The Development of Detector and Calibration Field as an Approach of Low Energy Photon Dosimetry

Suffian Bin Mohamad Tajudin

DOCTOR OF PHILOSOPHY

Department of Accelerator Science

School of High Energy Accelerator Science

The Graduate University for Advanced Studies (2015)

TABLE OF CONTENTS

LIST OF TABLES

LIST OF FIGURES

1 INTRODUCTION

1.1 PHOTON DOSIMETRY

In workplaces with radiation-generating devices and radio-isotopes, such as an accelerator, X-ray tube, and radioactive nuclei, radiation dose must be controlled properly to prevent hazards caused by exposure to radiation. Photon dosimetry is indispensable for this situation since photons are always produced as secondary radiation of energetic charged particles and neutrons, and emitted from activated materials due to irradiation of primary particles. Many dosimeters, methods, and standard fields have been developed that involve the energy region of interest to the present research.

To date, there are many different dosimeters available, and it is important to select one suitable for specific application. Commercially available dosimeters or survey meters are air ionization chamber, Geiger counter, NaI(Tl), CsI(Tl) and silicon. To be useful dosimeters, several studies have been conducted to understand their basic properties. Examples include the development of standard calibration fields, calibration of dosimeters and studies of the energy dependence of dosimeters. Such investigations are very useful in making dosimeters more reliable as a photon dosimeter.

Currently, air ionization chamber is widely used as a standard to evaluate the photon dose. The air ionization chamber is a common reference for dose measurements in various fields since it has a flat response, independent of incident photon energy. As examples, ionization chamber was used as a survey meter for monitoring the environment photon dose and perform quality control (QC) for diagnostic radiology. While in radiotherapy, two standard protocols (IAEA TRS-398 [1] and AAPM TG-51 [2]) have been developed for ionization chamber dosimetry of high-energy photon and electron beams.

For medical applications such as interventional radiology (IVR) or depth dose measurements in phantom, the dose measurements for a small photon fields and area drives the needs of smaller size dosimeter with high accuracy. The use of small size air ionization chamber is possible with main limitation- low efficiency due to the low density of air. Mainardi and Bonzi [3] had mentioned the smaller volume of plastic scintillator was adequate to obtain doses with same accuracy as with a large air ionization chamber with a volume of being in the ratio of 1:863. The use of detector system with a small size plastic scintillator had also been studied by workers in radiotherapy [[4],[5],[6]]. The use of other dosimeter such as NaI(Tl) is available with high efficiency but is known to exhibit a strong energy dependence [7].

1.2 ENERGY DEPENDENCE

It is important not to determine only the absorbed energy in the materials. Energy dependence is one of the important properties of photon dosimetry. The primary issue of energy dependence comes from the difference of atomic composition used in actual measurement and the one that should be measured. Soft-tissue is often the medium of interest in dosimetry. As an example, the photon response in scintillators differ for different incident energies compared to that of air or soft tissue due to their difference in atomic composition. Most of the scintillators have effective atomic numbers relatively higher than

that of soft-tissue. This problem is eliminated when both materials are identical; for example, air kerma should be measured with an air ionization chamber.

Figure 1 shows the mass attenuation coefficient of several materials as a function of photon energy.[8]. In the case of NaI below 200 keV, the photoelectric absorption is dominant because dependence of the photoelectric cross-section is proportional to $Z^{4 \text{ (or } 5)}$. As a result, for low energy photons NaI(Tl) detector exhibits strong energy dependence or higher response. It is mainly attributed by the enhanced photoelectric absorption at low energy photons. Accordingly, it will give higher reading than the actual dose. Therefore care must be taken in using such materials for dose-related measurements. In plastic scintillators Compton scattering is dominant for photons with the energy over 20 keV. The probability of a full-energy deposition event in the detector is often negligibly small. Thus, the energy dependence is less distorted and would be ideal as a photon dosimeter. This is an advantage over NaI(Tl) scintillator dosimeter. Water photon cross section was plotted together shows almost equivalent to that of plastics in a wide energy range in comparison to NaI or silicon.

In 1963, Murai et al [9] used a plastic scintillator for dose measurement. The choice of plastic scintillator material in their study was because it is near the tissue equivalent, which is useful for measuring tissue dose. In early 1990s, many studies focused on its application in high-energy photon beams [[4], [5], [6]]. In their studies, several advantages of plastic scintillators were identified including higher detection efficiencies, lower cost, flexibility in shape, and independence of atmospheric factors (e.g. pressure, humidity, and temperature).

1.3 PHOTON ENERGY AND DOSIMETER OF STUDY INTEREST

Following the nuclear reactor accident in Fukushima, Japan (2011) concern for Cs-137 contamination has increased along with an interest in radiation safety. From distribution of Cs-137 during the Fukushima accident, many detected photons have an energy of ~200 keV as a result of multiple Compton scattering [10]. This is an energy region of interest for medical dosimetry researches including the γ–sources used in nuclear medicine, surface radiotheraphy and diagnostic radiology.

For photon (gamma/X) detectors and dosimeters, the energy of the incident radiation is a major factor that can distort their responses. The dosimeters are commonly calibrated at a high energy photon with Cs-137 (662 keV), but then used at a lower energy region. The variation of the response of a dosimeter as a function of photon energy must be checked. As an example, the 200 keV energy region is critical for the response of a dosimeter owing to the transition point of photon interaction from the photoelectric effect to Compton scattering. Some dosimeters might have a higher response and indicate higher dose rate for ~200 keV photons.

For medical dosimetry, the dose to tissue is often the quantity of interest. Tissue-equivalent material is preferable to create dosimeters that directly represent the absorbed dose on human soft tissue. Table 1 shows the atomic compositions of soft-tissue [11]. Standard plastic scintillators (e.g., EJ-200, NE102A and BC-408) are normally fabricated from polyvinyl toluene, which only contain hydrogen and carbon with none of the higher atomic numbers. Thus, plastic scintillators are suitable candidates because the density and effective atomic numbers are close to those of human soft tissue.

However applications of plastic scintillators in the low energy photon region is not straight-forward. Plastic scintillators are well-known for their non-linearity below 200 keV [[7],[9]]. Several studies have reported that decreased light output distorts the response of incident photon energy below a few hundred keV due to the ionization quenching effect [[12],[13]]. The influence on energy response from the effect should be obtained to evaluate the accuracy of the measured absorbed dose by using plastic scintillators.

1.4 APPROACHES OF STUDY CONCERNING LOW ENERGY PHOTON DOSIMETRY

As a dosimeter in this energy range, ionization chamber is widely used as a standard. Recently, several applications are reported using plastic scintillator with combining optical fiber in medical field as a relative monitoring device of dose since it has advantages of high sensitivity, flexibility on shape and tissue equivalence. Thus, studying for response of plastic scintillator is meaningful to develop dosimeter applicable for wide photon energy range.

As a reference field, several radioisotopes have been used frequently, such as Cs-137 and Co-60. These nuclides provide relatively high-energy photons for dosimeters covering few tens of keV to MeV. According to above-mentioned applications, main energy is around 200 keV for both environmental and medical fields, since the former should consider scattering photons and the later should measure photons from X-ray generator. The reference field around 200 keV is strongly desired to confirm dosimeter readings.

The dosimeter being applicable to wide energy range and counting rate, and reference field to calibrate detector response should be prepared to obtain accurate readings for few tens of keV to MeV photons. Therefore, an approach of low energy photon dosimetry was performed to improve above situation through development of detector and calibration field for few tens of keV to MeV energy region. For the former point, photon dosimetry using a plastic scintillator was examined by considering quenching, a lower effective Z value, and the influence of surrounding materials. To compensate for the quenching effect and the lower effective Z, a lead-doped plastic scintillator (0.5%) was used to achieve a soft-tissue dose response in regions of less than 200 keV. For the latter point, a backscatter layout with a radioactive source was developed to provide a monoenergetic field with energy around 200 keV that were compared with those of an existing field with an X-ray generator. The acquisition and analysis of the photons spectrum were performed with a cadmium zinc telluride (GR1) detector and KSpect software (see section 3).

Table 1 Elemental compositions of soft-tissue weight by fraction (ICRU-4 component) [11].

Element	Fraction by weight
H	0.1012
C	0.1110
N	0.0260
O	0.7618

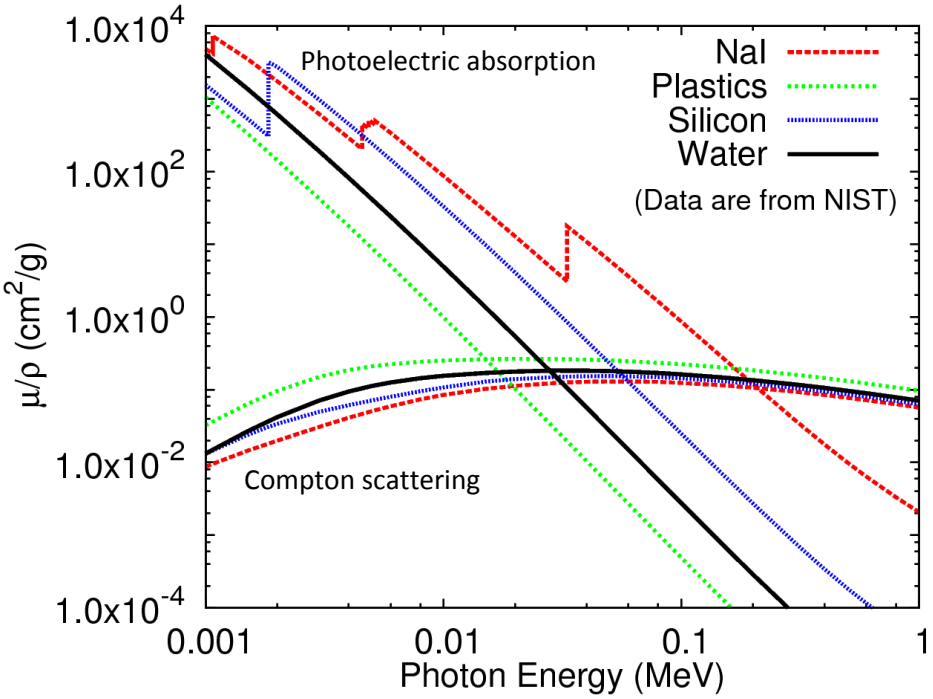

Figure 1 Mass attenuation coefficient, μ/ρ, of several materials as a function of incident photon energy [8], where ρ is the mass density of the material.

2 LITERATURE REVIEWS

2.1 DEVELOPMENT OF DETECTOR

2.1.1 Plastic scintillator as a dosimeter

The absorbed dose by using plastic scintillator (PLS) could be obtained directly based on pulse height distribution spectra. When we researched the studies comparison of the calculation and measurement of pulse height distribution of PLS with low energy photons, it is obvious that there is not enough comparisons had been carried out. Understanding the pulse height distribution is a key to the use of PLS as a dosimeter, and this was a problematic situation.

The application of PLS as a photon dosimeter (below 100 keV) in medical field had been studied in the current-mode widely. However the pulse height distribution is rarely measured. One of the reasons why there is little written about comparison of pulse height distribution in PLS photons seems to be that its response function is not clearly defined.

Kohan et al. [14] had calculated the pulse height distribution spectra of NE102 scintillators with joint codes: FLUKA for gamma transport and PHOTRACK for light transport. The calculated result was broadened by applying a Gaussian energy resolution to the output. However, the sigma (σ) value was not measured but was randomly added to the pulse heights. While in recent study by Ghadiri and Khorsandi [15] had adopted an optical photons model in the calculation. Both studies had obtained a good agreement at the around Compton edge peak of the Cs-137 source. However the comparison graphics of calculation and measurement of pulse height distribution do not show the lower level energy, and that makes it stand out less. The disagreement appeared at the low energy region after the Compton edge peak is important to evaluate in order to extend the use of plastic scintillator.

To date, few studies have addressed the use of plastic scintillators for gamma ray measurement of low-energy sources such as Am-241 (16.1 keV, 26.3 keV, and 59.5 keV) photons [14], [15],[16] ,[17]. A comparison of measured and calculated spectra in absolute values at such energy levels is useful for checking plastic scintillator response while considering the ionization quenching effect that is required for low-energy photon dosimetry.

2.1.2 Ionization quenching effect

Ionization quenching results in reduction of the scintillation response at low electron energies. Compton scatterings in the scintillator would produce several low scattered electron energies that are deposited in the scintillator. The generated ionizing particles will excite the scintillator molecules before de-excitation to emit the scintillation light. However, it may de-excite with less scintillation light as a result of quenching. It is therefore of interest to determine the response of scintillators particularly in low-energy regions to explain the possibilities of using plastic scintillators for photon dosimetry.

The electron response of plastic scintillator has been studied with various method for many years. Typically below 125 keV electron energies the scintillation light is significantly reduced in organic scintillators. Several semi-empirical models have been proposed to quantitatively describe the reduction in light output by ionization quenching of organic scintillators. The first model is introduced by Birks in 1951 to explain the degradation of light output through unimolecular quenching effect. In his formula, the author introduced a

constant parameter, *kB*, to represent the quenching effect. In 1953, Wright [18] introduced his model that considers unimolecular and bimolecular quenching. Heavy ionizing particles were suggested to introduce additional quenching due to bimolecular process. A more detailed approach was introduced by Voltz et al. [19] in 1966. It makes improvements to the previous models.

2.1.3 Birks formula of ionization quenching effect

The results of electron response were analyzed with the commonly used description of the non-proportionality by Birks. According to the Birks approach, light output of ionizing particles in scintillator material depends not only on its energy (E) but also on its stopping power (*dE/dx*). In this theory, Birks assumed that the high ionization density along the particle track is responsible for the reduction of scintillator response, i.e., quenching effect. The response of organic scintillators decreases due to the ionization quenching effect at less than a few hundred keV. There is one free parameter in the approach, the *kB* value (Equation 1);

$$\frac{dL}{dx} = A\frac{\frac{dE}{dx}}{1 + kB\frac{dE}{dx}}, \qquad (1)$$

in which *dL/dx* is light output per unit path length, *A* is the scintillation efficiency, and *dE/dx* is the electron stopping power.

For the typical organic scintillator compositions, the electrons will significantly lose their energies (*dE/dx*) with decreasing energy. Figure 2 shows the total stopping powers of electrons calculated with the ESTAR database [20] for vinyltoluene-based materials. The stopping values is higher at low electron energies below 200 keV. Thus, the amount of the light output per unit path length (*dL/dx*) decreases at the high *dE/dx* region.

Equation 1 is Birk's formula that gives the differential light output per unit path length. For the total light output, $L(E_o)$, from an electron of initial energy (E_o) should account for all light produced as the electron slows. Electron eventually loses all energy in the scintillator. The total light outout is obtained via the integration of Equation 2 over the energy interval from 0 to E_o:

$$L(E_o) = \int_0^{E_o} \frac{A}{1 + kB\frac{dE}{dx}} dE \qquad (2)$$

in which E_o is the initial electron energy and *dE/dx* is the total stopping power.

It has been reported that the response of well-type plastic scintillators is proportional to the energy deposition in the medium down to energies of 20 keV [21]. This result counters that of Birks's study for non-proportionality in plastic scintillators due to ionization quenching. Another study of liquid scintillator response to electron energies less than 20 keV confirmed Birks's formula with different values for kB (0.013–0.019 cm/MeV) depending on chemical concentration [22]. Craun and Smith had published a summary of Birks's constant kB for NE102 extracted from fits of Birks's formula to eight sets of experimental data, seven of which consisted of experimental data previously published by other authors. The values of *kB* ranged from 0.0096–0.0159 g cm^{-2} MeV^{-1}, primarily for proton particles ranging from 0.25–

11 MeV. Experimental data were described well, yet with different *kB* values for different measurements.

In many papers, the constant value of quenching parameter (*kB*) were reported for a wide energy range of particles. From current understanding, even if the non-proportionality of light outputs for electrons could be described based on the Birks law, the *kB* value might not necessary be the same for other particles such as protons. As an example, Chou [23] introduced one additional constant parameter to the Birks formula that give superior fits to the proton experimental data as published by Craun and Smith. Nevertheless, additional investigations are needed for possible relation to the *kB* parameter between low energy electrons and protons. While several values for *kB* were reported, it is important to know the effect of non-proportional light outputs of plastic scintillators, especially at low-energy photon dosimetry.

2.1.4 Compton coincidence technique (CCT)

The electron response of plastic scintillators is measured using a Compton coincidence technique [24]. The technique based on detecting Compton electrons produced by incident photons in the scintillator. At the same time, the scattered photon created as a result of Compton scattering interactions would escape from the scintillator. The escaped scattered photon and its energy are measured by a calibrated reference detector. By knowing the initial energy of incident photon and the final energy of scattered photon, one can evaluate the remaining energy transferred to the Compton electrons inside the scintillator.

For the measurements reported here, the target scintillator (EJ-200) was exposed to a collimated beam of 662 keV gamma rays from Cs-137. In Compton coincidence measurements, the incident γ-rays of 662 keV deposit part of their energy to an electron after undergoing Compton scattering interaction inside the target scintillator (EJ-200). Meanwhile, the Compton-scattered γ-rays' energy is deposited in the reference detector (NaI(Tl)) in coincidence. The energy deposition due to Compton electron energy within the target scintillator ($E_{EJ\text{-}200}$) can thus be calculated by using the conservation of energy:

$$E_{EJ\text{-}200} = E_{\gamma} - E_{NaI(Tl)} \qquad (3)$$

in which E_{γ} is the energy of the incident photon and $E_{NaI(Tl)}$ is the energy of the Compton-scattered γ-rays deposited in NaI(Tl).

2.1.5 Compensation for plastic scintillator response

Several researchers have made an attempt to compensate the difference of plastic scintillator between soft tissue in response at low-energy photon region (< 200 keV). To optimize the air or soft tissue equivalent of low-energy photons, Mainardi et. al [[25],[26]] had proposed doping the plastic with silicon ($_{14}$Si) and chlorine ($_{17}$Cl) through Monte Carlo simulations, respectively. In tissue-equivalent material the absorbed energy should be proportional to that in the soft tissue. The author had mentioned that it was impossible to apply the same atomic composition of plastic scintillator to the whole energy region for medical application. Instead doping with chlorine at two different concentrations were proposed; low concentration for the diagnostic photon energies while higher one for radiotherapy. However the details of the concentration was not mentioned.

For the former point, BICRON Co., a commercial company making plastic scintillators verified that the silicon-doped scintillator is chemically unstable with poor optical clarity because high concentrations of silicon are necessary to increase the absorbed energy efficiency [26]. For the latter point, Williamson et al. in 1999 [27] tested the proposed chlorine-doped plastic scintillator (4% of Cl) for its response to low energy X-ray beams. The author considered the quenching effect by measuring the current value to determine the light output. Nevertheless, the compensation is less than expected for the flat response. The higher atomic number materials such as Pb or Bi would be good candidates for doping into plastic scintillators. In contrast, Lessard et al. [28] recently demonstrated that the standard plastic scintillator could be applied for photon dosimetry in the low energy X-ray field. The expected underestimation of response in low energy X-rays field was compensated by applying the correction factors based on the medium differences, to overcome the energy dependence or quenching effects.

2.2 DEVELOPMENT OF CALIBRATION FIELD

In application of photon (gamma/X) detector and dosimeter, energy of radiation is one of the major sources to distort their response. When radiation detector is calibrated, it is desirable to calibrate for wide energies. Most of the detector and dosimeter are calibrated with Cs-137, 662 keV mono-energetic gamma-ray source. As an example, the 200 keV energy region is critical for the response of a dosimeter owing to the transition point of photon interaction from the photoelectric effect to Compton scattering. Thus, calibration for the low energy region is necessary to reduce any uncertainty contributions from the detector's energy response to the measured data. Stable sources mostly concern higher monoenergetic regions and one must accept the presence of errors in low energy measurements because do not have an adequate calibration field. Therefore, a low energy monoenergetic field would be desirable to determine the energy dependence of dosimeters in this energies.

For ensuring the accuracy of photon dosimetry, calibration of dosimeters is actively carried out at several laboratories such as at the Facility of Radiation Standard, JAEA (Japan) and at National Institute of Standard and Technology, NIST (US). Monoenergetic photon fields are preferable for this purpose since the energy response of dosimeters becomes more obvious. Several radioactive sources with known activities have been widely used for this purpose—primarily photon energies exceeding 600 keV except for Am-241 (60 keV). Between 60–600 keV, filtered X-rays are also candidates though they are broader in energy width and are less affordable to prepare. Around 200 keV is missing energy for calibration (Figure 3). Several short, half-life radioactive sources that suit this energy range are inadequate as references. As such, a stable monoenergetic field with approximately 200 keV of energy was most desirable for study purposes.

Figure 4 shows a Compton-scattered photon and its energy dependence as a function of scattering angle. Backscatter radiation is the radiation scattered with a large angle after undergoing Compton scattering interaction inside the material. According to kinematics of Compton scattering, the Compton-scattered photon energy can be calculated by:

$$hv' = \frac{hv}{1 + \frac{hv}{mc^2}\,(1 - cos\theta)} \qquad (4)$$

where hv is the energy of the incident photon, hv' is the energy of the Compton-scattered photon, ϑ is the scattering angle between the directions of the incident and Compton-scattered photons, and mc^2 is equal to 511 keV, denoting the energy of an electron at rest.

As far as I searched the literature, no paper has been published on the use of Compton scatted photon for calibration field. In this thesis, backscattered is proposed to produce quasi-monoenergetic radiation around 200 keV. From Figure 4, all the gamma rays from Co-60, Mn-54, and Cs-137 have Compton-scattered photon energies from 180 to 210 keV for scattering angle, θ, between 150-180°. Theoretically, the Compton-scattered photon energy widths at this scattering angle range for Co-60, Mn-54, and Cs-137 are 12.7 keV, 10.5 keV, and 9.4 keV, respectively. If the Compton-scattered photon which has a scattering angle of 150-180° is selected, its energy range is about 200 keV.

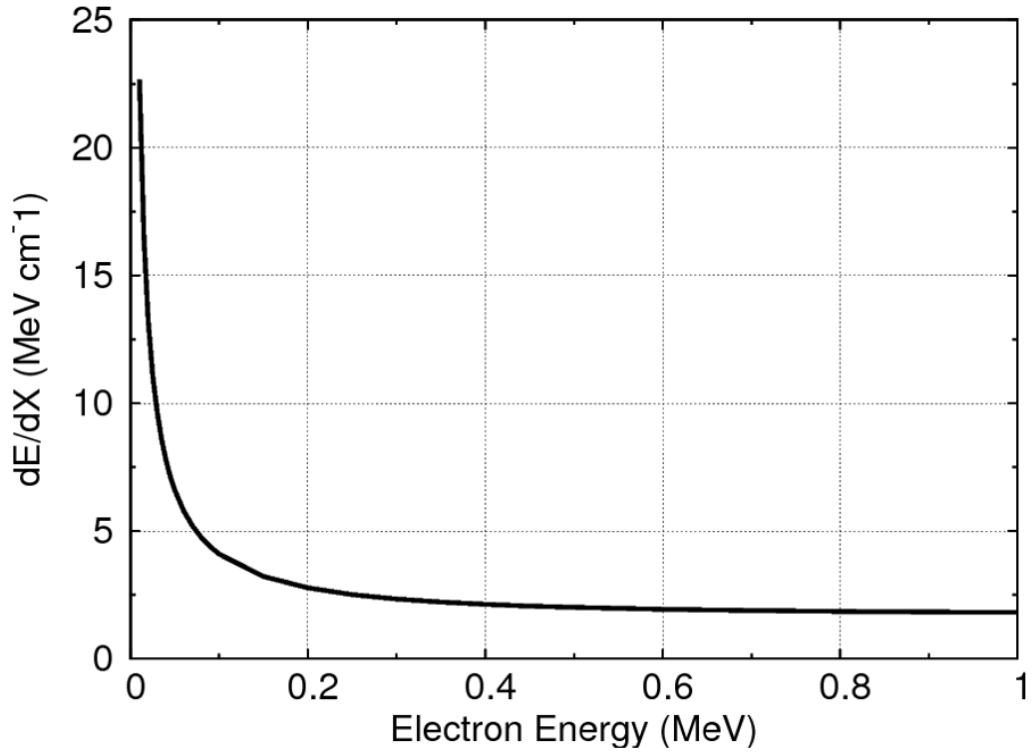

Figure 2 Total stopping powers of electrons calculated with the ESTAR database for vinyltoluene based materials [20].

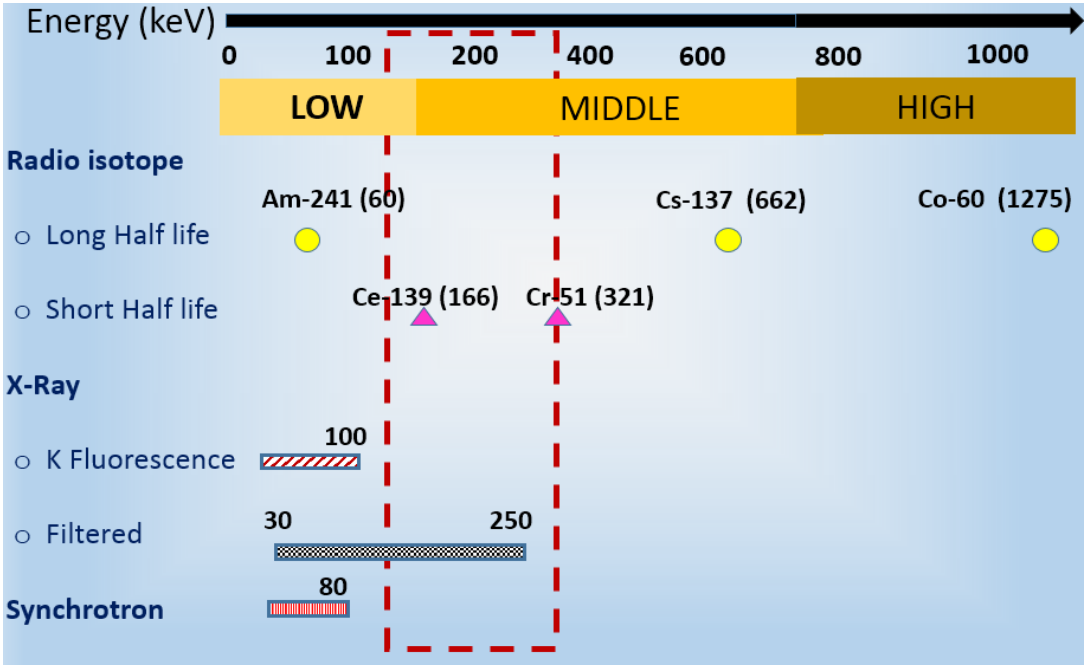

Figure 3 The available candidates of photons radiation for calibration. The rectangle red box is concerning candidates of photons energy around 200 keV such as short half-life ($T_{1/2}$) sources and broad X-ray beam. Development of a calibration field is highly desired within this energy range.

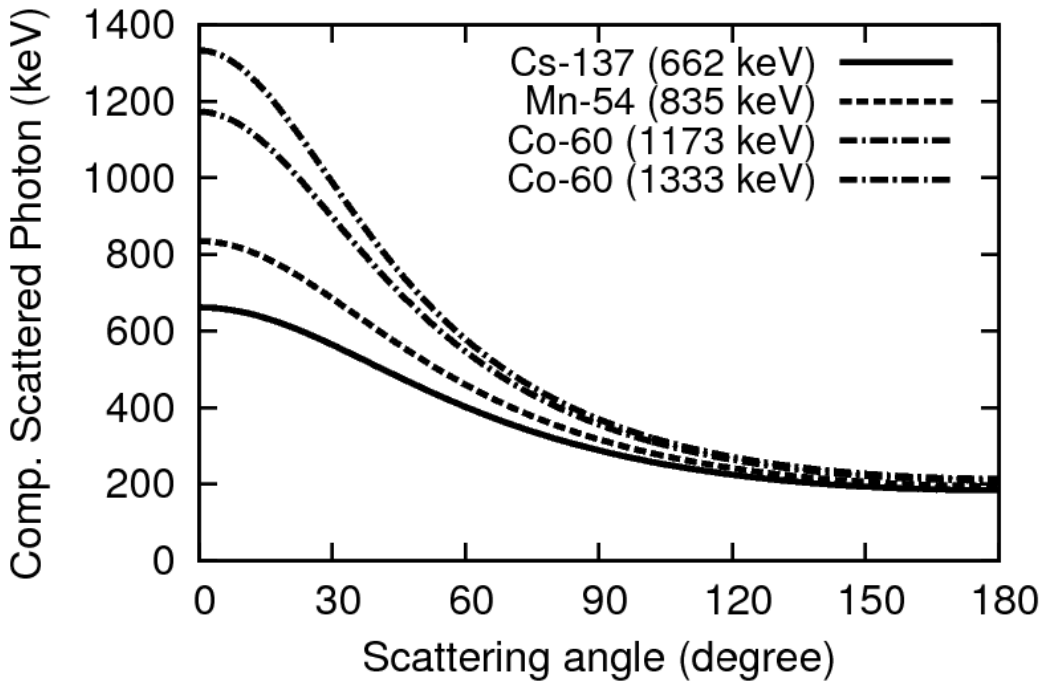

Figure 4 Compton-scattered photon energy as a function of the scattering angle θ, calculated according to the Compton scattering equation for Cs-137 (662 keV), Mn-54 (835 keV), and Co-60 (1173 and 1333 keV).

3 EXPERIMENTAL SETUP AND CALCULATIONS

3.1 DEVELOPMENT OF DETECTOR

3.1.1 Preparation of plastic scintillators

The scintillation detector consists of plastic scintillator and photomultiplier tube (PMT). The properties of the plastic scintillators (Eljen Technology, Sweetwater, TX, USA) [29] used in this study shown in Table 2. Matching their emission spectra to the readout device's photocathode-sensitivity spectra is important for efficient light collection. The emission spectra of EJ-200 (and EJ-256 for lead-doped scintillator) as functions of wavelength vary mostly from 400–500 nm (Figure 5(a) & (b)). The emission spectrum peaked at 425 nm. The readout device used was a photomultiplier tube Model R375 from Hamamatsu [30] with a diameter of 5.1 cm. The quantum efficiency of the photocathode also varies as a function of wavelength (Figure 5 (c)). The peak wavelength of the PMT's spectral response occurred at 420 nm, which is close to the photon emission spectra of both scintillators. The effective diameter of PMT is 4.6 cm.

The whole setup has to be light-tight wrapped to avoid any background light that may cause damage to the PMT. The scintillators were prepared with the following steps: (1) Three layers of white Teflon tape were applied to fully cover all of the non-exiting surfaces of the scintillator (Figure 6). (2) Optical silicone grease (Model: EJ-550) was applied between the PMT and scintillator for coupling. To remove any air bubbles, light pressure was applied between them during the coupling process. (3) The scintillator-PMT was then wrapped with a black tape to improve the light reflection and for the safety of PMT. (4) All of these were wrapped with aluminum foil.

3.1.2 Calibration of plastic scintillators

In this study, the γ–γ coincidence technique was adopted. Pulse-mode ADC was used as the readout electronics for pulse processing and triggering. The lower-level discriminators (LLD) of the ADC were fixed to 15 channels for spectra with 1024 channels. The same discriminators were applied to other ADC channels used (including reference detectors). The zero baseline of all the amplifier outputs were checked (and adjusted if necessary) prior to the measurement by monitoring with an oscilloscope. The pulse height was then calibrated with a high precision pulse generator (Model 419, ORTEC). The zero offset of the pulse height was deduced for each ADC channel.

Two sets of detectors—target (EJ-200/EJ-256; 5.1 cm diameter x 1 cm long) and reference (NaI(Tl); 5.1 cm diameter x 5 cm long)—were arranged to face each other at a distance of 10 cm, as shown in Figure 7. The same design and dimension of the detector holders (acrylic) of both detectors ensures they are in aligned to each other. The gamma ray source was placed between the target detector and the reference detector. The photons from the gamma ray source that enters the target scintillator will be reflected to the reference detector in 180° scattering angle owing to the face-to-face geometry.

High voltages of +550 V and +500 V were applied to the PMTs of the target scintillator and reference detectors, respectively. Signals from the PMTs were fed into preamplifiers (Model 5548, Clear Pulse for target and Model 5626, Clear Pulse for reference detector), the outputs of which were processed by the primary amplifiers (ORTEC 572A). All amplifier outputs were fed into an analog-to-digital convertor (ADC) (A3400, Niki Glass Co Ltd.). Pulse height data were accumulated using VMEbus and recorded event by event with timestamps (5 ns step) in the hard disk drive of a personal computer connected to Gigabit Ethernet. The data acquisition system can be applied to up to 16 channels with 10^5 events per second for each ADC board.

3.1.3 Electron response of plastic scintillators

Figure 8 shows the experimental setup. Cs-137 (200 MBq) was placed inside the full lead housing consisting of blocks 5 cm thick, one with a collimator hole 1 cm in diameter. The distance between the source to the collimator was 20 cm. The target scintillator (EJ-200; 5.1 cm diameter x 5 cm long) was placed 30 cm from the outer surface of the lead housing. The side wall of the target scintillator was arranged to face the collimator hole. The beam diameter irradiating the target scintillator was 2.2 cm. The central axes of the source, collimator hole and the target scintillator were aligned. The distance between the target scintillator and reference detector was 40 cm, and both were aligned.

Figure 9 shows the block diagram of the readout electronics. High voltages of +800 and +500 V were applied to the PMTs of the target scintillator and reference detectors, respectively. Signals from the PMTs were fed into preamplifiers (Model 5548, Clear Pulse target and Model 5626, Clear Pulse for reference detector), the outputs of which were processed by the primary amplifiers (ORTEC 572A). The minimum dead time occurred with a shaping time of 0.5 μs. All subsequent measurements were performed with the same settings. All amplifier outputs were fed into an analog-to-digital convertor (ADC) (A3400, Niki glass Co Ltd.). Pulse height data were accumulated using VMEbus and recorded event by event with timestamps (5 ns step) in the hard disk drive of a personal computer connected to Gigabit Ethernet. The data acquisition system can be applied to up to 16 channels with 10^5 events per second for each ADC board. The low-level discriminator of the ADC was set at 15 channels over 1024 channels. The target scintillator count rate per second was 7135 ± 18 cps. The electronic parts and their parameters were kept constant throughout the experiment.

Experimental data are taken for the fourteen scattering angles from 15 to 140 degrees by changing the position of the reference detectors. The angle range corresponds 34 to 462 keV for a Cs-137 source. Each run typically takes two hours to obtain enough statistics for coincidence counts. Data are also taken for NaI(Tl) (OKEN, standard type 8A8) of 5 cm in diameter and 5 cm in length by coupling to the same photomultiplier (Hamamatsu, R375) as a target scintillator. This confirms the validity of the experimental data through comparison with data taken previously. For NaI(Tl), nine hours was required for each run due to a lower probability that a gamma ray paths through the scintillator with one Compton scattering and without more interactions. Since longer acquisition times were necessary, an additional three units of reference detectors, NaI(Tl) (Model: OKEN; 5 cm in diameter and 5 cm in length) were prepared for simultaneous use.

3.1.4 Energy resolution of plastic scintillator

The pulse height distribution for photons at a hundred keV or more usually lack a total energy absorption peak, and is only a Compton continuum. Due to this, it is difficult to argue in detail about the energy resolution. As example, the energy resolution had been systematically studied by Hohara et .al [31] through finding the agreement between the measured and simulated spectra.

The low energy photons from Am-241 shows a clear photoelectric peak. The energy resolution of the scintillator was obtained from the measured photopeak of Am-241 by Gaussian fit ($FWHM_o$). For smearing of calculated spectra, energy dependency of the resolution (*FWHM*) was assumed to be a proportional ratio to square-root of the energy (*E*) as in Equation 5;

$$FWHM = \frac{FWHM_0}{\sqrt{E/E_o}} \qquad (5)$$

in which $FWHM_o$ value is determined for the photo-peak of Am-241 (E_o).

3.1.5 Pulse height distribution spectra

3.1.5.1 Experimental procedure

The pulse height spectra were measured from the 60 keV to 800 keV energy range. Am-214, Co-57, Cs-137 and Mn-54 were employed as standard sources. Experiments were performed in an open geometry with a source located at a distance of 10 ± 0.15 cm on the axis of the scintillator (Figure 10). The measurements were performed for both standard (EJ-200) and lead doped (EJ-256 0.5 % Pb) plastic scintillator of the same size (5 cm diameter x 1 cm long). Both were coupled to the same single photomultiplier tube (Hamamatsu, R375), which is the same one used in Compton coincidence measurements. The environment background measurements were performed at the same place to obtain the net counts.

The same bias voltage, shaping time and data acquisition system were used as in section 3.1.3 for energy calibration. The quality of the detector wrapping was checked with and without the light shield-box by monitoring the average background count rate in both conditions. For the measurements reported here, the difference between count rates was negligible. Poor wrapping condition may introduce unnecessary counts or noise which affects the pulse height spectra.

3.1.5.2 Calculation procedure

3.1.5.2.1 Calculation of pulse height distribution

Monte Carlo code for electron and photon transport (EGS5 code [32]) was used to calculate the scintillator pulse height spectra. The photons interaction such as photoelectric absorption, Compton scattering and pair productions were considered. The branching ratio of the gamma sources were sampled as the JRIA data book [33]. The calculation geometry is shown in Figure 11. The photons were emitted in the 4π direction to include the effect of plastic source casing. The scintillators material data and its density for the calculations correspond to the manufacturer's data (Table 2). For accurate calculation of scintillator pulse

height spectra, two parameters were determined experimentally to include in the calculations; the non-proportionality of light output and energy resolution in the plastic scintillator. The energy resolution will be discussed in the section 4.1.3

For the first case, calculation of the spectrum corresponds to the energy deposition of the gamma sources (C1). In the second case, the scintillator non-proportionality (ionization quenching) was considered (C2). A subroutine consisting of the data of total light output as Equation 2 (kB=0.016 g cm^{-2} MeV^{-1}) was included inside the user code to calculate the absorbed energy with light output dependent. The Birks parameter of the kB value comes from an experimental measurement as reported in section 4.1.2. The measured relative electron response is normalized at 0.462 MeV as per experiment data. A normalization factor at the same energy was calculated to apply on the all calculated light output results inside the user code.

3.1.5.2.2 Calculation of a normalization factor for electron Quenching effects

The light output as a function of electron energies were calculated with the Birks formula. The effect of electron binding energy and Moller scattering were included in the calculation. According to the Birks formula, there are two parameters needed for input in the calculation; the kB value and the total stopping power (dE/dx). The kB value of 0.016 is used as determined from the measurement. The total stopping power of EJ-200 scintillator was deduced from the EGS5 code and extrapolated down to 1 keV (Figure 12). The user code was opted for unrestricted collision and radiative stopping power for the material data of EJ-200. The ratio of light output to the incident electron energy is shown in Figure 13. For the calculation reported here, the normalization factor was calculated at 0.462 MeV. The value of normalization factor derived from the figure is 1.186. Nevertheless, Figure 13 indicated that above 0.462 MeV, the results with quenching effect are similar to the energy deposition. They are not dependent on the kB value. Finally, the same normalization factor was applied on the light output results inside the user code to yield the pulse height distribution with normalized quenching effect. The pulse height spectrum of several gamma-ray sources were calculated for both scintillators of EJ-200 and EJ-256 (0.5 % Pb) to be compared with the experiment.

3.2 DEVELOPMENT OF CALIBRATION FIELD

3.2.1 ~200 keV photon field by backscatter layout

The basic backscatter layout is shown in Figure 14. A lead block was used to absorb the direct component. The floor served as the scattering material. When the primary photon was removed on a sufficiently thick lead block, the backscatter photons that were scattered by the floor with large angles could be measured, as indicated by the solid arrow line in the figure.

3.2.1.1 Backscatter Layout Optimization by Calculations

In order to improve the backscattered field photon spectra, the arbitrary parameters of the backscatter layout were studied with Monte Carlo simulations. The first three parameters shown in Table 3 were optimized to enhance the backscatter peak and to reduce the lower energy components.

The EGS5 code was used to calculate the backscattered photon spectra and ambient dose equivalent (Sv/photon). Surface crossing was used to calculate the back-scattered photon dose and spectra on the surface of 2 cm x 2 cm (X-Y axis system) scoring region. In order to obtain ambient dose equivalent, air absorbed dose (Gy) was calculated as a first step by using kerma approximation. A function was adopted in the calculation to evaluate the ratio of ambient dose equivalent (Sv) to air absorbed dose. Then the ambient dose equivalent was calculated by multiplying the ratio of ambient dose to air absorbed dose.

The geometry used in the calculations is the same as that shown in Figure 14. The scoring region was positioned at a detector-to-lead distance (DPD) of 15 cm from the top of the 10 cm x 10 cm x 10 cm lead block. The source was placed at a source-to-floor distance (SFD) of 20 cm from the surface of the concrete floor. A single-energy, 662keV point isotropic source was used in the calculation, and the solid angle of the source photons was 4π, as in experiment. The concrete floor was a cylinder with a radius of 150 cm and a height of 1 m.

Two indicators were used to study the obtained photon spectra: the mean energy and the peak-to-total ratio. The average energy (<E>) of a photon spectrum was calculated by the Equation 6:

$$< E >= \frac{\int_0^\infty E \cdot f(E) dE}{\int_0^\infty f(E) dE} \qquad (6)$$

where *f(E)* is the number of photons with energy *E*. Each photon was multiplied by its corresponding energy and all the product was integrated over the whole spectrum. The integral of all the products were divided by the total number of photons to yield the mean energy. The peak-to-total ratio is defined as the ratio of the integral number of photons of the backscatter peak to the total number of photons over the entire spectrum. The peak boundary of backscattered photons was determined as ± 10 keV from the peak centroid. The ambient dose equivalent (Sv/photon) was also calculated for each examined layout parameter.

3.2.1.2 Uniformity of the Backscattered Photon Field

The optimal backscatter layout to provide a uniform backscattered field was obtained from experiments and calculations. The goal was to obtain a uniform backscattered radiation field with less than 10 % variation over a wide area. Thus, the position dependence of the field was examined for the spectral shape and dose rate by changing the detector position and scoring region (temporarily set as DPD=15 cm) under the predetermined backscatter layout. It is important to establish a uniform radiation field at the detector location to reduce the position dependence of the calibration field for application to various sizes of dosimeters and detectors.

The experimental backscatter layout used in this study is shown in Figure 15. The layout features optimized parameters, such as lead block thickness of 10 cm, SFD at 20 cm, and the added 1.4 m x 1.4 m x 0.05 m square of iron on the concrete floor. The uniformity of the backscattered radiation field in the tested area was examined vertically and horizontally. The same optimized layout was also modelled in EGS5-CGview [34]for uniformity studied as shown in Figure 16.

The Cs-137 source used (AEA Technology QSA Inc., Code no: CDC 805) was sealed within a stainless steel capsule with dimensions of 6 mm (diameter) × 8 mm (length). The source was then placed under an aluminum case 45 mm (diameter) × 15 mm (thickness) with an acrylic window with a thickness of 1 mm. The source activity at the time of the experiment was 208 MBq (5.62 mCi).

The spectra of the backscattered photons were measured by a $Cd_{1-x}Zn_xTe$ detector (KROMEK, Model GR1) whose size was 1 cm x 1 cm x 1 cm. The dose rate was measured by a NaI (Tl) scintillation survey meter with a crystal size of 25.4 mm (diameter) × 25.4 mm (length) (ALOKA, TCS-171), and with an ionization chamber survey meter of 400 cm^3 effective volume (ALOKA, ICS-321). The uniformity of the backscattered radiation field was examined at different DPD values in the vertical direction and with respect to the horizontal position of the detector.

3.2.2 ~200 keV photon field by an X-ray generator

Monoenergetic photon fields are indispensable for calibration of radiation detectors and dosimeters. An X-ray generator could produce photon energies about 200 keV by using appropriate filtration and voltage. Primary X-ray beams are polychromatic in nature with most of the photon average energy being one-third of the maximum energy of the X-ray. Therefore, filtration of the primary X-ray beam would reduce the total number of X-ray photons in the beam and removes a greater portion of the low-energy photons. Filters added to the X-ray beam are most often constructed of high atomic number materials such as lead, tin, and tungsten. In this present study, several sets of filters and applied peak voltages are demonstrated to provide a few hundred of keV mono-energetic photon field. Selection of filter materials and their thicknesses are based on data from ANSI, ISO, JAERI and NIST organizations [[35], [36], [37], [38]].

3.2.2.1 Calculation of photon spectra for filtered X-rays

SpekCalc software [39] was used to obtain the unfiltered X-ray spectra as a source input for EGS5 code. The code is used to select candidates for filter materials, thicknesses and combination. A strong single filter, Tungsten (W, with 5 mm thick) is chosen due to its narrow

calculated photon spectra in comparison to literature filter sets with one drawback— the clear observed K X-rays of the tungsten filter. Figure 17 shows the calculated photon spectra for filtered X-rays of 250 kVp. The mean energy for (a) to (c) are 203, 209 and 206 keV, respectively. It was expected that the broad peak of the filtered X-rays will be measured concerning the broad width of the calculated photon spectra.

3.2.2.2 Measurements of suggested filter materials

The experiment is performed with the X-ray tube (Comet; MXR-320/26) at the radiation calibration facility, KEK, Japan. A distance of 5.3 m ± 1 cm between CdZnTe and filter surface was adequate to avoid significant dead time losses. The detector has a higher detection efficiency at X-rays energies. The lower energy threshold of the CZT was set to 24 keV (lower than default energy=32 keV) without any significant dead time effect observed for measurements. Three data were taken for each filters; (1) direct measurements with the filters, (2) measurements with filters with a lead bar was placed in front of the CZT to account the room-scattered radiation, and (3) background of radiation measurement. The measured spectra properties are evaluated as a result of mean energy, full energy peak, energy width and dose rate.

3.2.3 Spectrum measurement using CdZnTe detector

CZT detector have several advantages such as its compact size as well as stability and good energy resolution are very useful in the study and understand the photons field. To evaluate energy width for both backscatter and X-ray generator fields, a 1-cm^3 CdZnTe detector (KROMEK Model GR1) was used. In previous studies, the problems of inactive layer and incomplete charge collection efficiency had been reported for the CZT detector (1-cm^3). In this study, the measured peak efficiency (%) was compared to the literature data [40] and calculated in absolute values.

3.2.3.1 Measurement - calculation geometry

The check sources (as listed in Table 4) were placed 10 cm away from the surface of CZT as shown in Figure 18. All the sources used were encased in a plastic discs and were aligned to the center of CZT surface. The data acquisition and analysis of the photon spectrum were performed with its software (KSpect) running on a personal computer. The background radiation was taken at the same place as where the measurements were conducted. Figure 19 shows the model of CdZnTe detector in EGS5-CGview for particle trajectory. The main parameters of the geometry are:

(a) The active crystal area is 1.0 x 1.0 cm^2,
(b) The active crystal thickness is 1.0 cm,
(c) The outer case is 1.2 mm thick aluminum,
(d) The window is 0.5 mm thick aluminum,
(e) The distance from the window to the surface of the crystal is 5 mm.

The proportion numbers of CZT material components are 0.9, 0.1, and 1 for Cd, Zn, and Te respectively. Density is set as 5.86 g/cm^3. The source was positioned at a 10 cm distance from the window corresponding to the measurement and literature geometry. The 4π isotropic source photons go toward the CZT and cover only the front face of CZT crystal area as shown in Figure 19.

From preliminary calculation, calculated peak efficiency exceed measurement. Thus calculation for CZT of several sizes were performed.

The peak efficiency depends on the geometry of the detector and crystal size. To assume the effect of insensitive region, the active crystal area was re-modelled. While remaining the original size of the crystal area (1.0 cm x 1.0 cm), the “effective” area that registered the events was reduced. The outer part of the “effective” area would become the reflector. The geometries of the remodelled crystal depicted in Figure 20.

Table 2 Physical characteristics of the plastic scintillators studied

Scintillator model	EJ-200	EJ-256 (0.5% Pb)
Size		
Diameter (cm)	5	5
Length (cm)	1, 5*	1
Light output (% of anthracene)	64	56
Density (g/cm^3)	1.023	1.028
Decay time (ns)	2.1	2.1
Max. emission spectrum (nm)	425	425
Typical light attenuation (cm)	380	-
Composition (proportions by relative atomic weight)	H: 0.084 C: 0.916	H: 0.084 C: 0.911 Pb: 0.005

*A length of 5 cm was used for electron response measurement and 1 cm for photon dosimetry study.

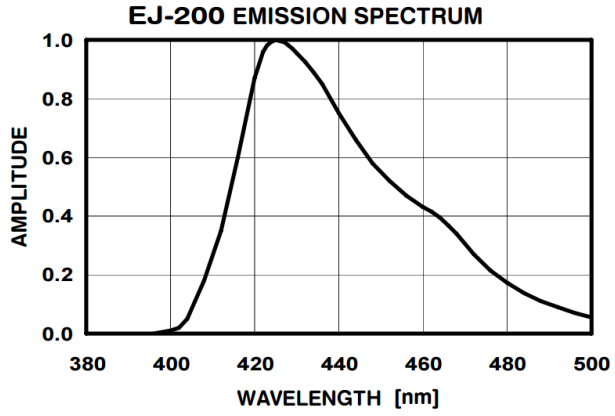

(a)

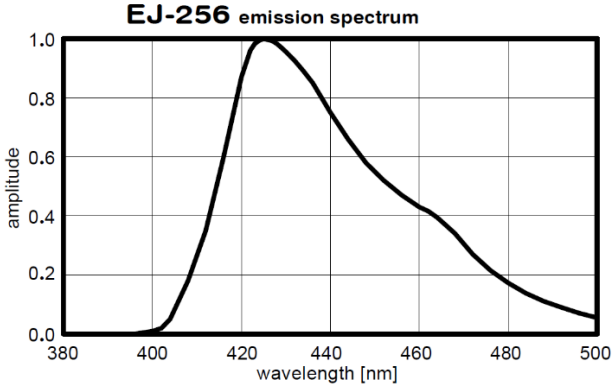

(b)

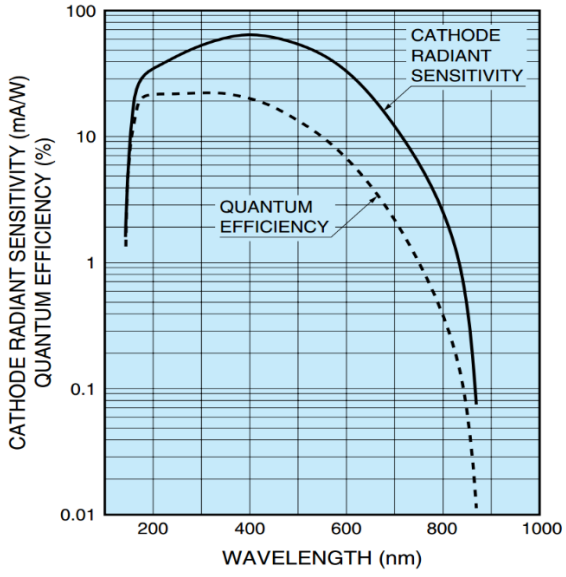

(c)

Figure 5 Scintillator emission spectrum of EJ-200 (a) and EJ-256 (b) [29]. The wavelength peak of both scintillators is 425 nm. Figure 5 (c) shows PMT photocathode sensitivity as a function of incident wavelength of light [30]. The wavelength peak is 420 nm. The matching of the scintillator photon emission spectrum and PMT response is important for efficient light collection. The figures were adopted from the manufacturer's webpage.

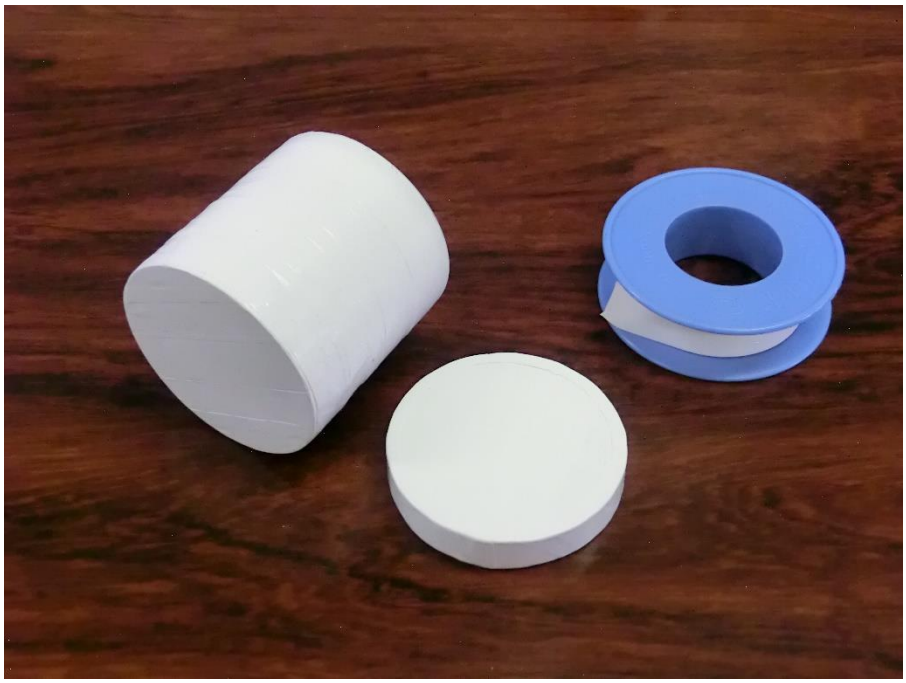

(a)

(b)

Figure 6 Final appearance of the self-wrapped scintillator of both thicknesses with white Teflon tape; 5 and 1 cm are ready for use (a). Three layers of Teflon tape were used for better light reflection. The exit face of the scintillator (non-wrapped part) is optically coupled to the PMT of the same diameter with optical silicon grease (b).

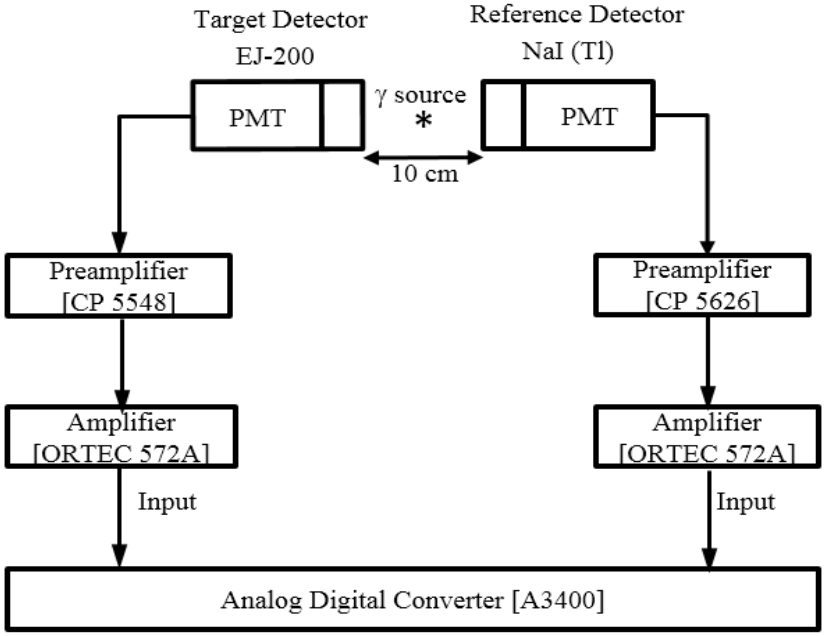

Figure 7 Block diagram showing the electronics used in the experiment of γ–γ coincidence. Two sets of detectors, target (EJ-200) and reference (NaI(Tl)), are arranged face to face. The separation between the target and reference detector is 10 cm. The gamma ray source is placed in the middle of the target detector and reference detector. The photons from the gamma ray source that enter the target scintillator will be reflected to the reference detector at a 180^0 scattering angle because of the face-to-face geometry.

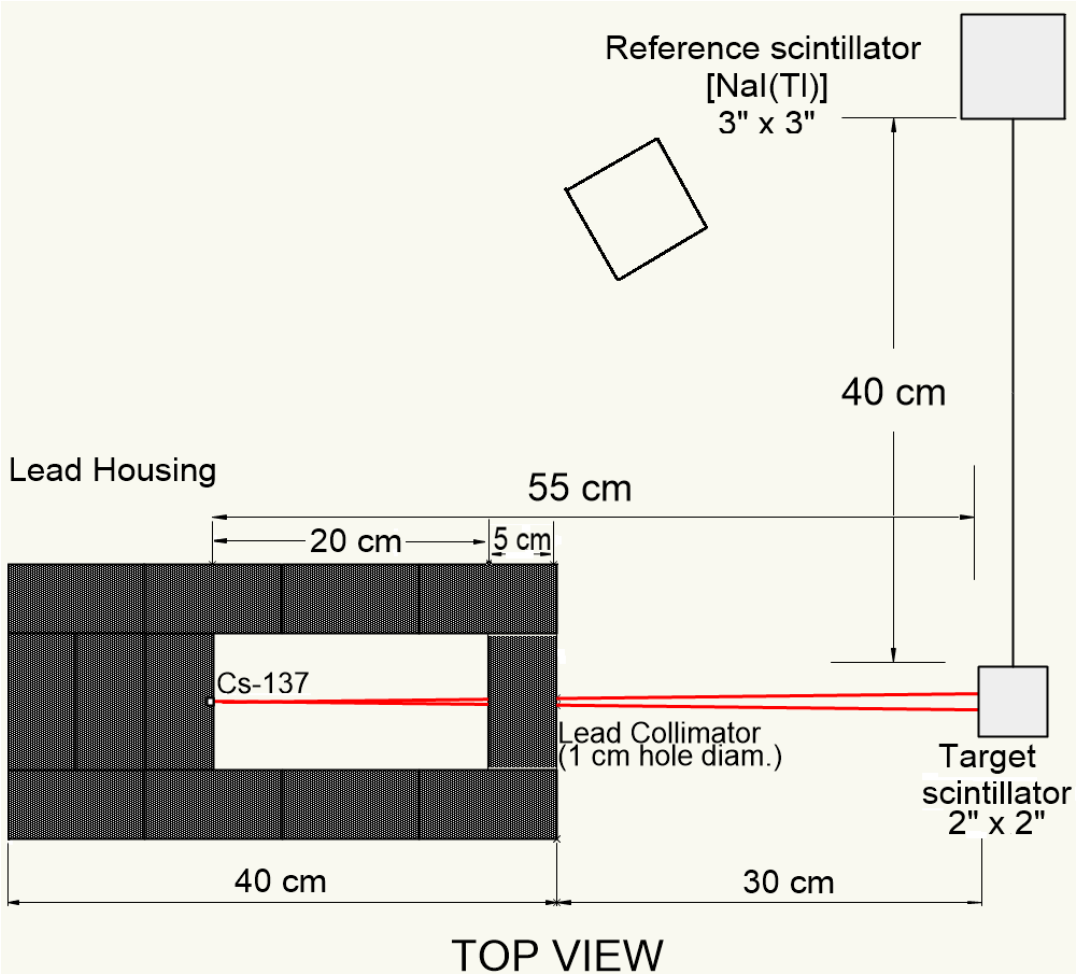

Figure 8 Schematic diagram of the setup for Compton coincidence technique in the actual scale size. The measurement was performed at the radiation calibration facility, KEK with a Cs-137 source intensity of 200 MBq. The Cs-137 source inside the lead housing was collimated to irradiate only the target scintillator. The collimator hole diameter is 1 cm. The beam diameter irradiated the target scintillator is 2.2 cm. The distance between the target and reference scintillator was fixed at 40 cm as for scattering angles (15^{o} to 140^{o}). The collimator opening, source, and target scintillator were in alignment. The same acrylic detector holder design and dimensions aligned both the target and reference detectors.

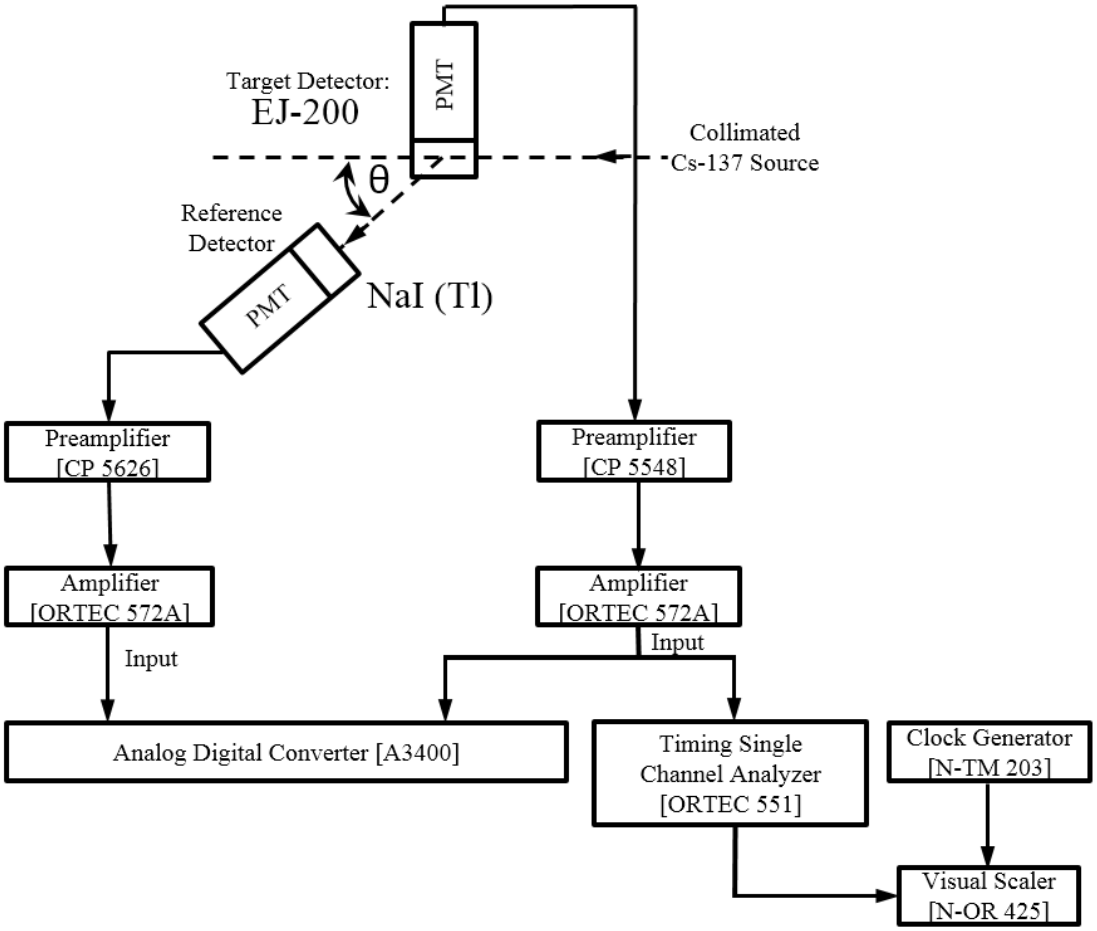

Figure 9 Block diagram showing the electronics used in the experiment.

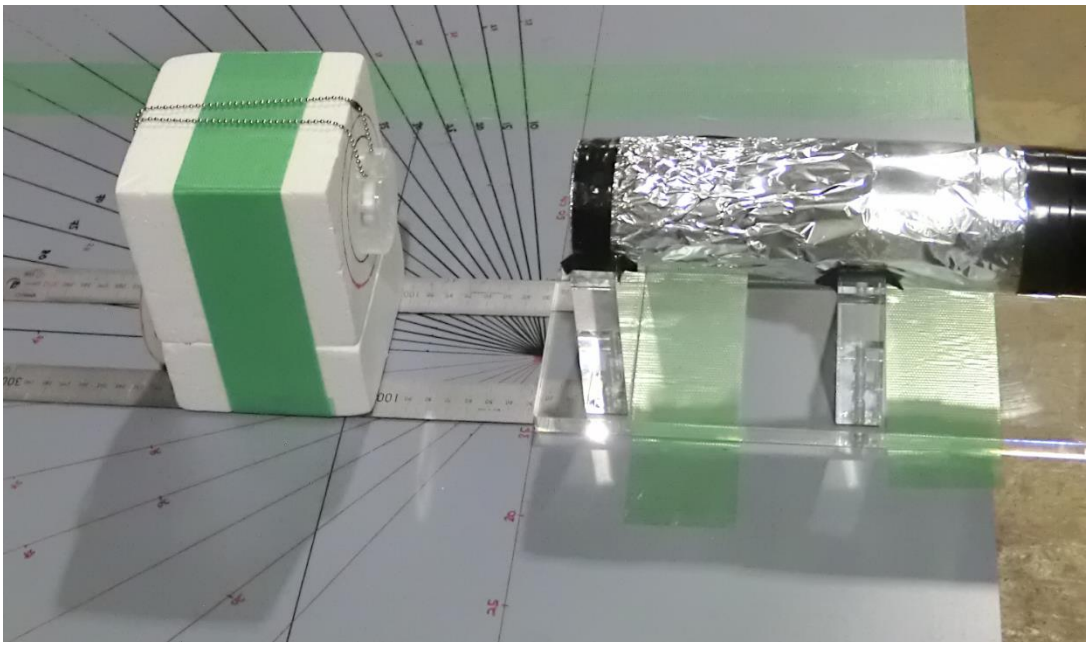

Figure 10 Picture showing the direct measurement of gamma sources in open geometry. The distance is 10 cm between the sources and surface of the scintillator. All sources were encased in the same plastic housing.

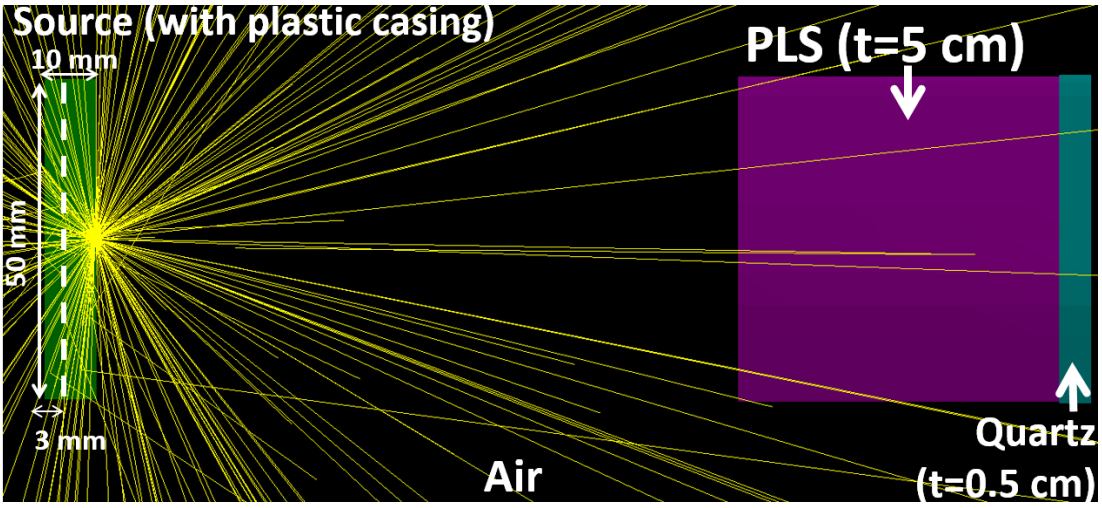

Figure 11 Simulation geometry modelled in EGS-CGview for calculation of the scintillator energy deposition. The photons were emitted in 4π that was isotropically incident to the plastic scintillator (PLS=5 cm long) which was coupled to the PMT window (Quartz=5 mm long). The wrapping materials such as Teflon tape and aluminium foils were ignored.

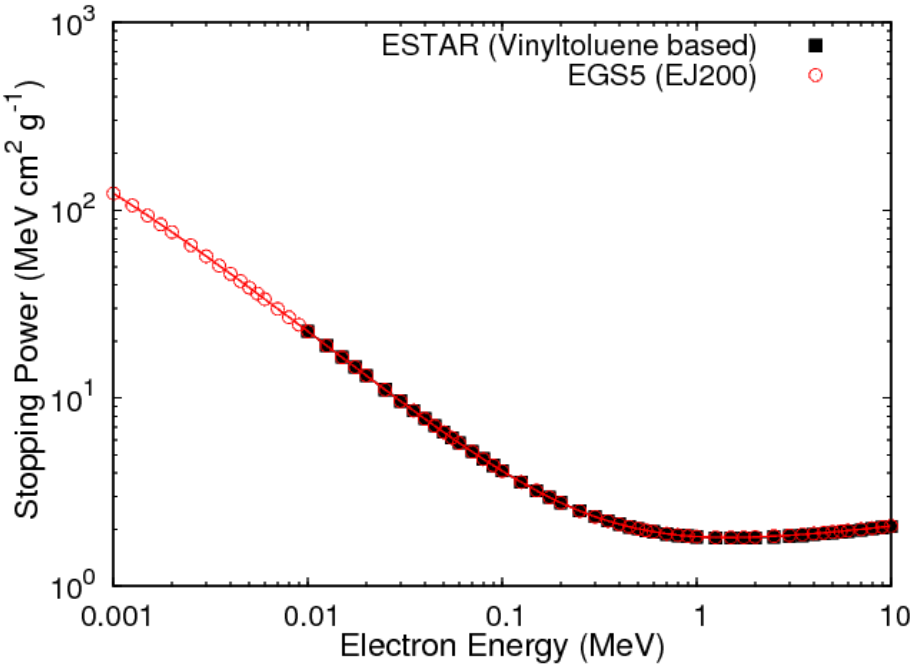

Figure 12 Total stopping power of electrons (*dE/dx*) passing through the plastic scintillator. The closed square is the data of the vinyltoluene-based scintillator from the ESTAR database [20]. The data for the scintillator (EJ-200) were calculated down to 1 keV by EGS5 code as open red circle.

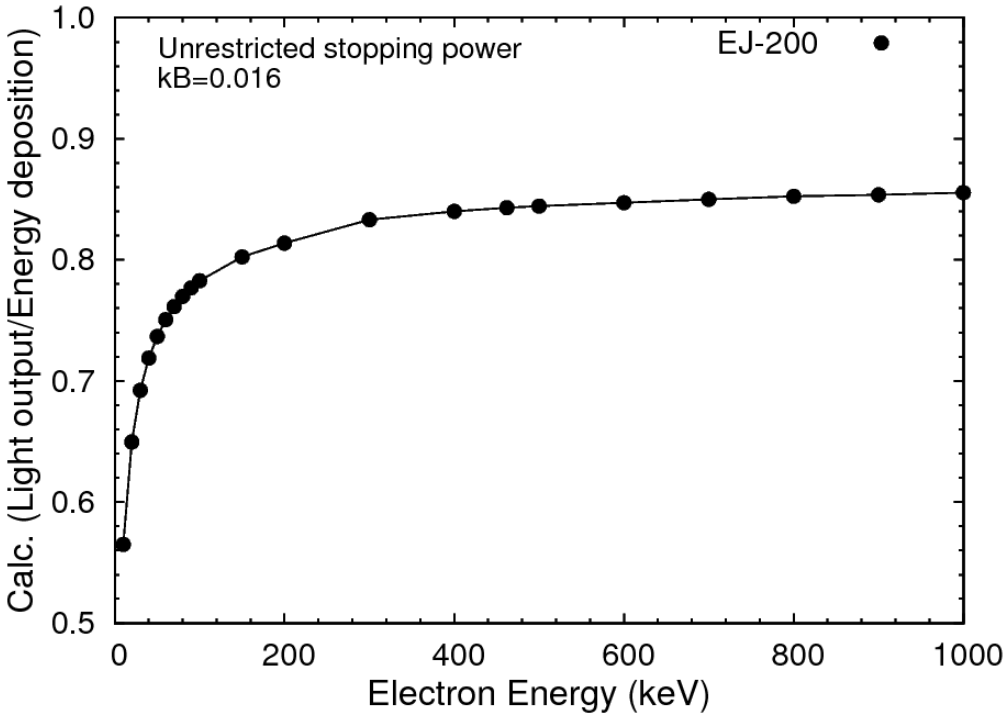

Figure 13 The ratio of calculated light output to the electron energy deposition for a *kB* value of 0.016 g cm^{-2} MeV^{-1}. At 0.462 MeV, the normalization factor is 1.186 and is applied to the light output results of EJ-200.

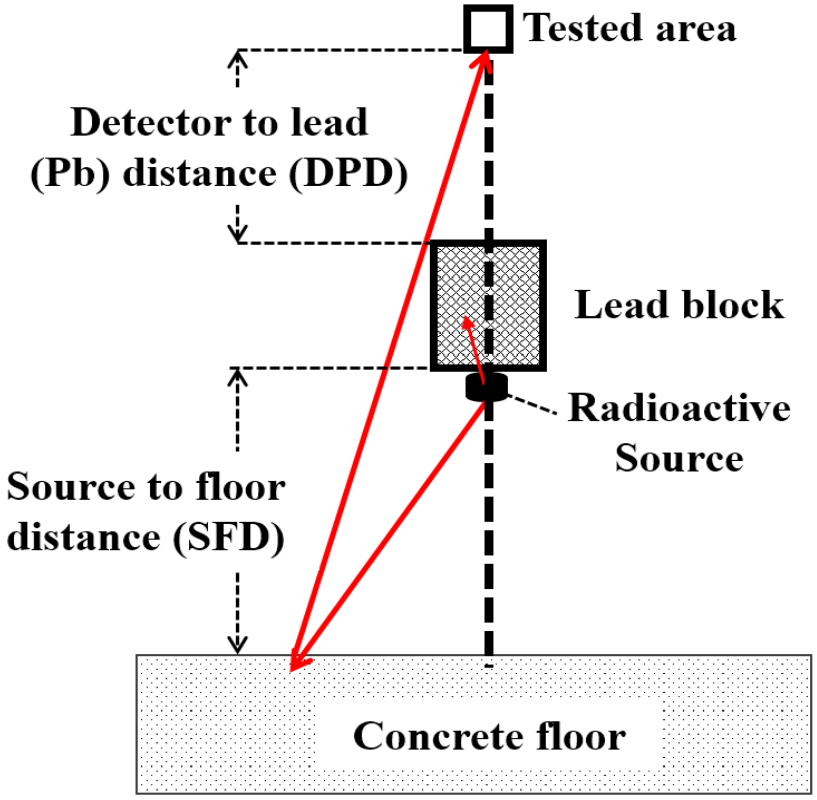

Figure 14 Basic setup of backscatter layout. The primary photons of the sources were absorbed by the lead block. The backscattered photons with energy of ~200 keV detected at the tested area as a result of Compton scattering with the floor by a large scattering angles.

Table 3 Example of layout parameters of Figure 14.There are four parameters would be optimized; lead block sizes, source to floor distance (SFD), scattering material, and detector to lead distance (DPD).

Layout parameters	Value of parameters
Lead block	10 cm x 10 cm x 10 cm
Source to floor distance (SFD)	20 cm
Scattering material	Concrete floor of 1 m thickness
Detector to Pb block distance (DPD)	15 cm

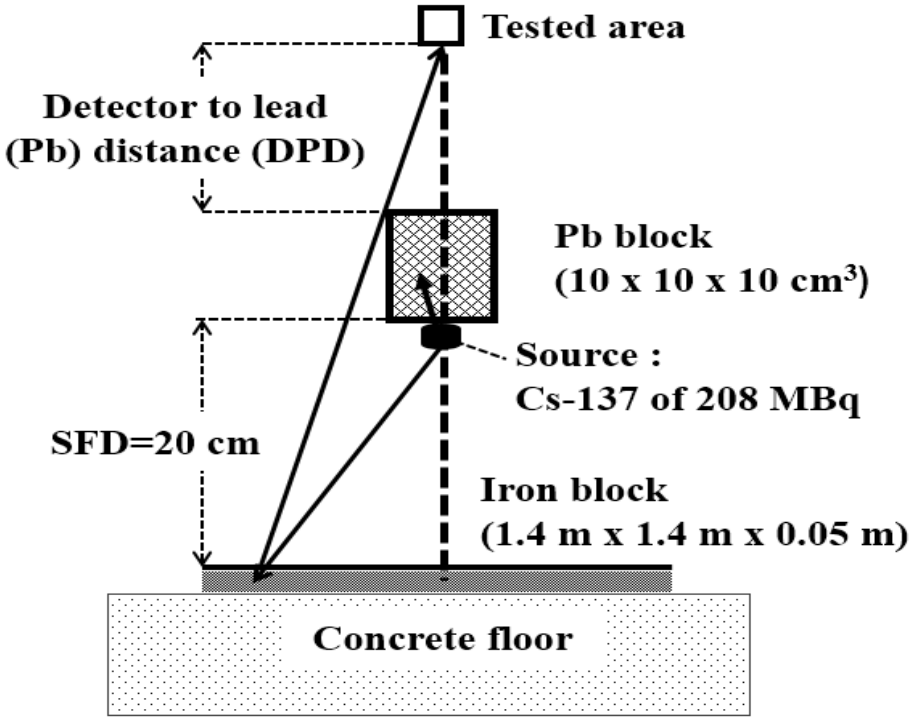

Figure 15 Partly optimized the setup of backscatter layout. The schematic consists of arbitrary (DPD) and the other optimized parameters. The tested area was investigated by optimizing the DPD parameter both vertically and horizontally.

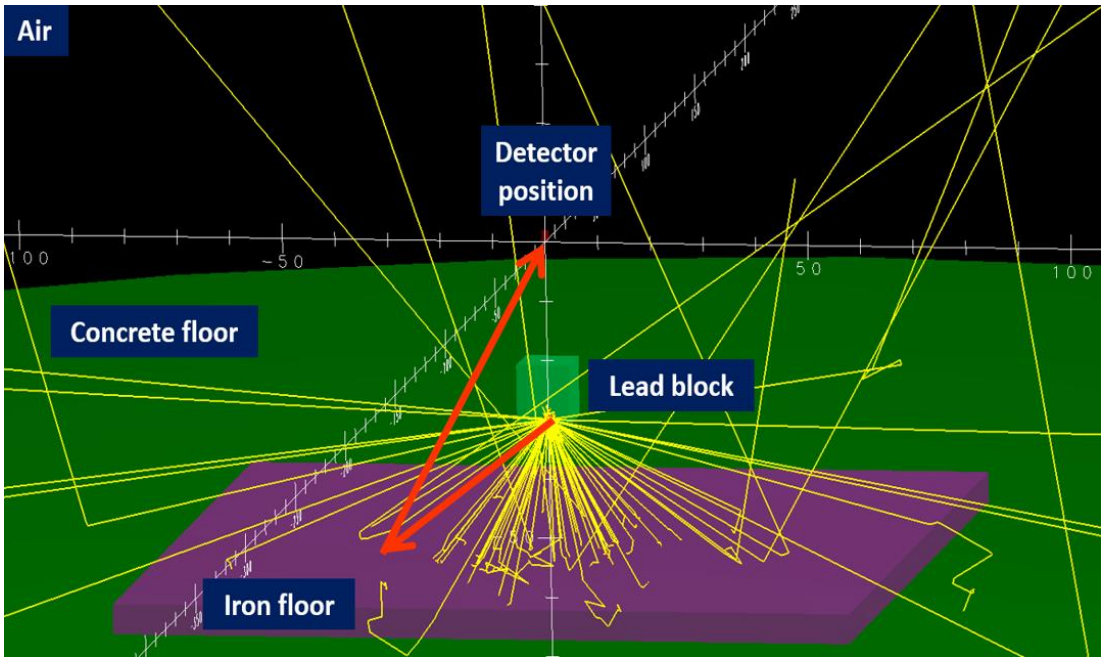

Figure 16 The backscatter layout modelled in EGS5-CGview as Figure 15. Calculation performed on square of Iron blocks 1.4m x 1.4m area x 0.05m thickness on cylinder concrete floor of 3m radius with 1m thickness. Most of the scattered photon scored were mainly from the Iron floor.

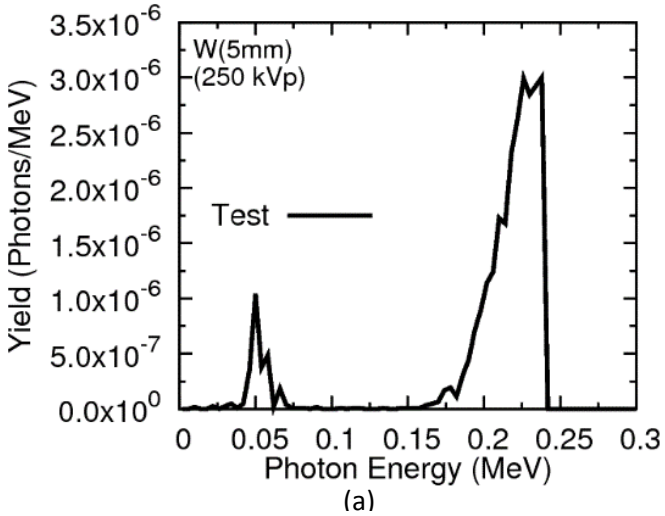

(a)

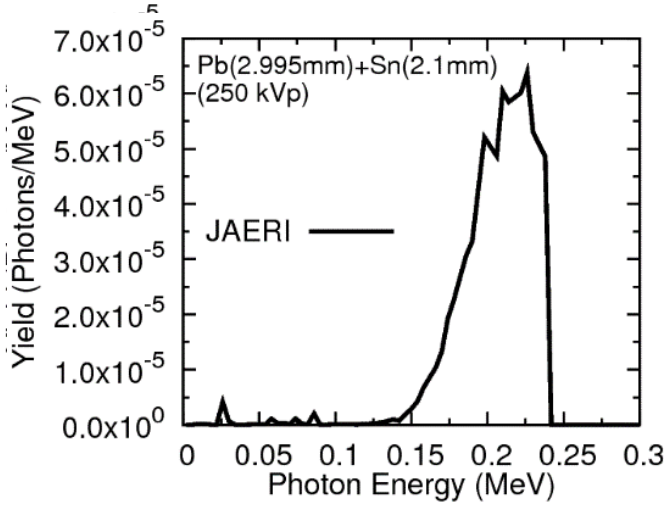

(b)

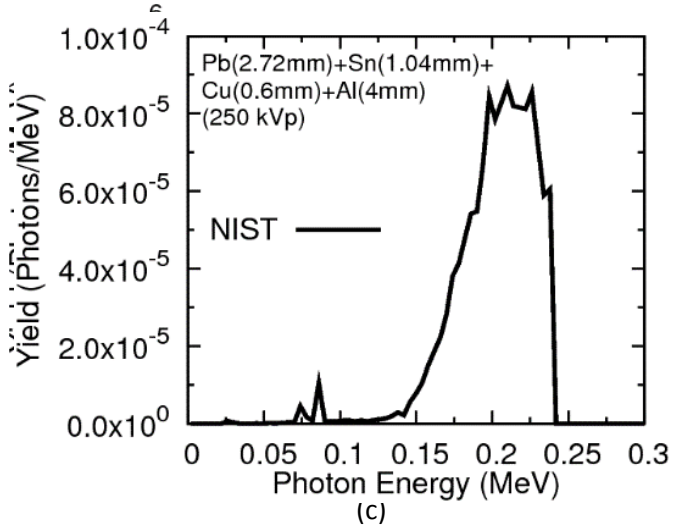

(c)

Figure 17 Overview of the calculated photon spectra for X-ray of 250 kVp. In (a) is the proposed filter of tungsten (W). In (b) and (c) are the calculateded filters of JAERI and NIST, respectively. The mean energy for filters (a) to (c) are 203, 209 and 206 keV, respectively. A K X-ray peak of the filter tungsten yield is obvious in (a).

Table 4 The list of check sources used for measurements. The sources activity ranging from 120 to 400 kBq (as on 01.01.2015).

Code no	Serial No.	Source	Energy (MeV)	Branching ratio (%)	Activity (kBq)
QCR310	NY 235	Am-241	0.06	35.9	405.2
CT402	579	Co-57	0.122	85.6	263.2
QCR310	NY237	Cs-137	0.662	85.1	348.9
MN402	579	Mn-54	0.835	83.5	323.6
QCR310	NY239	Co-60	1.173 1.332	99.9 100	122.3

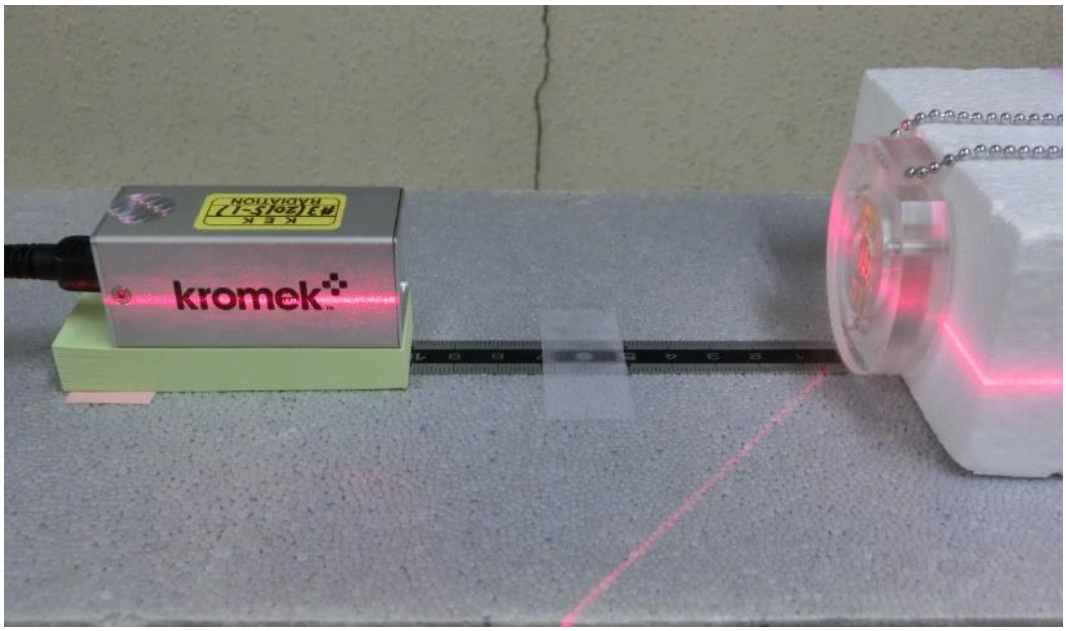

Figure 18 The experimental setup used for measuring the absolute peak efficiency values. The gamma sources was aligned to the CZT front surface at a distance of 10 cm. The measured values obtained were compared to the literature and calculated data.

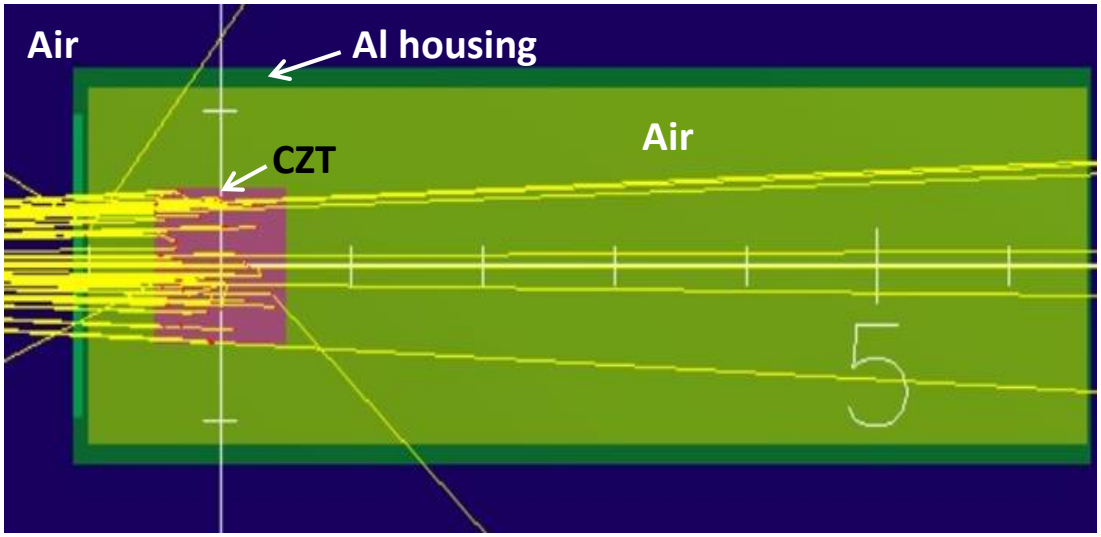

Figure 19 The model of CdZnTe 1cm^3 crystal (KROMEK, Model GR1) in EGS5-CGview for particle trajectory. The outer case is aluminum of 1.2 mm in thickness. The window is aluminum of 0.5 mm in thickness. The distance from the window to the surface of the crystal is 5 mm. The density is 5.86 g/cm^3. The proportion numbers of CZT material components are 0.9, 0.1, and 1 for Cd, Zn, and Te respectively.

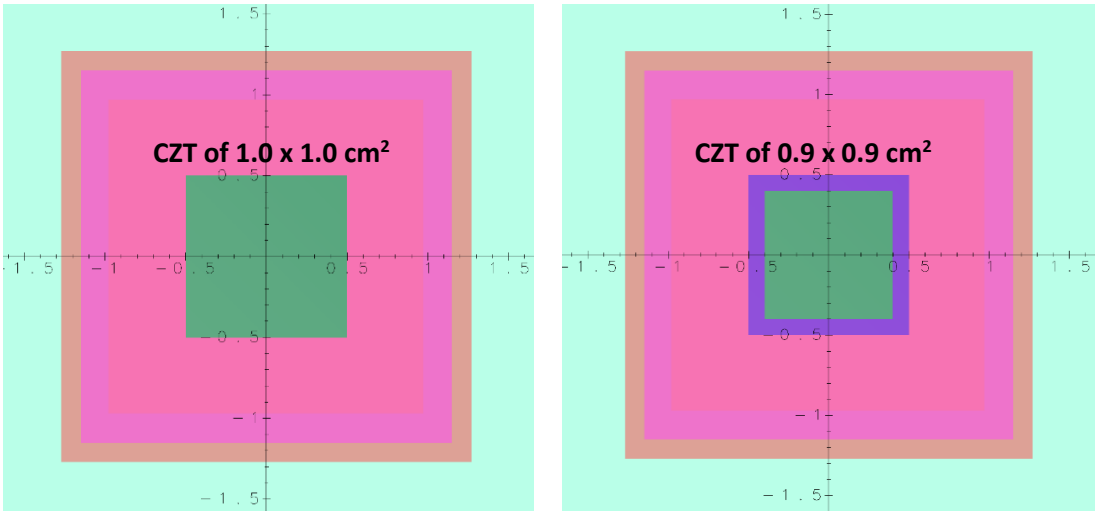

(a) (b)

Figure 20 The calculated crystal areas of CZT from the front view. Several areas of the crystals were calculated. Figure (a) is the original area of 1.0 x 1.0 cm^2 and (b) is 0.9 x 0.9 cm^2 area of the region used to score in calculation while remaining its original size.

4 RESULT AND DISCUSSIONS

4.1 DEVELOPMENT OF DETECTOR

4.1.1 Calibration of plastic scintillator

Energy calibration of an organic scintillator is performed by gamma ray sources. The positions of the Compton edge in pulse height spectra that have known energy values will be identified. However the Compton edge is normally very broad. It is difficult to determine the exact point corresponding to that particular Compton electron energy. Several researchers have made use of the Compton edge for energy calibration. For example Miyajima et al [41] obtained a linear energy calibration curve for NE102A scintillator by with several high-energy gamma sources. The sources used were Mn-54, Bi-207, Co-60, Na-22 and Tl-208.

There are three possibilities for the positions of the Compton edge as depicted in Figure 21; the Compton maximum (E_m) where the channel value is at the highest part of the Compton edge in pulse height spectra, the half-height of Compton maxima (E_h) in pulse height spectra, and the true Compton edge (E_e) where the position is in between E_h and E_m.

A.A Naqvi et al. [42] studied NE213 (5 cm in diameter x 5 cm long) and mention that the separation between the real Compton edge position, E_e with the half of Compton maxima, E_h is proportional to the detector resolution. In a similar study, Swiderski et al. [43] compared the separation of E_e to the Compton maxima itself, E_m of BC408 (4 cm in diameter x 5 cm long).

For comparison with the EJ-200 (5 cm in diameter x 5 cm long) used in this study, the E_m position was determined directly from the pulse height analyzer. While the half-height of Compton maxima, E_h was obtained by fitting the Compton edge region of interest (see Figure 22). A Gauss-error function was used to fit the Compton edge region as:

$$f(x) = a \operatorname{erf}\left[\frac{(x - x_o)}{b}\right] + c, \qquad (7)$$

where the control parameter *c* is the half counts of Compton maxima and x_o is the output for the channel number corresponding to the location of its half-height (E_h).

Many researchers use several fitting functions and Monte Carlo simulations to determine the position of the Compton edge. For example, Proctor & Wellman [44] used a straight line fit to the linear part of the Compton edge and extrapolated a zero count. While A.A. Naqvi et al [42] and L. Swiderski et al. [43] used a method based on a back-scattered coincidence measurement to measure the position of the Compton edge in organic scintillators. γ-γ coincidence technique was widely applied when the position of the Compton edge needs to be determined precisely. In this section, the position of the Compton edge relative to the position of the Compton maximum and the half height of the Compton maximum will be discussed.

Three mono-energetic gamma ray sources of higher energy such as Cs-137, Mn-54 and Na-22 were employed. Both direct and γ-γ coincidence spectrum were acquired for each sources. The results for Cs-137, Mn-54, and Na-22 sources are shown in Figure 23(a)-(c) of EJ-

200 that is 5 cm long. The 200 ns time window was applied for Cs-137 and Mn-54. Na-22 has a pair of 0.511 MeV photons from the annihilation process where a pair of gamma rays are detected in both detectors in coincidence events. A narrower time window of 25 ns was applied gated on after the coincidence events.

The results of the Compton electron spectrum for each gamma sources show a Gaussian shape peak. The centroid and FWHM of the distribution were determined with a Gaussian fitting to represent the Compton edge position as shown in Figure 23 (a)–(c). Figure 24 (a) to (c) are corresponding energy calibration curves for 5 cm EJ-200, 1 cm EJ-200 and 1 cm EJ-256, respectively. The error bar shows the error of peak position.

The summarized results of the position of the Compton edge are shown in Figure 25 (EJ-200; 5.1 cm diameter x 5 cm long). All three Compton edge positions were fitted linearly. The positions of Compton edges were compared to each other (Table 5 and Table 6) to understand the pulse height resolution. The measured and literature data show the same tendency where the E_e shifts relative to E_m or E_h and decreases as the energy of the Compton electron increases. This demonstrates that the energy resolution is better towards higher energies. From measurements, the deviation of E_e to E_m is from 5.4 to 4.2 % while the deviation of E_e to E_h is from 8.3 to 4.5% for Na-22 (511 keV), Cs137 and Mn-54 sources. It was observed that the Compton edge (E_e) is closer to the Compton maxima (E_m) than the half-height of the Compton maxima (E_h) for all γ-sources. From this relative position of the Compton edge, it could be concluded that the typical assumption that the Compton edge corresponds to the half-height of the Compton maxima is inadequate for this scintillator model. Instead, it is better to use the Compton maxima for rough energy calibration of the scintillator.

4.1.2 Electron response of plastic scintillators

Two calibrated NaI(Tl) (BICRON) reference detectors with a diameter of 7.62 cm and length of 7.62 cm were used at the same time for CCT. Figure 26 (a) & (b) shows the energy calibration curves of the two reference detectors using photo-peak positions of known gamma ray energies. The error bars were determined from the error of peak position.

The recorded data of CCT are processed in accordance with the following procedure: (1) First, events having time stamps within a specified time window of true coincidence events are selected as coincidence events from a large number of events recorded. The term “time” refers to the time of arrival of a pulse in both target and reference detectors. The time window for coincidence events is 10 channel steps for the total time window of 50 ns, as described in section 4.1.1. Figure 27 shows a two-dimensional scatter plot for the pulse heights of an EJ-200 target scintillator and reference detector. (2) Next, from the scatter plot, Compton scattering events are identified and sorted into a histogram of pulse height data for the target scintillator. The Compton electron energy was calculated by Equation 3. (3) Then the peak channel of the histogram is deduced by using a Gaussian fitting representing the light output corresponding to the Compton electron energy. Figure 28 shows the Compton electron energy spectrum for the EJ-200 scintillator and its corresponding Compton-scattered photons deposited in NaI(Tl) as measured by CCT for several scattering angles. (4) Finally, the ratios are computed between light output (3) and the deposited electron energy (2) to yield the electron response, L/E_e.

The uncertainties in the relative light yields such as counting statistics, centroid calculations and calibration have been discussed by Rooney et al [24] to be less than 0.6 %. For the measurements reported here, the peak position uncertainty ($\sigma_{E\gamma'}$) was calculated as Equation 8 [45]. It introduces an uncertainty of less than 1 %.

$$\sigma_{E\gamma'} = \frac{FWHM}{2.35\sqrt{N\gamma'}} \tag{8}$$

Here *FWHM* is the full width at half maximum of the peak and $N\gamma'$ is the total counts under the peak. The uncertainty of both reference detectors for conversion from channel number to energy are 0.048 and 0.045 % respectively. The error was calculated as the propagation error of the linear equation established for each reference detectors. For each run, the average NaI(Tl) instability was estimated to be 1.5 % (620 ch ± 9 ch for Cs-137). In the case of the target scintillator, the scintillator and photomultiplier tube performance were assumed constant throughout the measurements.

The chance coincidences depend on the width of the time window for the coincidence events in both the target and reference detectors. Due to a narrow time window (within 50 ns), the rate of contamination from background scattering or by chance-coincidence was low compared to coincidence events as shown in Figure 27. Therefore it was anticipated that the chance-coincidence events would have no impact on the obtained energy spectrum. The value of the time window as a function of the scattering angle are shown in Table 7.

4.1.2.1 Calculation of the CCT geometry

PHITS code of the version 2.76 [53] was used to simulate the CCT geometry to check the data quality of the measurement. The same size of the target and reference detectors was modelled in the calculation. The distance between the target and reference detectors is 40 cm as per experiment. The calculations were performed for several scattering angles. The measured scattered photon for several angles were compared with calculated one (see in Figure 29). The output of PHITS calculation were fitted to the Gaussian for its peak centroid. The difference of measured to calculated peak centroids values are within 2 %. The calculated spectra peak width was not included the NaI(Tl) detector resolution, showing the inherent width due to the geometry of CCT. Figure 30 shows the effect of distance between the target and reference detector at the angle of 25 degree. The spectra of distance less than 30 cm have a broad inherent width and higher detection efficiency as a result more scattered photons from deposited. The peak was not adequate for Gaussian fitting. The narrower and Gaussian shape peak was observed as the distance between both detectors above 30 cm. Thus, it is recommended that the distance between both detectors to be at least at 30 cm.

The effect of angle uncertainty (± 1 degree) was also evaluated as shown by Figure 31. The 1 degree uncertainty is corresponding about 1 cm shifted of the NaI position to the particular angle. The calculated scattered photon spectra was calculated at a distance of 40 cm from the target scintillator as per experiment. Three angles were calculated at 24, 25 and 26 degree to understand the impact of NaI angulation on the spectra. Each spectra was analysed for its peak centroid by the Gaussian fit. The percentage of different either 24 or 26 to the angle of 25 degree is within 0.86 %. Thus, the impact of different angle within 1 degree was very small.

Figure 32 shows the relative light output per unit of electron energy deposited for both plastic and NaI(Tl) scintillators together with the data obtained from previous studies. The data of BC-408 (40 mm diameter x 50 mm long) from the literature was plotted together [46] as BC-408 is equivalent to the model of EJ-200. The author had measured the electron response from the technique of wide angle Compton coincidence. The response of the plastic scintillator decreases significantly below 150 keV as the electron energy decreases. The degradation of light output shows the effect of ionization quenching as the stopping power of free electrons increases for lower electron energies. In contrast, NaI(Tl) data increases with decreasing electron energy. The measurements with NaI(Tl) supports the data from the literature [24], validating the measurements performed with a plastic scintillator. However, it is clear that the response somehow disagree at the point of 350 keV. This disagreement was mainly due to the calibration error of an individual reference detector calibration of (NaI(Tl); 2" x 2") used for a particular angle. The deposited energy of Compton-scattered γ-rays was found to be lower than the theoretical energy of Compton-scattered photon energy at the same scattering angle of 75° by 7.2 %. Thus it would yield the lower light output per electron energy absorbed in the target detector. Nevertheless, the observed disagreement at 350 keV data would not affect the results of the EJ-200, which are measured by the same two reference detectors (NaI(Tl); 3" x 3").

The value of the Birks parameter (kB) was extracted from the shape of the light output curve. Figure 33 shows the least squares result of comparing the light output measured during this experiment with Birks formula for different kB values. The least square minimization (x^2) was calculated by:

$$x^2 = \sum_{i=1}^{n} (M_i - C_i)^2 \qquad (9)$$

where M is the experimental data and C is the number generated by the Birks formula (2). When the plot curve of kB=0.016 is compared to the experimental data, the reduction of light output is consistent with experiment, as shown in Figure 34. The extracted value is important to be use in calculation of absorbed energy while considering the electron response.

4.1.3 Comparison of measured and calculated pulse height distribution

Energy resolution is important in the successful comparison of calculations with measured results. The photopeak of Am-241 was acquired by direct measurement as shown in Figure 35. The measured photopeak of main gamma from Am-241 at 59.5 keV was analyzed to obtain the *FWHM* value. Figure 35 (a) shows that the measured spectrum of Am-241 was fitted by exponential (green) and Gaussian (red line) functions. The *FWHM* was deduced by a Gaussian fit after subtracting the exponential part as shown in Figure 35 (b).

Figure 36 to Figure 40 show the comparison of measured (M) and calculated (C1 and C2) pulse height spectra for Am-241, Co-57, Cs-137 and Mn-54 sources, respectively. In each figure, the comparison is shown for each scintillators of EJ-200 and EJ-256 (0.5 % Pb) labelled with (a) and (b), respectively. The typical shape of the pulse height spectra seen in the low Z plastic scintillator are presented in Figure 38 to Figure 40. The results show that there is no photon photopeak in the case of Cs-137 and Mn-54 sources. It is associated mainly with the

scattering process in the plastic scintillator from high-energy photons. For Am-241 and Co-57 sources, a few of the primary photons from the primary photons undergo photoelectric interactions as seen in Figure 36 and Figure 37 (note that the counts are on the log scale for both figures).

Generally, the Compton edge peak widths reproduced by the calculated spectra are in reasonable agreement with experiment for all gamma sources. By using the photopeak of Am-241 source, Equation 5 is adequate to smear the initial calculated spectra of all other sources once we know the value the photopeak energy (from the calibrated measured spectra) and its *FWHM*.

There are two figures show the comparisons for the Cs-137 source; Figure 38 and Figure 39 . In the Figure 38, the comparison of the spectra shows the agreement part only at the Compton edge peak and disagreed after the Compton edge peak. This result are in agreement with other researchers [[14], [15]]. In this study, the agreement was further improved as depicted in Figure 39. A thin Al (2 mm) was added in between the source and scintillator for re-measurement and calculations. The agreement of the experimental data and calculated spectra (C1 and C2) was achieved for the entire spectra. The purpose of adding thin Al is to block the beta ray emission from the Cs-137 source. The well agreement also was achieved for Mn-54 as shown in Figure 40.

The effect of non-proportionality in the plastic scintillator is clear from Figure 36 and Figure 37 for low energy gamma sources, Am-241 and Co-57, respectively. When considered the scintillator non-proportionality (ionization quenching) in the same calculation, the disagreement between measurement and calculation is improved considerably as depicted by the C2 spectra in the same figures.

The effect of lead doping on the pulse height spectra could be seen in Figure 41 (a) and (b) for Am-241 and Mn-54 sources, respectively. Figure 41 (a) shows that the lead doped improved the detection efficiency and energy absorption with higher pulse height in comparison to standard plastic scintillator. In the case of Mn-54 sources, both the measured and calculated results agreed that there is no significant contribution of the lead doping on the pulse height spectra as depicted in Figure 41 (b). The influence of the optimal concentration of lead doping scintillator with soft-tissue dose will be discussed in the section 4.1.5.

The study shows that calculation results are in consistent agreement with corresponding experimental data of both scintillators, EJ-200 and EJ-256 (0.5 % Pb). To summarize the agreement between the calculated and the experimental data is satisfactory. The agreement will be discussed in the next section from the viewpoint of absorbed dose.

4.1.4 Absorbed dose from pulse height distribution spectra

The absorbed dose (Gy) was obtained by summing up the absorbed energy (MeV) deposited in the scintillator from the pulse height distribution spectra. The total absorbed energy was then divided by it mass to yield the output in the unit of MeV/g. Following conversion were used to convert the unit of MeV/g to Gy;

$$1 \text{ MeV} = 1.602 \times 10^{-13} \text{ J} \quad (10)$$

$$1\ \text{MeV/g} = 1.602 \times 10^{-13}\ \text{(J/MeV)} \times 1000\text{(g/kg)} = 1.602 \times 10^{-10}\ \text{Gy} \quad (11)$$

The energy threshold of the summation is 20 keV. Because the plastic scintillator composition is close to soft-tissue, any deposited energy into plastic scintillator would be similar to soft-tissue of the same size.

The measured pulse height spectra of each 1 cm long scintillators (EJ-200 and EJ-256 0.5% Pb) were calibrated by using the established energy calibration line as shown in Figure 24 (b) and (c). The absorbed dose was deduced from the calibrated pulse height spectra as in Equation 12;

Absorbed dose (MeV/g);

$$= \sum_{\text{i=0.02 MeV}} \frac{\text{Counts of channel i x Energy of channel i (MeV)} x \text{ Energy bin width}}{\text{volume (cm}^3\text{) x density } \left({}^{\text{g}}/_{\text{cm}^3} \right) \text{ of scintillator}} \quad (12)$$

The proper energy calibration procedure is important for the accuracy of absorbed dose measurement. For the measurements reported here, the absorbed dose was evaluated from the pulse height spectra as mentioned in section 4.1.3. No correction was applied to the developed calibration curve as the Compton edge of the higher energy sources (Cs-137, Mn-54 and Na-22) were fitted linearly and were close to the origin.

The uncertainty of the measured absorbed dose was evaluated as a statistical uncertainty due to counting statistics of the measured net counts ($\sqrt{n}$). For the measurements reported here, the counting statistics give an uncertainty of less than 4.5 % and 3.1 % in the absorbed dose of EJ-200 and EJ-256 (0.5 % Pb), respectively. The distance from the source to the scintillator throughout the measurements was estimated to produce an error of 1.5 %.

Table 8 and Table 9 shows the results of measured and calculated absorbed dose for the scintillator of EJ-200 and EJ-256 (0.5 % Pb), respectively. These absorbed dose values were derived from the pulse height spectra as shown in Figure 36 to Figure 40 for Am-241, Co-57, Cs-137 and Mn-54, respectively. In the case of Cs-137 and Mn-54 sources, the measured absorbed dose by EJ-256 is higher than EJ-200 by 4 %. There is a significant effect of lead doping for lower gamma sources of Am-241 and Co-57. The ratio of absorbed dose in EJ-256 to that in EJ-200 is 3.6 and 1.2 for Am-214 and Co-57, respectively. Adding lead at 0.5 % of the total plastic scintillator weight significantly increased the photoelectric absorption of low energy gamma photons with a lower effect on higher energy sources. These results suggest that using a single concentration of lead doped is adequate for photon dosimetry in a wide energy range.

Table 10 shows the summarized results for the ratio of calculated to measured (M) absorbed dose of both scintillator EJ-200 and EJ-256, respectively. The calculated absorbed doses were considered in two situations: C1 for energy absorption and C2 is an energy absorption including the quenching effect as discussed in section 3.1.5. For higher energy gamma sources such as Cs-137 and Mn-54, the ratio of either C1 or C2 to the M are within 6 % in both scintillators of EJ-200 and EJ-256. For Am-241 sources, both scintillators disagree up to 40 % (C1/M). The difference was improved to 13 % (C2/M) once quenching effects were considered. The results indicated that the energy response was much affected on the absorbed dose of low energy gamma sources rather than higher energy gamma sources.

To summarize, the degradation energy response of the plastic scintillator distorted much of the absorbed energy towards low energy photons. This effect requires a compensation for soft-tissue dose. Lead-doped plastic scintillator is a good candidate to compensate the underestimation of absorbed dose by standard plastic scintillator, particularly for low energy photons.

4.1.5 Compensation of underestimation for soft-tissue dose

In the previous study, the compensation of dose underestimation in the low energy region had been proposed by doping the plastic scintillator with higher atomic material. The idea for this investigation is that the addition of a high Z element to plastic scintillator in small proportions offers substantial increases in gamma interaction probability at energies below 200 keV.

In this section, the absorbed dose of the standard and several concentration of lead doped plastics scintillator will be compared to the soft-tissue through calculation. Both energy absorption and quenching effect will be considered in the calculation of plastic scintillator absorbed dose.

The absorbed dose in the scintillator and soft-tissue of the same size were calculated for the parallel photon beams. Figure 42 shows the geometry modelled in EGS5-CGview for the calculation of absorbed dose. While maintaining the diameter of both scintillator and PMT, the parallel photon beams were incident on the plastic scintillator (5 cm long) which is coupled to the PMT window (5 mm long). In the case of soft-tissue, the calculation is without the PMT window. The scintillator materials data are generated with the MIXT option of PEGS. The plastic scintillator materials data are the same as in section 3.1.5. The elemental compositions of the soft tissue is based on its atomic weight proportion as described in Table 1. The density is 1.0 g/cm^3.

For the first case, the absorbed dose in the scintillators (EJ-200 and EJ-256; 0.5% and 1.0 % Pb) was calculated where only energy absorption was considered. For the second case, the same subroutine of electron response and normalization factor value as in section 3.1.5 was applied. The calculated absorbed dose of the scintillators was then compared with the calculated soft-tissue dose.

Figure 43 shows the ratio of a calculated absorbed dose of plastic scintillators model of EJ-200, EJ-256 (0.5% Pb) and EJ-256 (1.0% Pb) to the soft-tissue (of the same size) as a function of incident photon energy. The purpose of this figure is to show the feasibility of lead-doped scintillator to compensate the underestimation of tissue dose by standard plastic scintillator, particularly in the low energy photons region.

Initially, the ratio was calculated based on absorbed energy showing a strong overestimation of the soft-tissue dose from both concentration of lead-doped scintillator (0.5 and 1.0 %). In contrast, a standard plastic scintillator (EJ-200) would underestimate a soft-tissue dose under 150 keV incident photon as shown in Figure 43 (a). This is expected since the effective atomic number of the plastic scintillator is lower than that of the soft tissue. By considering the quenching effect in the calculated absorbed dose, the 0.5% of the lead-doped plastic scintillator is evidence for soft-tissue dose equivalent, making it ideal for low-energy photon dosimetry as shown in Figure 43 (b).

4.1.6 Summary development of detector

In this study, the electron response was obtained experimentally using the Compton coincidence technique because it is necessary in obtaining absorbed dose from light output spectra. The electron response as a function of electron energy was not linear and was found to decrease significantly below 150 keV. The degradation of electron response could be explained with the quenching effect in scintillator by using the model developed by Birks, where the high ionizing density along the particle track in scintillator would be responsible for the reduction of light yields i.e. quenching effect.

With the measured results of plastic scintillator electron response, it was also possible to apply the same response to a doped plastic scintillator such as silicon-, bismuth- or lead-doped materials in a photon dosimetry study. In this study, a commercially available lead-doped scintillator (EJ-256) was chosen as the candidate.

The light outputs were well fitted with the results obtained by the equation derived by Birks within errors of 3-13% for photons of energies from 59.5 to 835 keV, and a value of quenching parameter could be obtained. The absorbed dose in scintillator from a few tens of keV to MeV was assured to be well calculated once a constant quenching parameter was applied in the calculation. In addition, the calculations suggested that the underestimation effect could be compensated by doping heavy materials such as lead into the plastic scintillator.

The lead doped scintillators compensated for the underestimation of the soft-tissue absorbed dose from standard plastic scintillators. Through calculation, a correction based on the degradation of electron response in low-energy regions compensated well the effect of over-response of lead doped scintillator to 15 % and -5 % for Am-241 and Co-57. By considering the quenching effect, could extend the usefulness of the plastic scintillator to dose measurements by a soft-tissue dose. Finally, the performance of lead-loaded scintillators was shown to be better for photon dosimetry, particularly in the low-energy region.

4.1.6.1 Effect from surrounding material

A plastic scintillator requires a device that collects scintillation light and converts it to an electronic signal. When a small plastic scintillator coupled with a photo-multiplier tube (PMT) is employed as a dosimeter, a PMT window of considerable size and weight exists on the side of the PLS. There is a possibility that the PMT window glasses will influence the absorbed dose when thin plastic scintillators are used. The contribution of backscattered photon and electron from the window were evaluated using an EGS5 code.

The parallel photons beam of the same radius with the scintillator was set to incident on the front face of the scintillator. The electrons or photons generated in the window that were backscattered to the scintillator were identified. The absorbed energy in the scintillator was scored separately by considering the contribution of reflected photons or electrons from the window. For comparison, the absorbed energy was also scored without the window. Figure 44 shows the geometry of the scintillator and particles trajectory of the photons used in the calculation.

Figure 45 shows influence due to reflected photons and electrons and the calculated result of 5.08 cm in diameter and 0.05 cm long for a plastic scintillator with and without a quartz window. There is also a significant additional dose from a PMT quartz window for 400

to 1000 keV photons (20 % to 43 %) in comparison to one without quartz. To reduce the unexpected additional dose, a plastic scintillator with considerable thickness in comparison with a PMT window thickness should be adopted for the 'soft-tissue' dose response.

4.2 DEVELOPMENT OF CALIBRATION FIELD

4.2.1 ~200 keV photon field by backscatter layout

By using a Monte Carlo simulation, EGS5 code, the typical calculated photon spectra of backscattered radiation from the Cs-137 source was given in Figure 46. The calculation was performed under the backscatter layout with the parameters, as listed in Table 3. The detector response was not considered in the calculated photon spectra.

The measured pulse height spectra in Figure 47 were obtained under this layout by a 1 cm^3 CZT detector (KROMEK, GR1). The red and black dotted represent the measured data with and without the lead block, respectively. The main gamma of 662 keV was blocked when inserting a 10 cm x 10 cm x 10 cm lead block. The two peaks represent the unscattered photons of Cs-137 (peak at 662 keV) and the Compton-scattered photons from the concrete floor (backscatter peak at 190 keV). The total net count rate of the backscattered field with the lead block is smaller by a factor 11. Thus, the backscatter layout can be effectively used to produce the desired quasi-mono-energetic photons.

The calculated peak energy of the backscattered photons under this layout is 190 keV and corresponds to a scattering angle of 156°, according to Equation 3. The low energy component of the peak that was caused by multiple Compton scattering inside the concrete floor should be minimized.

4.2.1.1 Backscatter Layout Optimization by Calculations

For the backscattered field calculations, a lead block area of 10 x 10 cm was selected as an adequate size, considering the calibration fields used for many dosimeters and detectors. By keeping the area constant, the necessary lead thickness was estimated. Assuming there was no other material except air in the vicinity, the attenuation of the 662keV photons from the Cs-137 source was calculated at 25 cm distance using the EGS5 code. Figure 48 shows the calculation results for the attenuation (shielded dose rate, µSv/h) as a function of lead thickness (cm). As an example, a 10-cm-thick lead block would be sufficient to reduce a direct ray to 1/10 of the environmental radiation when use a 200 MBq Cs-137 source.

While keeping the other parameters for the DPD, the lead block, and the concrete floor fixed, as in Table 3, the photon spectra and ambient dose were calculated for SFDs of 0.5, 5, 15, and 20 cm. An SFD of 0.5 cm indicated that the source position was the closest above the concrete floor surface. The source position was aligned with the scoring region throughout the calculations. The calculated photon spectra showed that the highest peak-to-total ratio was obtained for an SFD of 20 cm when the source position was directly under the lead block, as summarized in Table 11. As the SFD decreases, the contribution from the low-energy component increases compared to the backscatter peak.

In order to enhance the backscatter peak and reduce the low-energy component, several additional materials were considered to use on the concrete floor. With the same backscatter setup, the backscattered photon field was calculated for five different scattering materials from low to high atomic number (such as C, Al, Fe, Cu, and Sn). For comparison purposes,

their sizes were fixed at an area of 5 m x 5 m and a thickness of 1 m. While using the optimized SFD value of 20 cm, the backscattered photon spectra and doses were calculated at a DPD value of 15 cm. The relationship of the calculated air absorbed dose (Gy/incident photon) and peak-to-total ratio of the photon spectra as a function of scattering material is presented in Figure 49. The higher atomic number materials, such as iron, copper, and tin, displayed higher peak-to-total ratios, while carbon and aluminum were not recommended owing to their low peak-to-total ratios. The lower energy components of the spectra were reduced owing to lower multiple scattering inside the scattering materials with higher atomic numbers.

However, the calculated air absorbed dose decreases almost linearly as a function of atomic number. Since the probability of photoelectric interaction increases with the atomic number of the material, the yield of escaped backscattered photons decreases with increasing atomic number. Thus, a reduction of photon dose can be expected. By considering both factors, iron was determined to be the best among these five scattering materials because it provided a reasonably high peak-to-total ratio and featured only a small reduction in the dose. Subsequently, the optimum dimensions of iron on the concrete floor were calculated.

Assumed that iron squares (5 cm thickness) of various sizes were placed on the concrete floor. Figure 50 (a) shows the calculated dose rate as a function of side length of iron square for a Cs-137 source (208 MBq). All the calculations were performed using the optimized SFD value (20 cm) and a test DPD value of 15 cm. The values of both calculated dose rate and peak-to-total ratio were found to be nearly constant for an area of 1 m x 1 m or more. Figure 50 (b) provides useful information that the calculated dose rate and peak-to-total ratio are nearly constant at 3 cm iron thickness or more.

Adding a 1 m x 1 m square iron slab as thin as 3 cm on the concrete floor was sufficient to obtain better spectra of quasi-monoenergetic photons of ~200 keV; with this minimum modification, the peak-to-total ratio of the photon spectra reached its saturation value of 0.68. Because the Compton scattering interaction probability depends on the material's electron density, thicker materials would be required for low density floor materials (such as concrete or aluminum) to obtain a high yield of the backscattered photon field. Therefore, all subsequent experimental and theoretical studies were conducted using additional iron blocks on the concrete floor as scattering materials.

Figure 51 shows typical calculated spectra of the backscattered photon field of ~200 keV from the concrete floor (dotted line) and with the addition of 5 cm thick iron to the concrete floor (solid line). Adding an iron block on a concrete floor reduces the amount of lower energy components (≤ 155 keV) almost by a factor of 3. While the remaining lower energy components cannot be avoided due to multiple scattering, most have been successfully reduced by the suitable choice of iron thickness and area to keep the low intensity of low energy parts. The ratio of photons yields in the low energy components to the whole spectra for less than 100 and 170 keV are 0.03 and 0.21, respectively. Thus the high peak-to-total ratio was retained although the calculated backscattered photon spectra are quite broader than the real monoenergetic source.

4.2.1.2 Uniformity of the Backscattered Photon Field

4.2.1.2.1 Position Dependence of Spectra

The measured pulse height spectra and the calculated photon spectra at a DPD of 15 cm are shown in Figure 52 and Figure 53, respectively. The measurements were performed for two horizontal detector positions: at 0 cm (detector aligned with the source at the center) and shifted horizontally by 6 cm along each DPD plane (5, 10, 15, 20, 25, 30, and 40 cm).

The horizontal displacement of 6 cm was investigated because it covers several detector and dosimeter sizes. By fixing the horizontal position at 0 cm, the measured and calculated spectra were examined as a function of DPD (vertical direction). Both the measured and calculated data show that the full energy peak increased as a function of DPD by about 2 keV per 5-cm step, as presented in Figure 54.

This weak dependence of the spectral shape on DPD was observed when DPD was over 15 cm, where the calculated peak-to-total ratio differences between 5-cm steps were within ~3 %. Figure 55 shows that the maximum calculated peak-to-total ratio difference was only ~2 % as the detector position shifted 6 cm horizontally for each DPD.

4.2.1.2.2 Position Dependence of Dose Rate

The dose rate was calculated in vertical directions (at DPD values from 10 to 40 cm) and in the horizontal direction (per 2 cm steps) to confirm the uniformity of the backscattered field. The measured and calculated dose rates of the 208 MBq Cs-137 source as a function of DPD are presented in Figure 56. The maximum achievable dose rate was obtained when DPD was 15 cm.

The calculation result show in good agreement with experimental one at DPD longer than 10 cm when the radiation field is sufficiently uniform. However, the calculation result underestimate experimental data at DPD shorter than 10 cm. In this region, the dose rate increases with horizontal distance, especially near DPD 0 cm. Since the surface area of the survey meters to take experimental data are larger than the scoring area of calculation (2x2cm), the underestimation of calculation in this region is reasonable. The region of shorter DPD (< 10 cm) is not adequate for study purpose.

The results agreed that the optimum DPD was in the 15 to 25 cm range, and featured less than 10% dose rate variation. The lower DPD range of 10 to 15 cm is not recommended owing to a strong dose rate dependence. The variation of the dose rates along the horizontal direction is shown in Figure 57 (a) and (b). The measured and calculated dose rates were obtained every 2 cm steps (from 0 to 6 cm) horizontally for all DPD planes. There was no significant dose rate variation found in the horizontal direction, which displayed less than 4 % dose rate variation (per 6 cm) for a DPD within the 15 to 25 cm range.

4.2.2 ~200 keV photon field by X-ray generator

Generally, above 200 keV filtered X-rays with a narrow peak width are difficult to obtain. As an example, Figure 58 shows the measured filtered X-rays spectra by Ludlum measurement Inc. with a CdTe (ICS-4000) detector [47]. The filtered spectra of the X-ray 200 kVp obtained is not monoenergetic X-rays. In this study, several recommended filters type and combinations were measured.

The stability of the X-ray output for specific settings (tube voltage and current) was determined by measuring X-ray tube dose rate every 5 s once the irradiation started. Figure 59 shows the measured dose rate as a function of irradiation time. For this measurement, about 40 s is necessary as a "time-trigger" for the stability of X-ray output.

Figure 60 a to c show measurements of filtered X-rays by using a CdZnTe detector. The detail properties of the measured spectra and its dose rate were shown in Table 12. Figure 60 (a) shows that using a strong single filter (^{74}W) is a good candidate to obtain narrow peak width for about 200 keV peak. The low dose rate is suitable for many environment dosimeters such as CsI(Tl) Horiba Radi PA-1000 [48] or Mr. Gamma A2700 [49] dosimeters whose measurement range is typically up to ~9.99 µSv/h. However, the characteristic tungsten K X-rays which were generated in the tungsten filter produce a large peak around 50 keV. 52% of the low energy component (below 150 keV) deposited in the spectra was defined as the unknown contribution. 13% was confirmed due to the room-scattered radiation via the shadow shield measurement. Consequently, all the filtered X-rays measured here gave larger energy width compared to the backscatter field.

4.2.3 Comparison of peak efficiency and pulse height spectra using CdZnTe detector

The energy width of the field was measured using CdZnTe detector. To compare the spectra of experiment and calculation, insensitive region of the CdZnTe crystal was estimated. The detector was applied to evaluate energy width of 200 keV mono-energetic field of filtered X-ray using an X-ray tube.

The absolute values and ratio of the measured and calculated peak efficiency are shown in Figure 61 (a) and (b), respectively. The literature values were also included. The measured and literature data [48] in well agreement. Both measured and calculated peak efficiencies decrease as a function of photon energy. Initially, above 100 keV the calculated peak efficiency overestimated the measured within 70 %. Below 100 keV the overestimation is within 35 %. The calculated value agreed with measured value within 5 % in a wide energy range when the "effective" area was reduced down to 0.8 x 0.8 cm^2.

The measured photopeak of Cs-137 was fitted by Gaussian function to obtain FWHM for smearing of calculated data as in Figure 62. The comparable of measured and calculated pulse height spectra is presented in Figure 63. The black dotted is the experimental data, the red, blue and green lines are calculated spectra for the crystal area of and 0.8 x 0.8 cm^2. The K X-ray peak, Compton edge and photopeak appeared at the correct energies with reasonable agreement of the peak widths. By comparing the red and green lines, a small peak around 200 keV was known due to the backscattered photons from the Al housing that surround the crystal. The photopeak reproduced by the calculation in close agreement to the measured one for the crystal size of 0.8 x 0.8 cm^2. The agreement in the Compton part was improved once considering the plastic source casing as indicated by the blue line.

The low energy tail of the photopeak in the measured spectra indicated an incomplete charge collection efficiency and short carrier mobility-lifetime especially for holes [50] & [51]. Bolonikov et. al [52] had demonstrated by the algorithm to identify the effect of incomplete charge collection efficiency which caused by the crystal defects or "bad" regions in CdZnTe detector.

4.2.4 Summary development of calibration field

The backscatter layout was established to obtain a quasi-monoenergetic 200 keV photon field using a radioactive source. The optimal parameter values of the layout are given in Table 13. A significant and stable measured dose rate of 3.18 ± 0.18 µSv/h (background dose rate of 0.055 ± 0.008 µSv/h) was obtained from a 208-MBq Cs-137 source by optimizing the backscattered radiation field (peak at 190 keV) with the appropriate layout. The volume of the uniform backscattered radiation field is presented in Table 14; the volume of 'uniform dose' was calculated as the volume of a box of $(6 \text{ cm} \times 2)^2 \times 10 \text{ cm} = 1440 \text{ cm}^3$.

The uniformity of the backscattered field was evaluated by considering two factors: the spectra (calculated and measured photon spectra) and the dose rate (calculated and measured dose rate). The uniformity in the volume was confirmed with a variation smaller than 10 % of the peak-to-total-ratio and dose rate.

Under the optimal backscatter layout arrangement, the percentage contribution of the dose rate value from low energy components (≤ 155 keV) were then investigated by calculation. Figure 64 and Table 15 shows that under the real situation (1.4 m x 1.4 m x 0.05 m square of iron blocks on concrete floor), 19 % of the dose rate value was contributed by the low energy components. The difference of low energy component between 100 % of iron material (Iron of 3 m x 3 m x 1 m) with real situation is 4 %. From this 4 % difference, it was found that only 1 % of the low energy component was contributed directly from the concrete floor outside the square of iron blocks (1.4 m x 1.4 m). Thus another 3 % was contributed from the photons that penetrated the iron blocks and then backscattered from concrete to air. Under this layout arrangement, the direction of source photons is restricted in the solid angle which defined the backscattered photon source; 99 % from added iron square area onto concrete floor and 1 % from concrete outside of the iron blocks square area ('Path 3' in Figure 64).

Figure 65 shows the comparison of energy width for ~200 keV photon field by backscatter layout and filtered X-rays. In comparison with filtered field with proposed setup by National Institute of Standard and Technology (NIST) or Japanese Atomic Energy Institute (JAERI), the backscatter field can provide narrower energy photons.

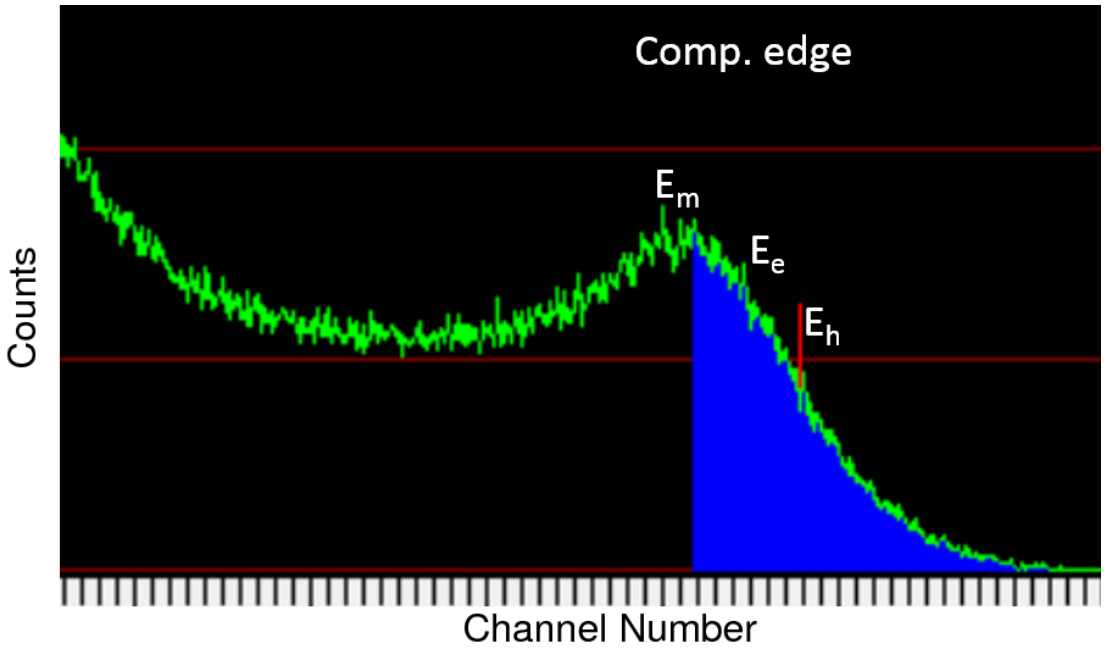

Figure 21 The typical measured spectra with plastic scintillators showing a broad Compton edge. Several points considering the positions of Compton edge include: $E_m$is Compton maxima, E_e is the real Compton edge position (from γ–γ coincidence), and E_h is half of the Compton maxima.

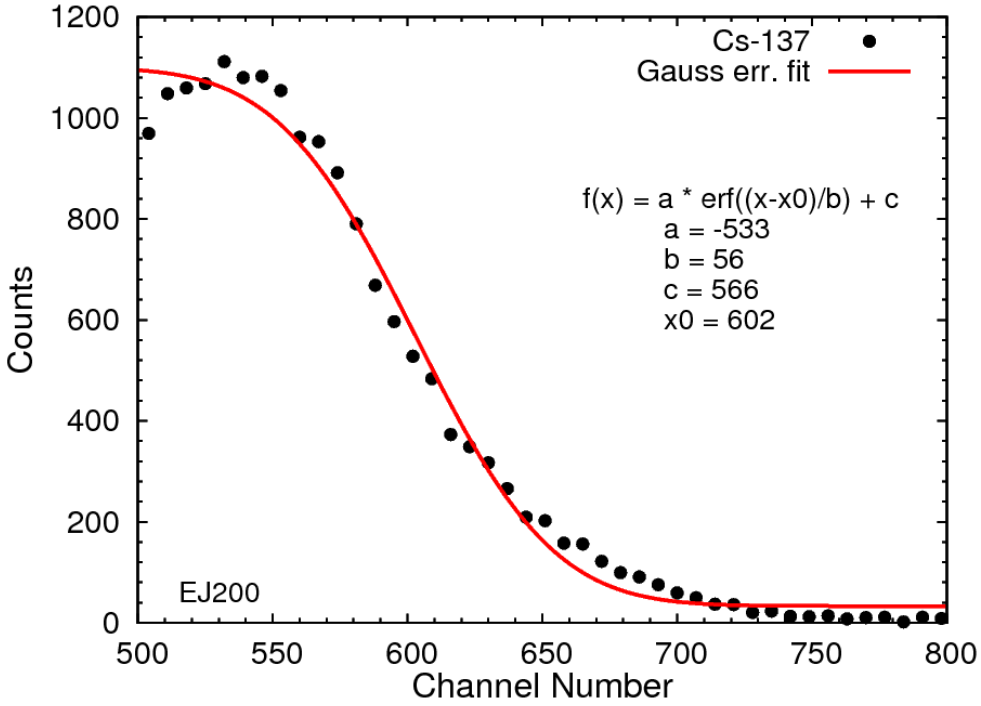

(a)

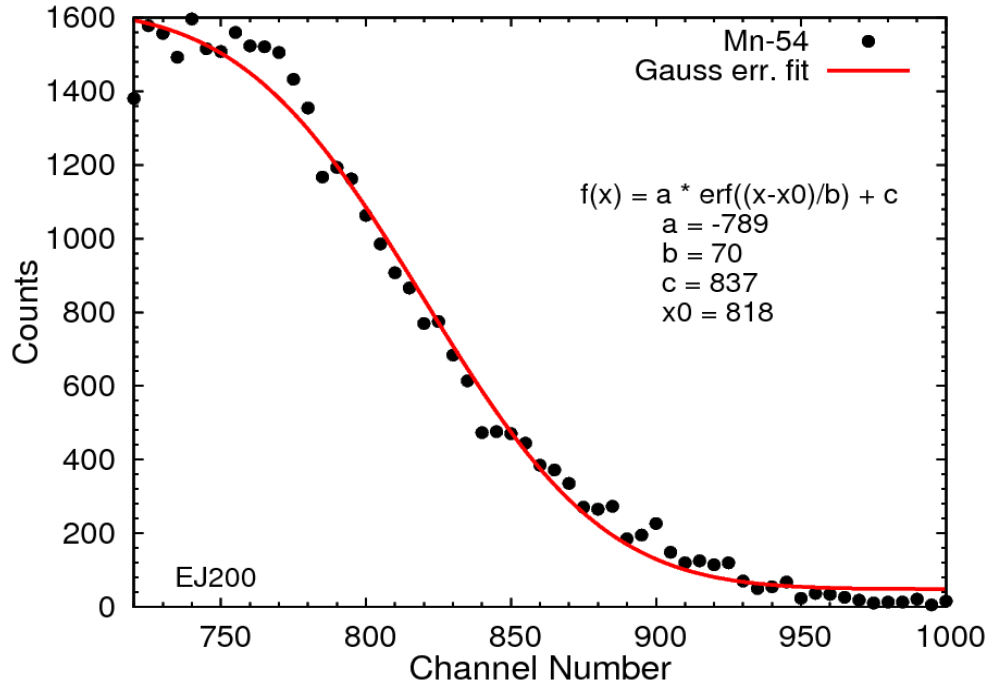

(b)

Figure 22 Example of the shape of the Compton region defined by the Gaussian error function for Cs-137 (a) and Mn-54 (b). Control parameter c is the half counts of the Compton maxima and x0 output is the channel number which corresponds to the location of E_h.

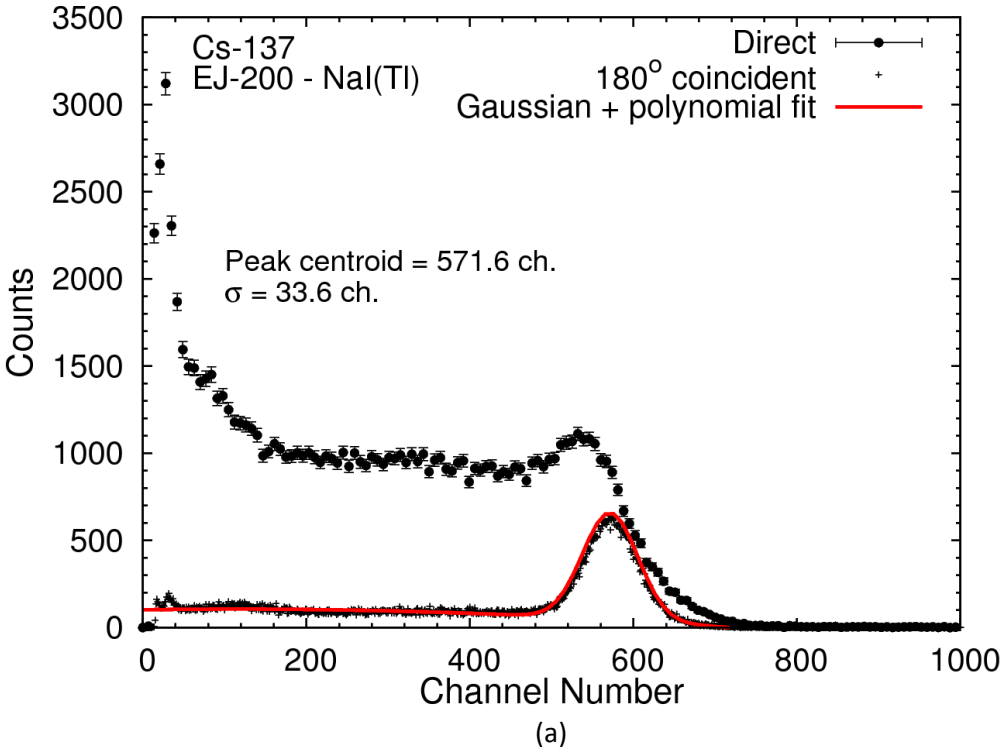

(a)

Figure 23 The direct Compton electron spectrum (o) superimposed on the coincidence spectrum (+) for Cs-137 (a), Mn-54 (b) and Na-22 (c) of EJ-200 (5cm diameter x 5cm long). The red line is the Gaussian fitting on the coincidence spectrum for positions of the Compton edge. (Continue)

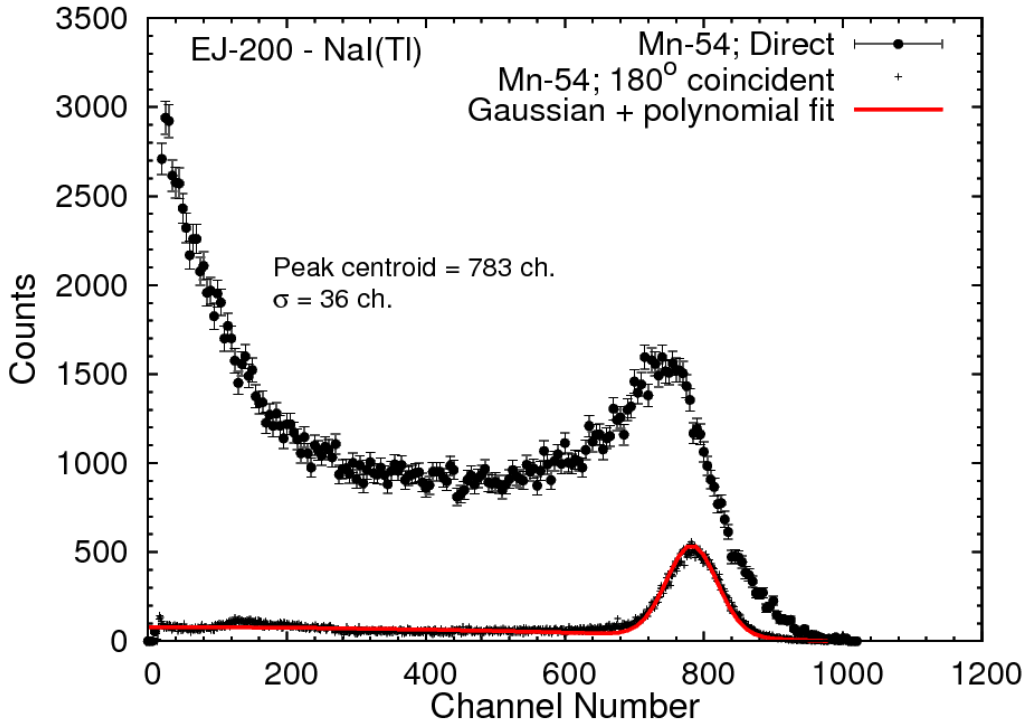

(b)

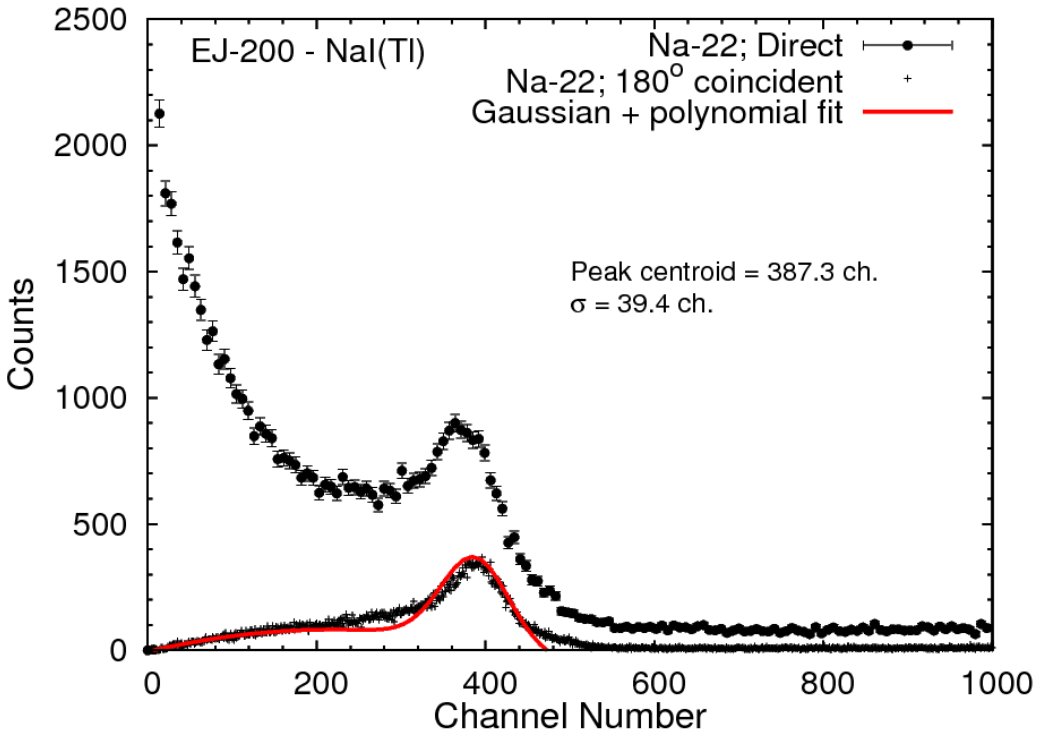

(c)

Figure 23 (cont.) The direct Compton electron spectrum (o) superimposed on the coincidence spectrum (+) for Cs-137 (a), Mn-54 (b) and Na-22 (c) of EJ-200 (5cm diameter x 5cm long). The red line is the Gaussian fitting on the coincidence spectrum for positions of the Compton edge.

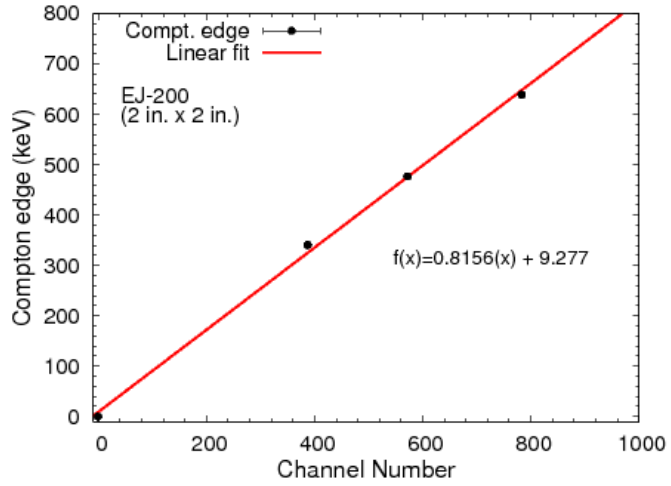

(a)

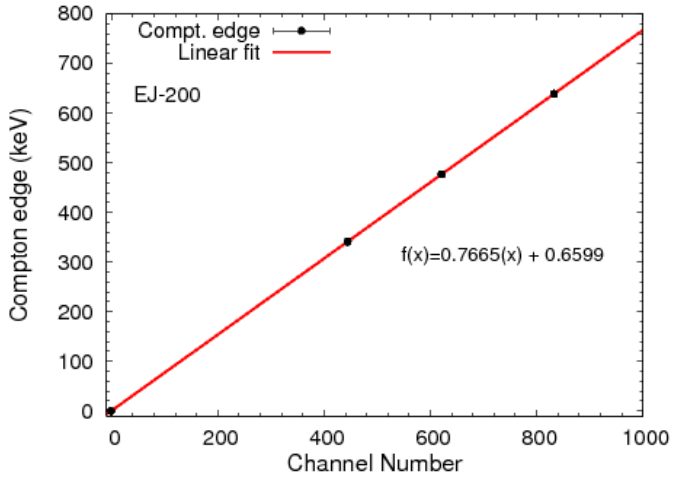

(b)

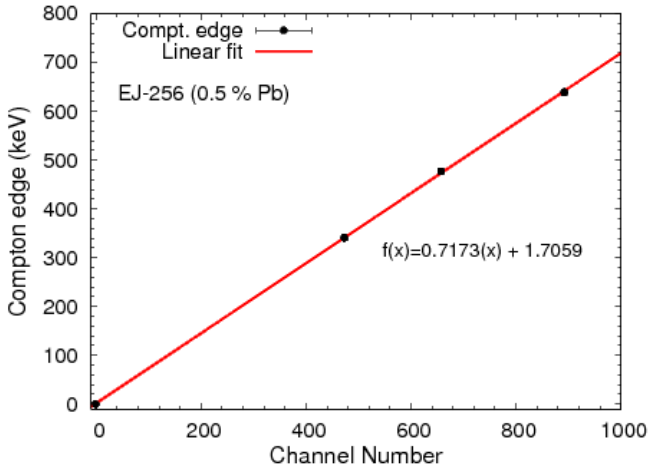

(c)

Figure 24 Linear fit of the Compton edge energy and its pulse height from Cs-137, Mn-54 and Na-22 gamma ray sources. (a) EJ-200 for 5 cm long, (b) EJ-200 for 1 cm long and (c) EJ-256 (0.5 % Pb) for 1 cm long. Error bars shows the error of the peak position.

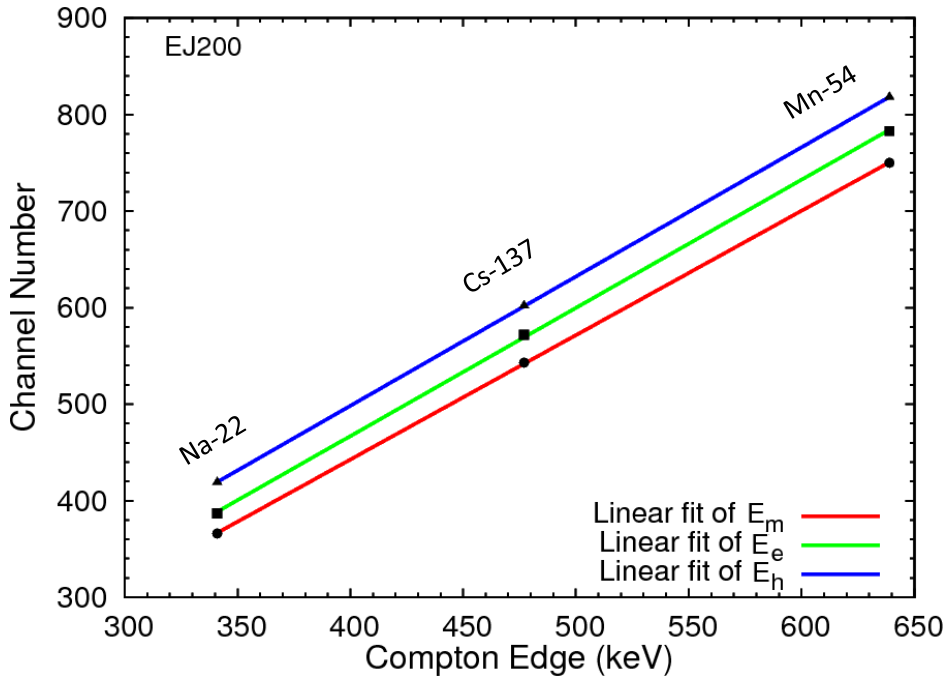

Figure 25 Linear fit of the Compton edge positions and pulse height values from Cs-137, Mn-54 and Na-22 gamma ray sources. The data of EJ-200 for 5 cm diameter x 5 cm long.

Table 5 The deviation of the Compton edge position of Compton maximum (E_m) with the true position of Compton edge (E_e) for EJ-200 (5 cm diameter x 5 cm long).

Sources	C_{edge}	Channel position		$(E_m - E_e)/E_e$
	(keV)	E_m	E_e	(%)
Na-22	341	366	387	-5.43
Cs-137	477	543	572	-5.07 (-5.5*)
Mn-54	639	750	783	-4.21

* Literature data for BC-408 of 4 cm diameter x 5cm long [43].

Table 6 The deviation of the Compton edge position of half-height of Compton maximum (E_h) from the true position of Compton edge (E_e) for EJ-200 (5 cm diameter x 5 cm long).

Sources	C_{edge}	Channel position		$(E_h - E_e)/E_e$
	(keV)	E_h	E_e	(%)
Na-22	341	419	387	8.27 (9.8**)
Cs-137	477	602	572	5.24 (6.7**)
Mn-54	639	818	783	4.47 (5.4**)

**Literature data for NE-213 of 5 cm diameter x 5 cm long [42].

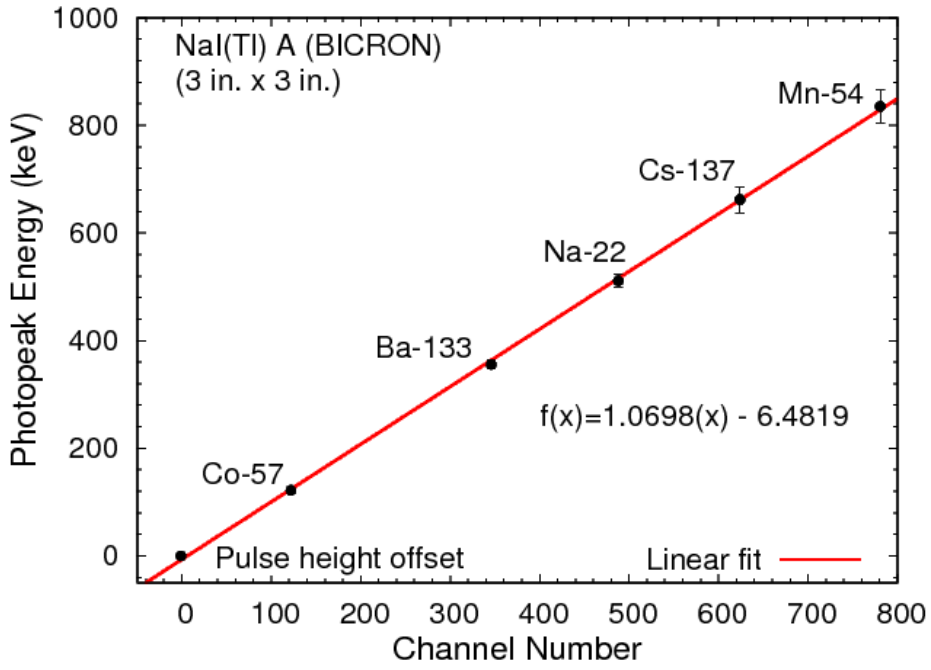

(a)

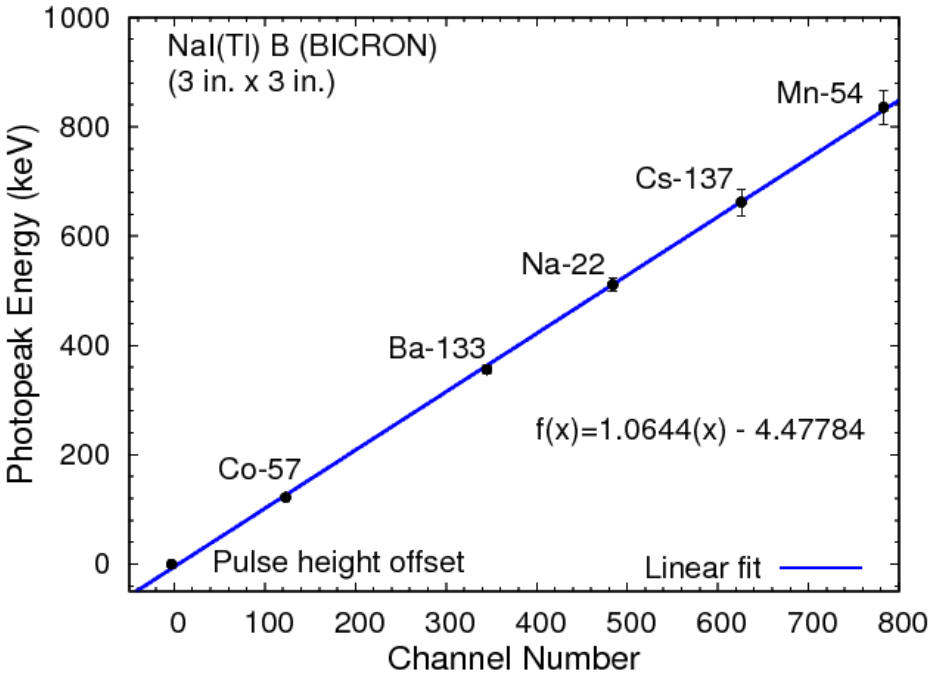

(b)

Figure 26 The energy calibration curves of both 3”x 3” NaI(Tl) reference detectors. Both detectors were independent of each other for coincidence measurements. The error bar shows the error of peak position.

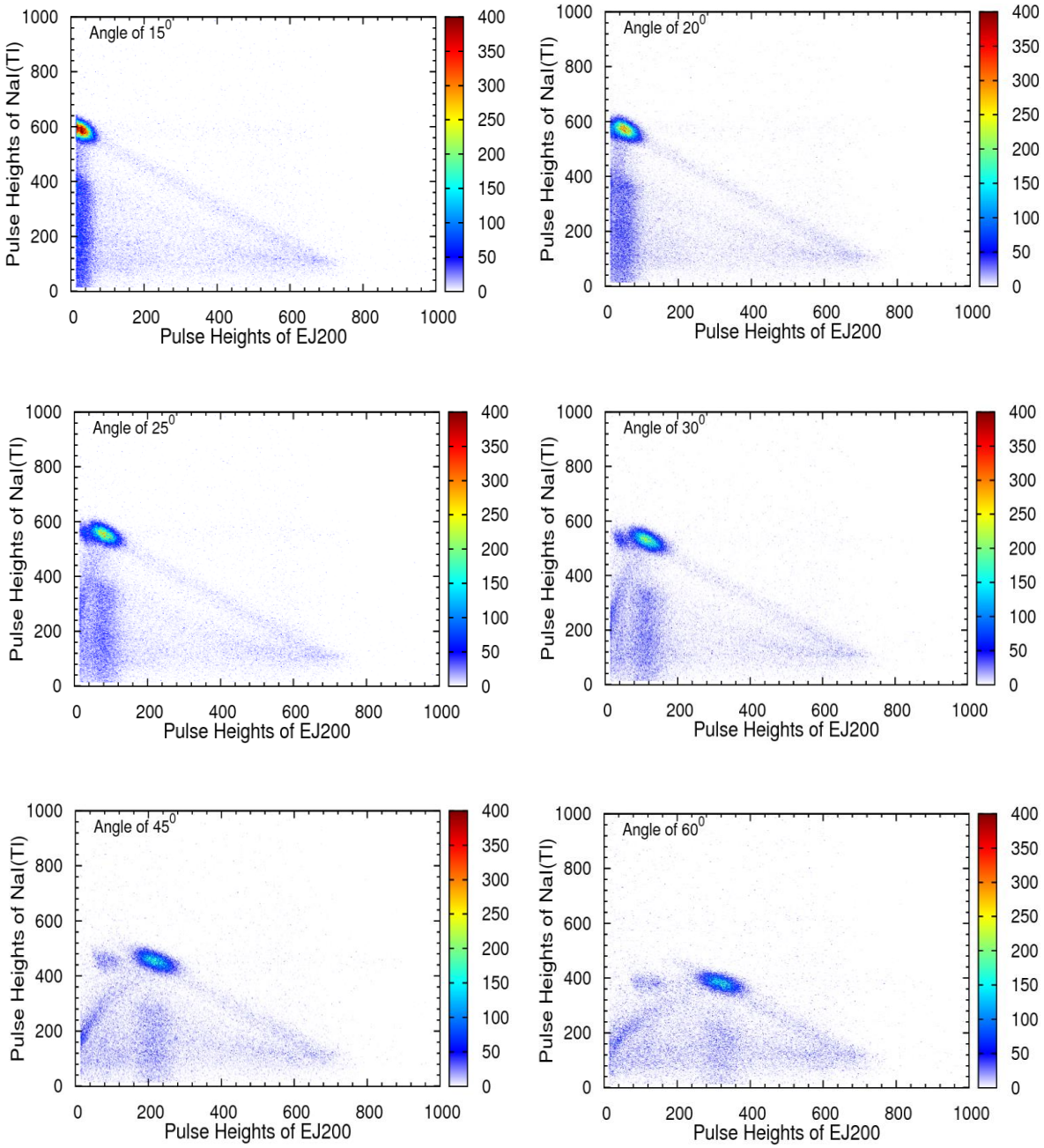

Figure 27 The 2D coincidence plots of the 2”x 2” EJ-200 and 3”x 3” NaI(Tl) measured by Compton coincidence technique. The coincidence events were obtained through the time window of events that had arrival times within 50 ns of one another. The circle structures represent the energies of 662 keV deposited partly in the target and reference detectors in coincidence.

(Continue)

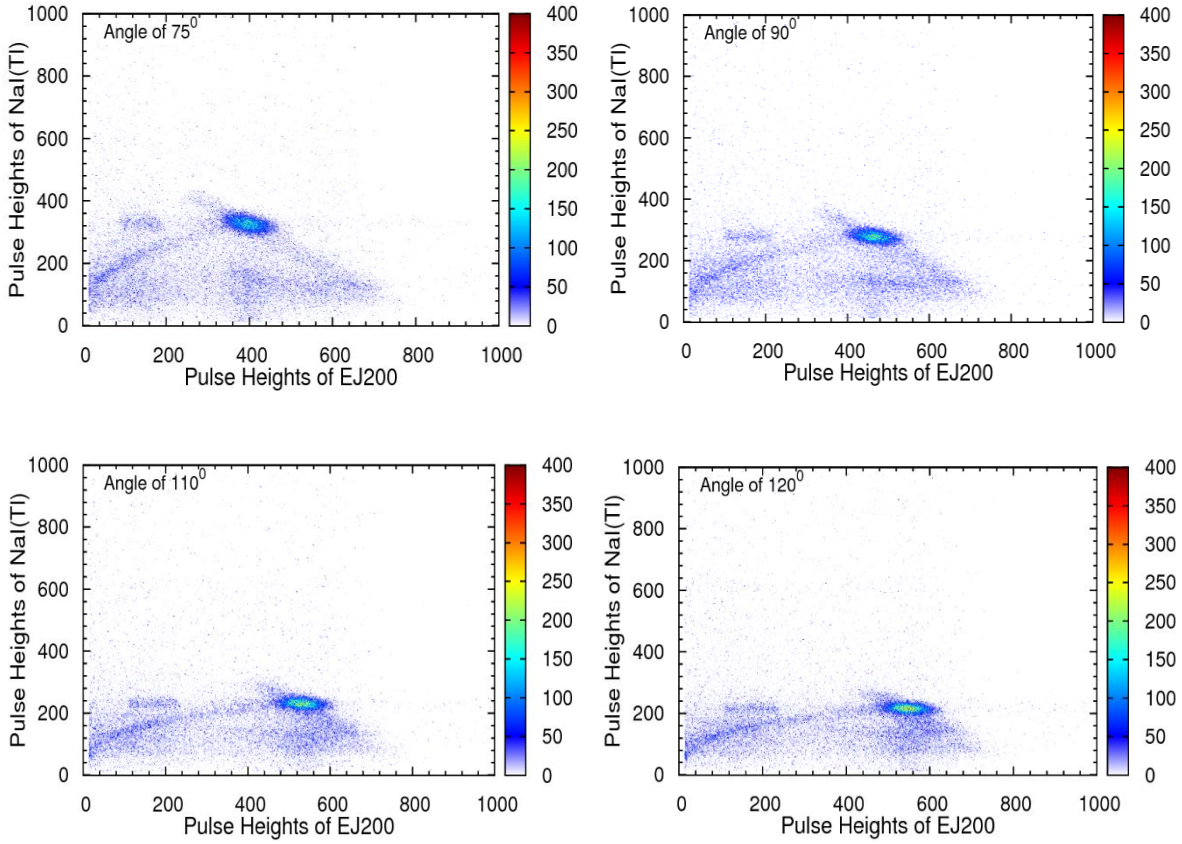

Figure 27 (Cont.) The 2D coincidence plots of the 2”x2” EJ-200 and 3”x3” NaI(Tl) measured by Compton coincidence technique. The coincidence events were obtained through the time window of events that had arrival times within 50 ns of one another. The circle structures represent the energies of 662 keV deposited partly in the target and reference detectors in coincidence.

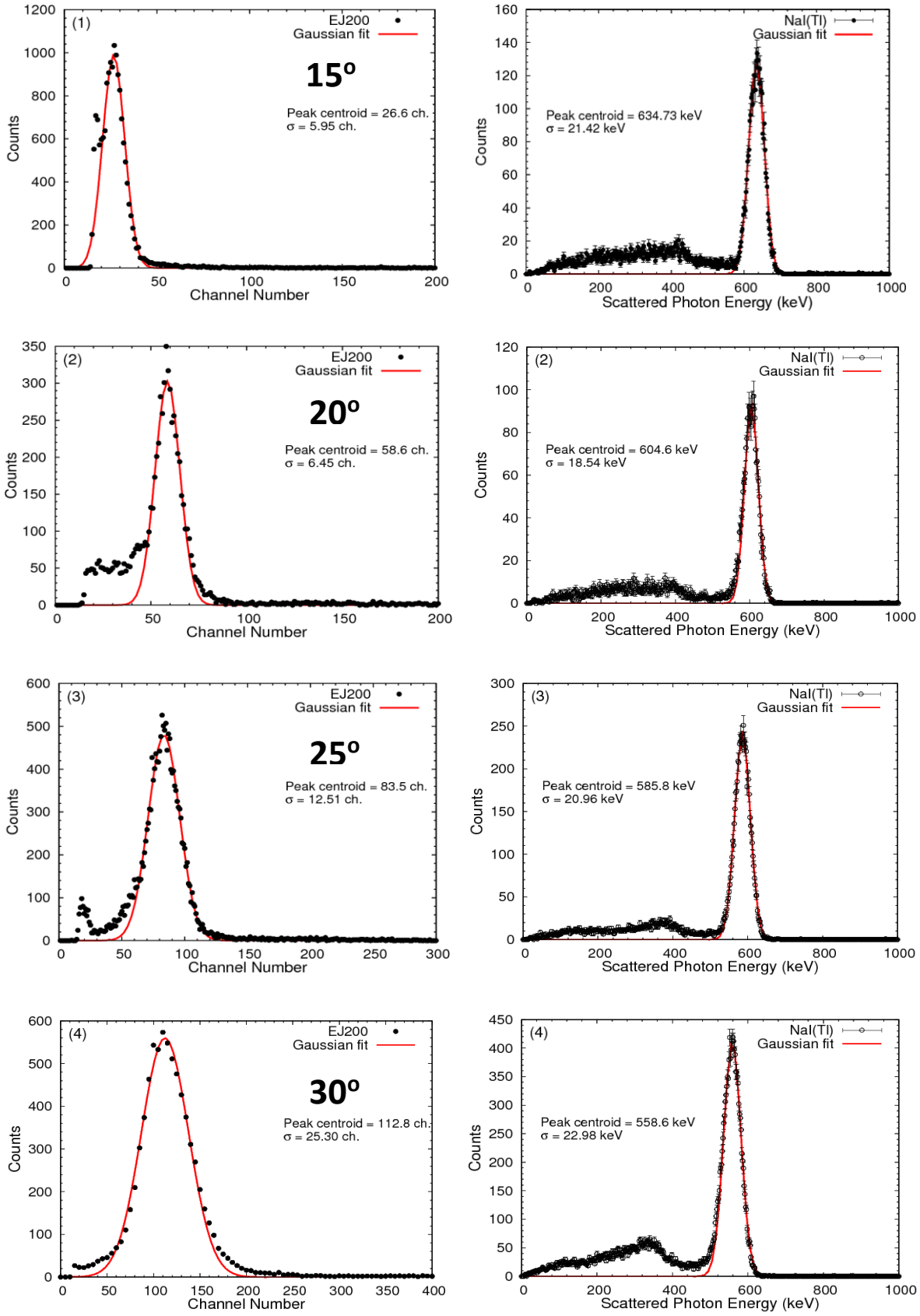

Figure 28 The coincidence energy spectrum of the 2"x 2" EJ-200 and 3"x 3" NaI(Tl) that correspond to Fig. 17 as measured by the Compton coincidence technique. The coincidence electron energy spectrum obtained was a Gaussian peak. (Continue)

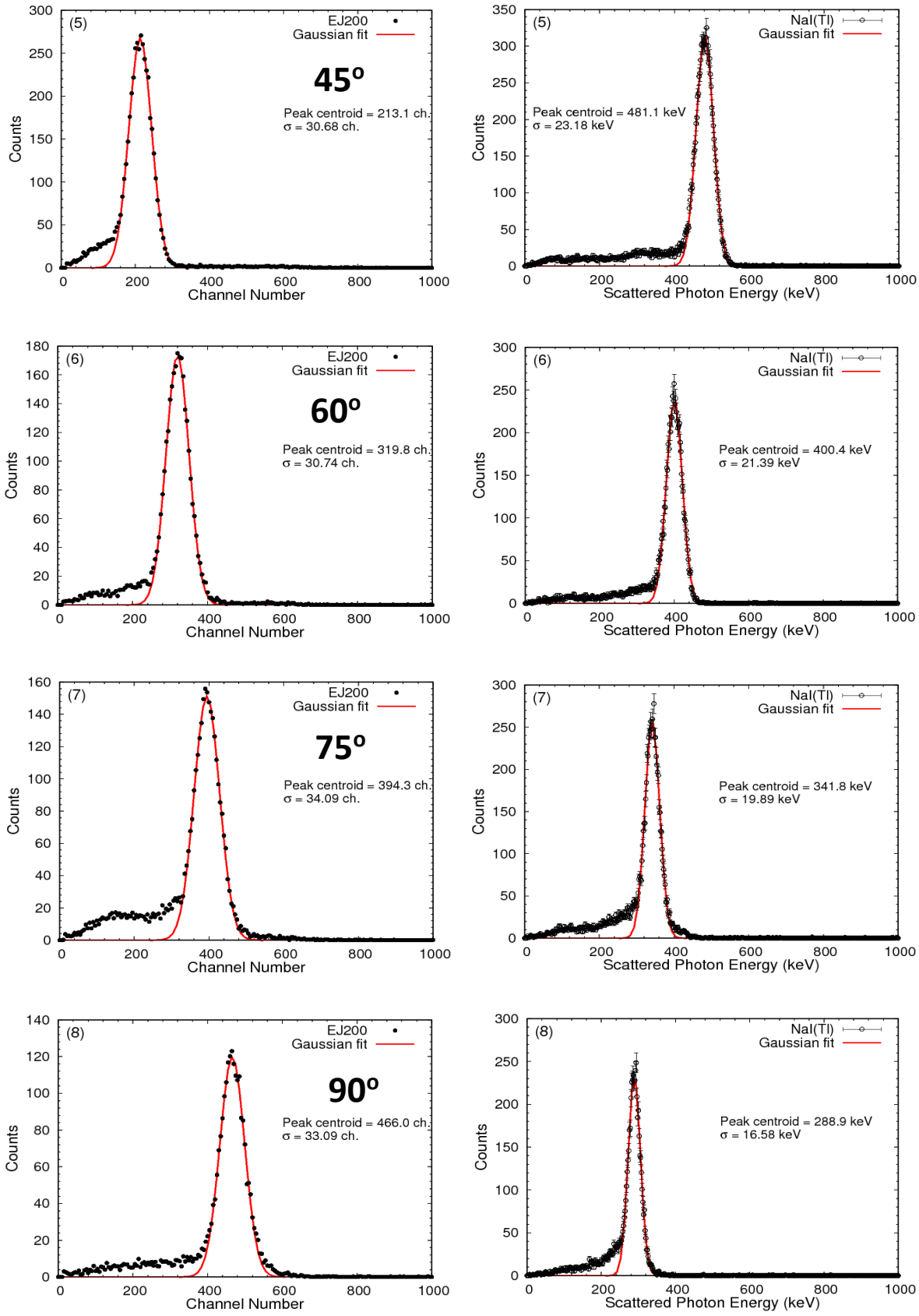

Figure 28 (Cont.) The coincidence energy spectrum of the 2"x 2" EJ-200 and 3"x 3" NaI(Tl) that correspond to Fig. 17 as measured by the Compton coincidence technique. The coincidence electron energy spectrum obtained was a Gaussian peak. (Continue)

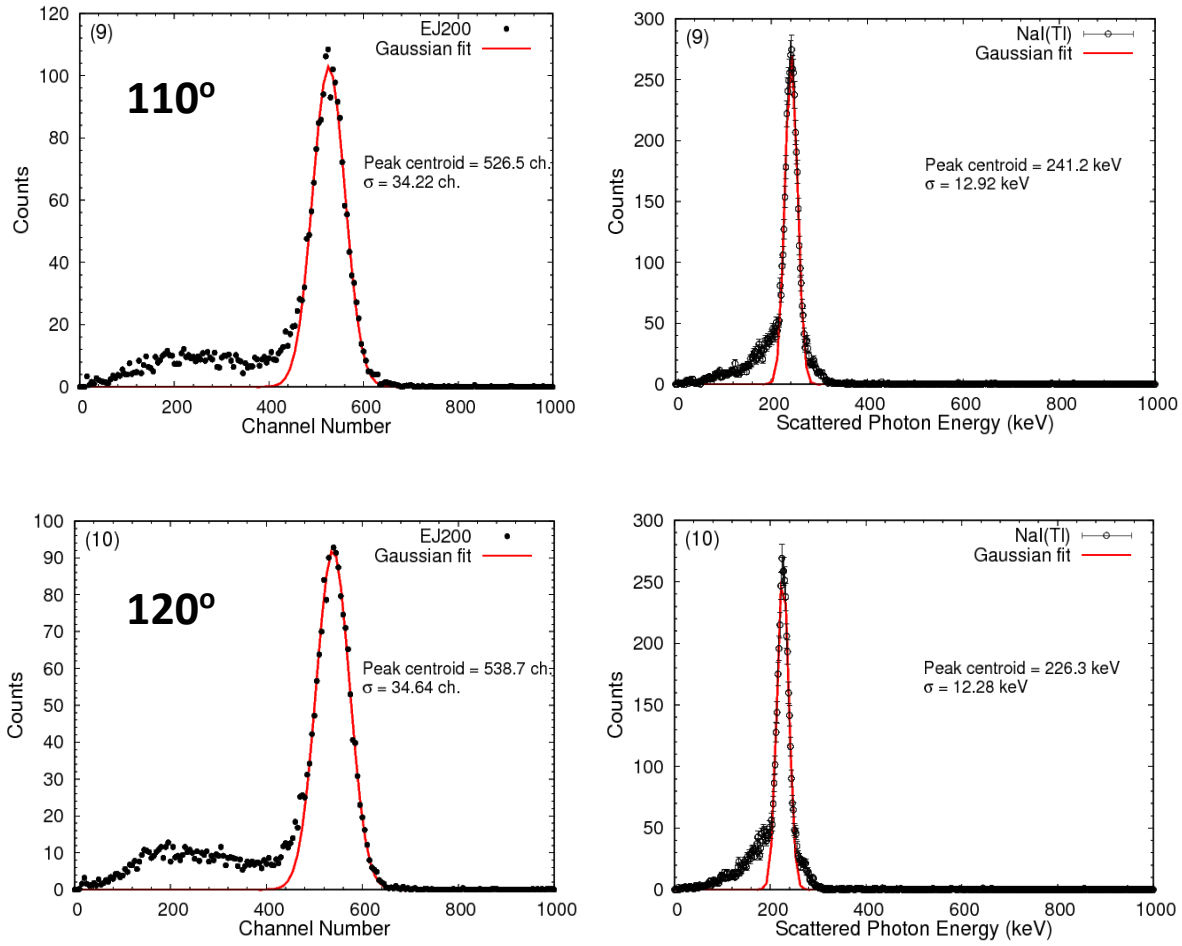

Figure 28 (Cont.) The coincidence energy spectrum of the 2"x 2" EJ-200 and 3"x 3" NaI(Tl) that correspond to Fig. 17 as measured by the Compton coincidence technique. The coincidence electron energy spectrum obtained was a Gaussian peak.

Table 7 The values of time window (ns) applied as a function of scattering angle. The short coincidence time gives an advantage to significantly reduce chance coincidence events.

Angle (θ)	15	20	25	30	45	60	75	90	110	120
Time window (ns)	50	25	50	75	75	50	25	50	50	50

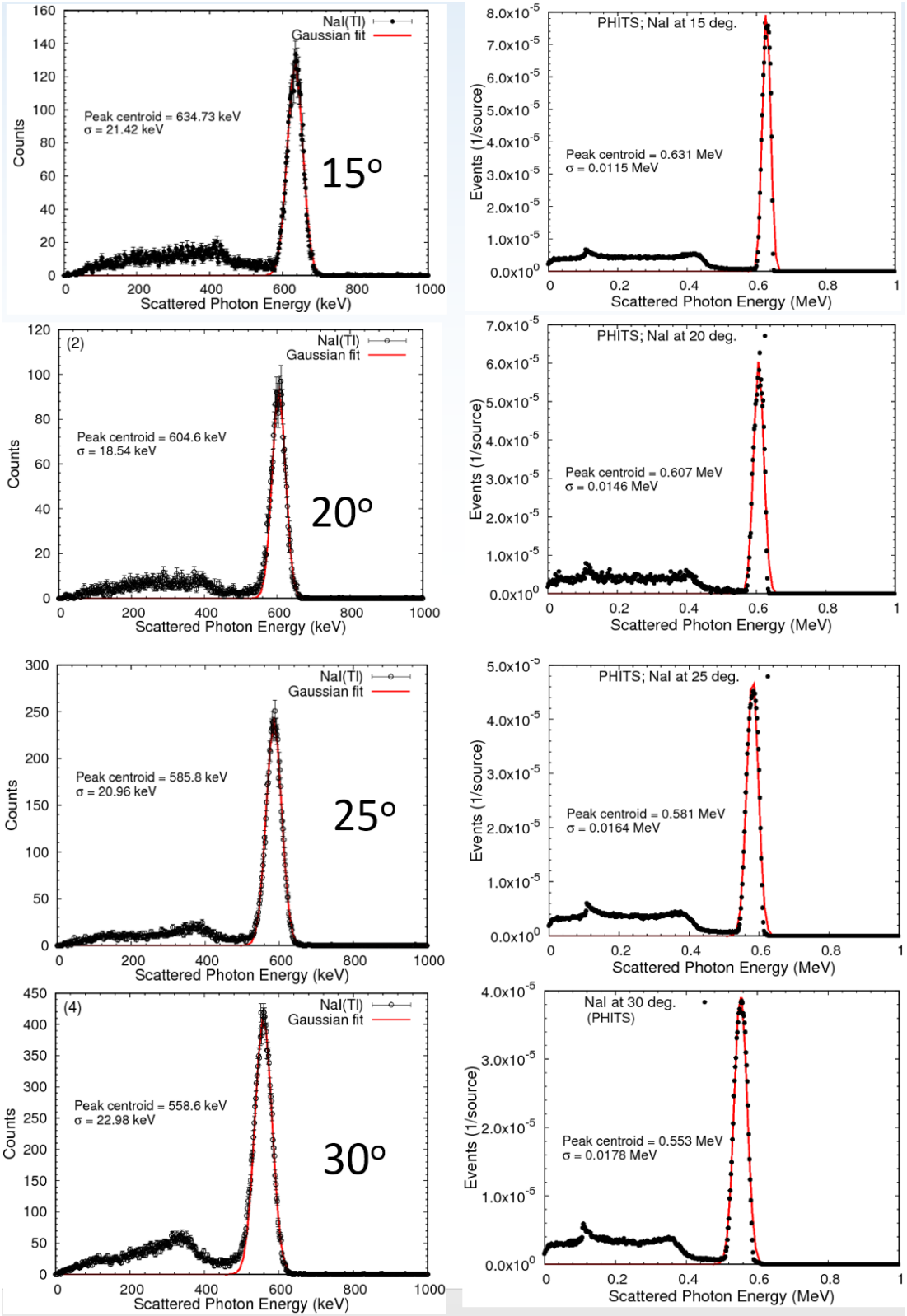

Figure 29 The measured (E_γ) and calculated (E_γ') (PHITS code) for Compton scattered photon energy as a function of scattering angle. The distance between the EJ-200 to the NaI(Tl) was fixed at 40 cm. (Continue)

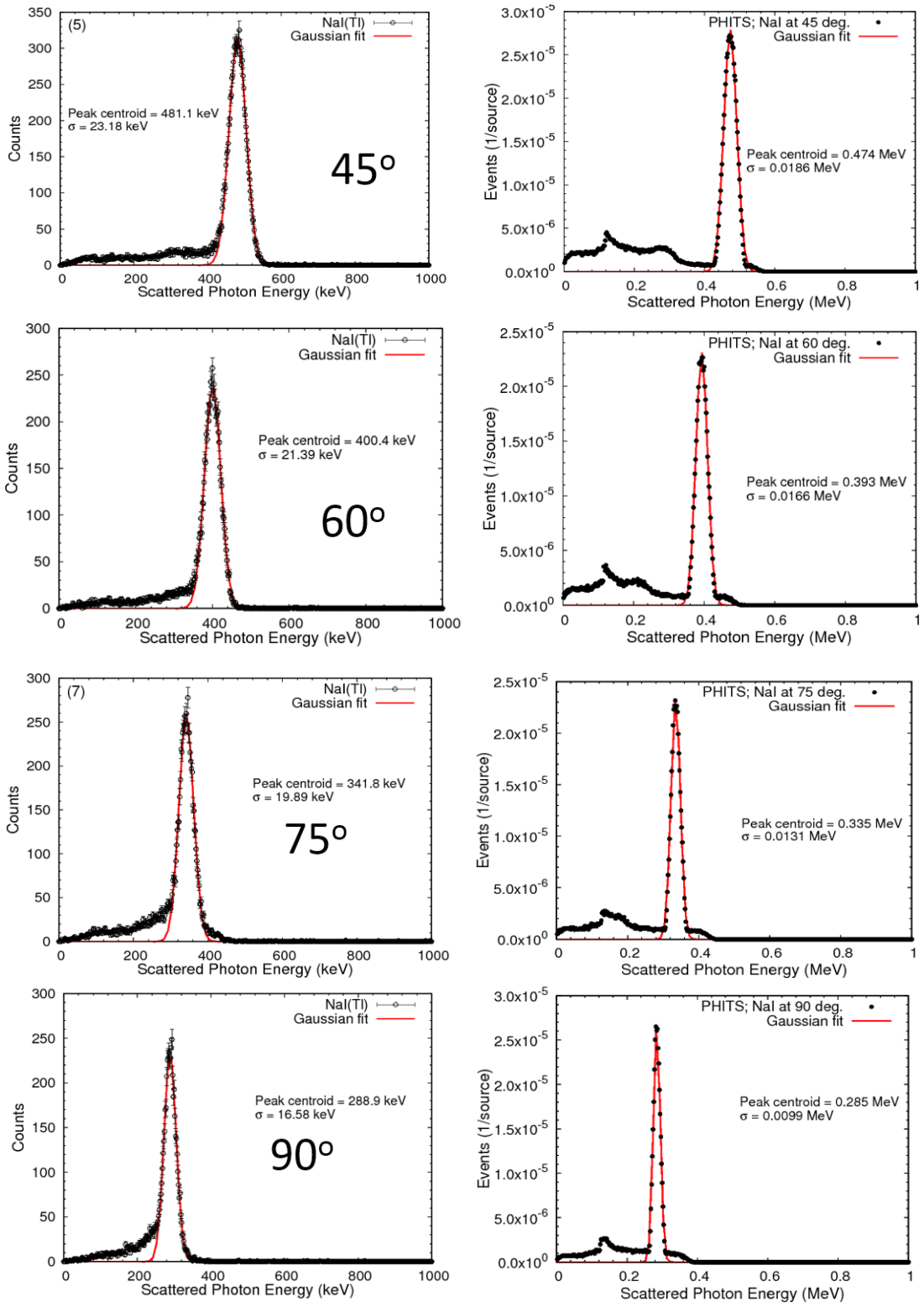

Figure 29 (Cont.) The measured (E_γ) and calculated (E_γ') (PHITS code) for Compton scattered photon energy as a function of scattering angle. The distance between the EJ-200 to the NaI(Tl) was fixed at 40 cm.

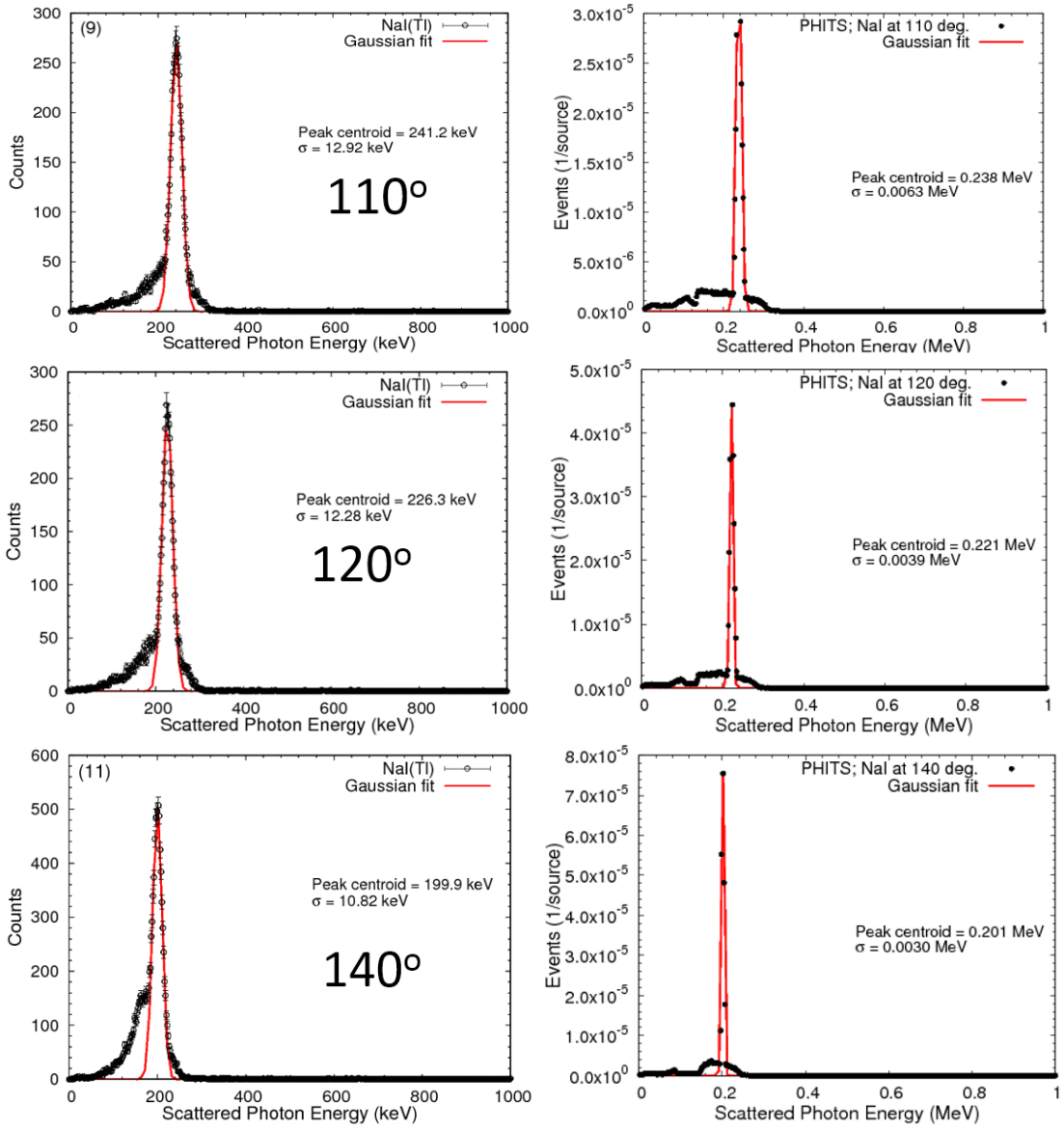

Figure 29 (Cont.) The measured (E_γ) and calculated (E_γ') (PHITS code) for Compton scattered photon energy as a function of scattering angle. The distance between the EJ-200 to the NaI(Tl) was fixed at 40 cm.

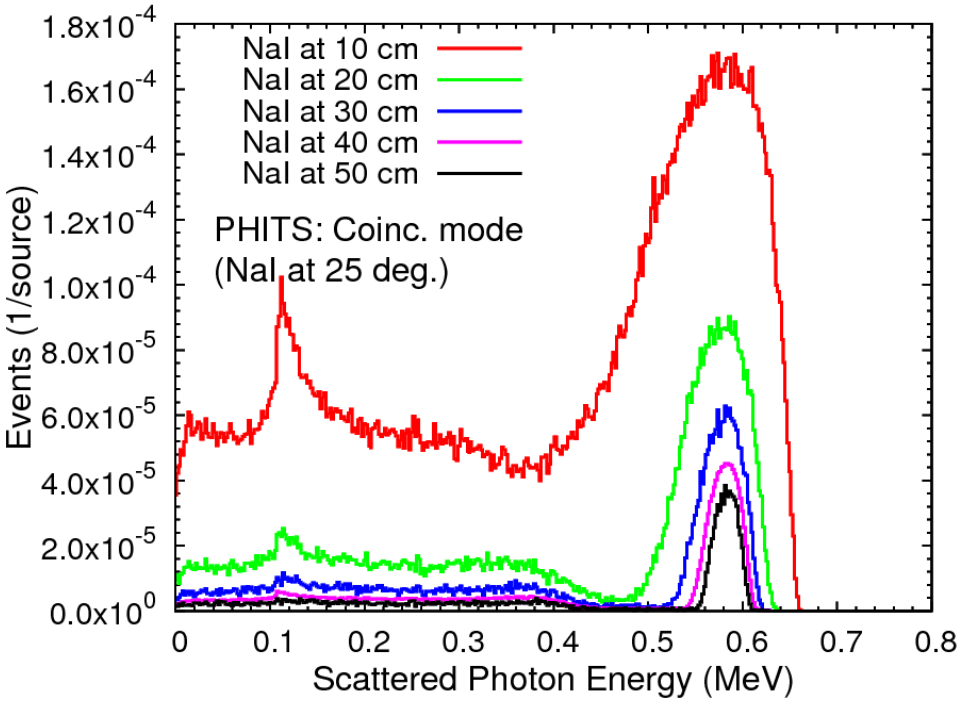

Figure 30 The inherent width of scattered photon spectra by NaI of 3 in x 3 in. The spectra was calculated at one angle of 25 degree for several distance. The narrower and Gaussian shape peak was obtained when the distance is above 30 cm distance.

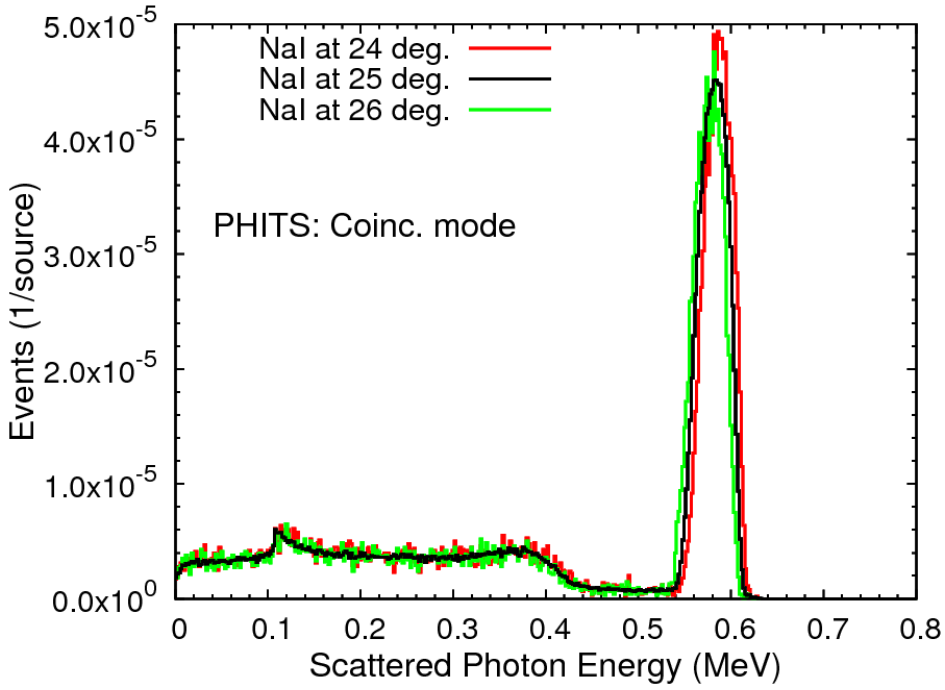

Figure 31 The calculated scattered photon spectra for angle uncertainty of 1 degree at a distance of 40 cm from target scintillator. The peak centroid was deduced from the Guassion fit. The difference of peak centoid to 25 degree is within 0.86 %.

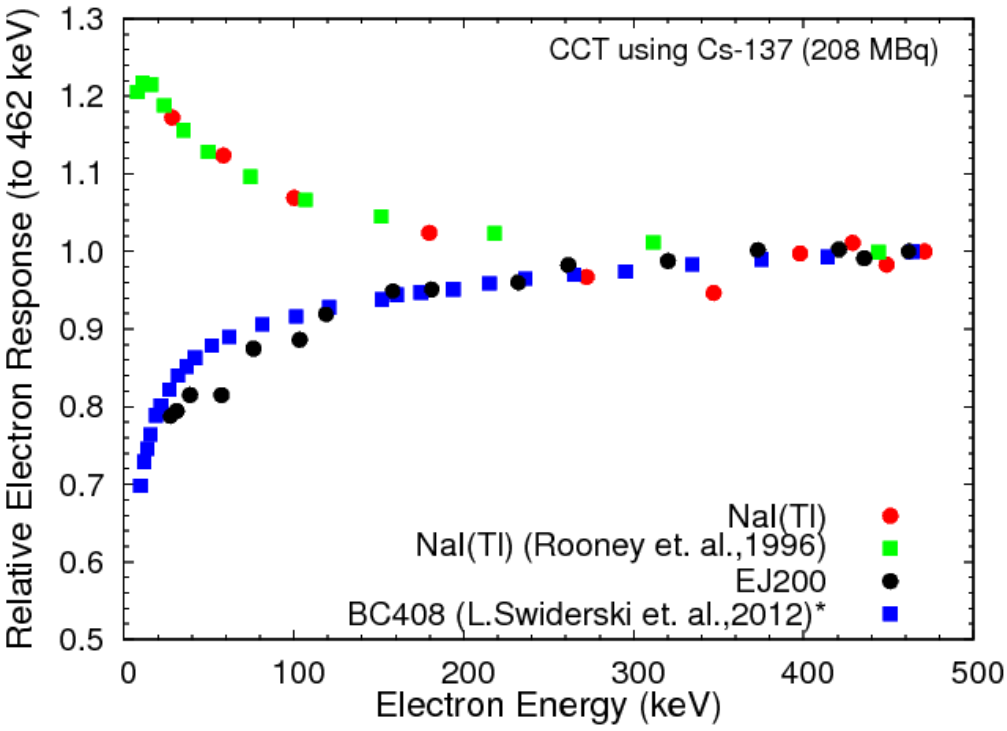

Figure 32 Relative electron response of EJ-200 (black dotted) and NaI(Tl) (red dotted) measured with CCT. The blue square is the literature data [46] measured from wide angle Compton coincidence. Disagreement was significant at around 60 keV. The electron response of NaI(Tl) was compared to the green square [24]. Disagreement of measurement could be seen around 350 keV as discussed in main text.

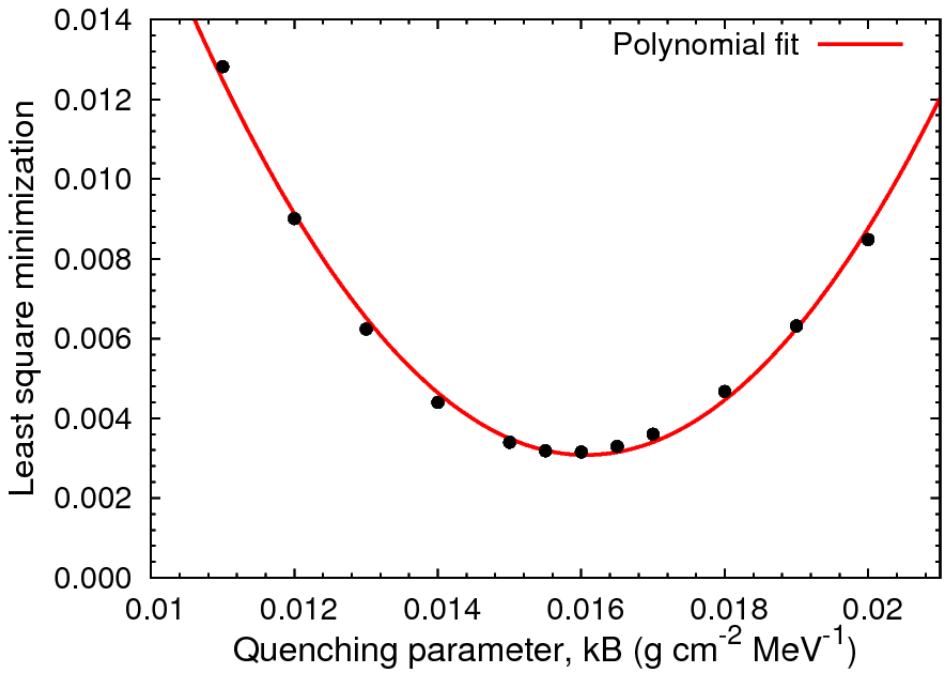

Figure 33 Result of least square analysis comparing the Birks calculated light output from Equation 2 to the experimental data light output for EJ-200. Several quenching parameters (*kB*) were considered. Best-fitted value is *kB*=0.016.

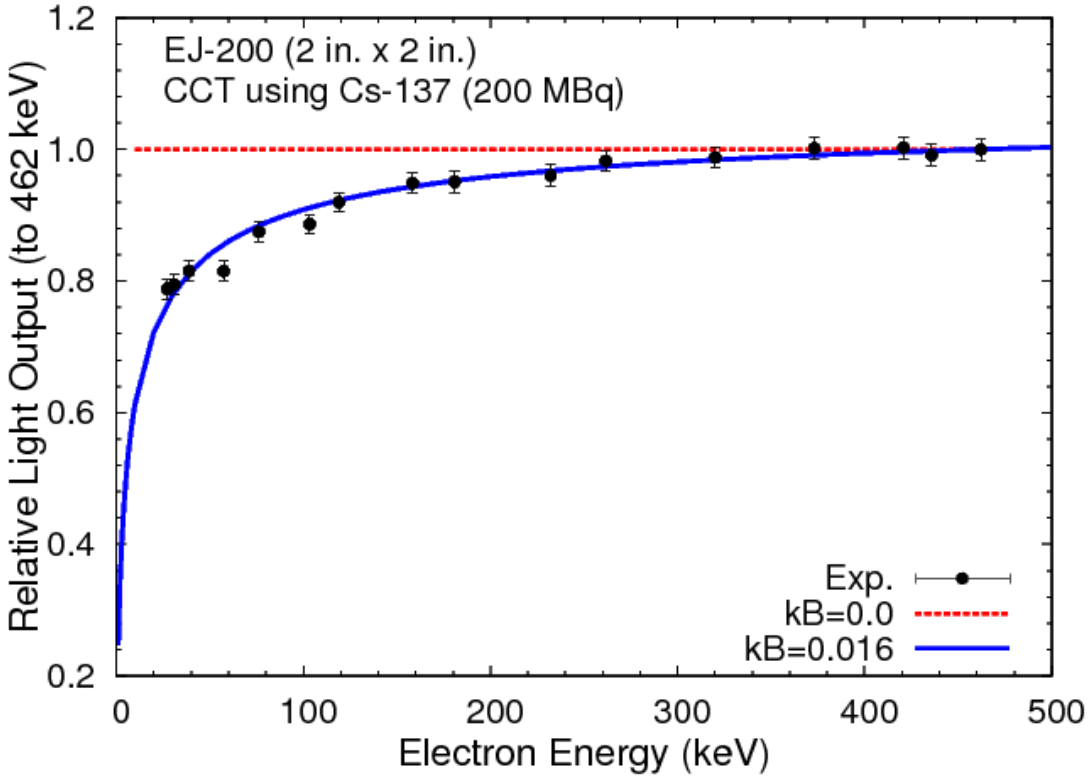

Figure 34 Relative electron response of the EJ-200 plastic scintillator (black dotted) measured with CCT. The red and blue lines are the calculated light yield from Birks' formula for *kB* of 0.0 and 0.016 g cm^{-2} MeV^{-1}, respectively. The error bars shows the total error of peak position and NaI(Tl) conversion uncertainty from channel to energy.

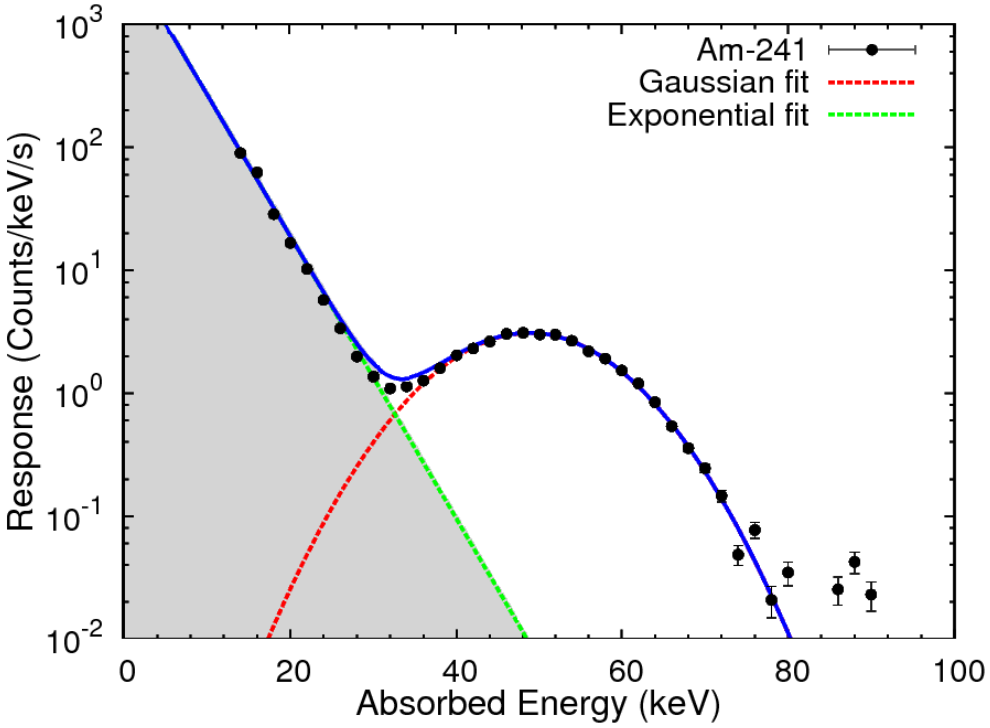

(a)

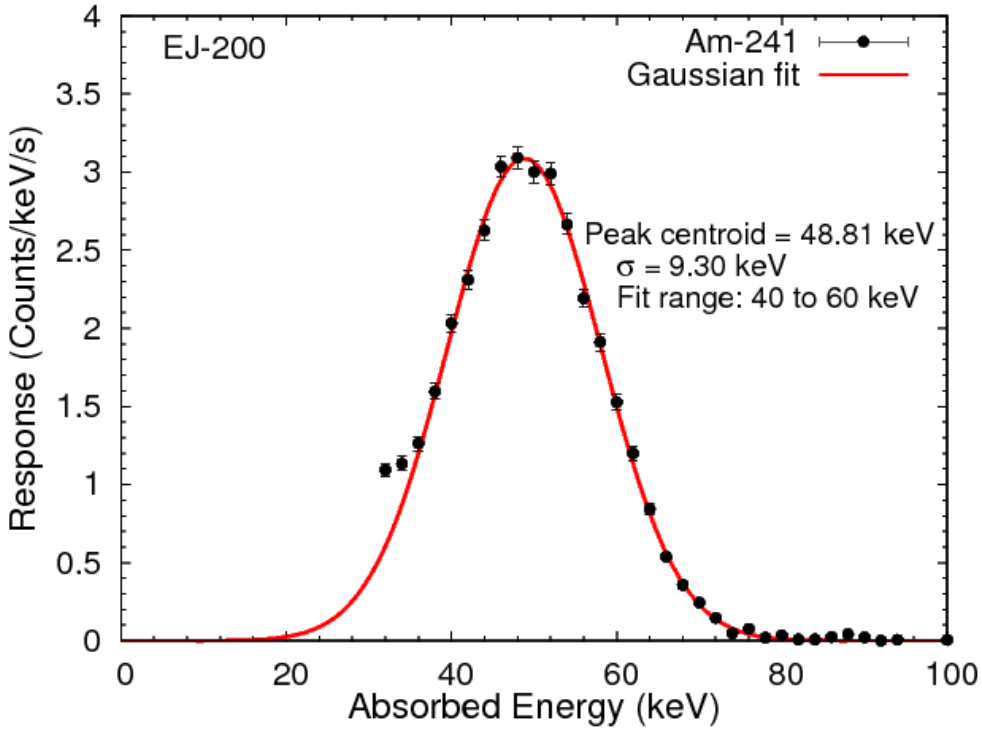

(b)

Figure 35 The 2-step analysis on the photopeak of Am-241 to determine FWHM. (a) The exponential fit was subtracted, and (b) Gaussian fit after subtraction.

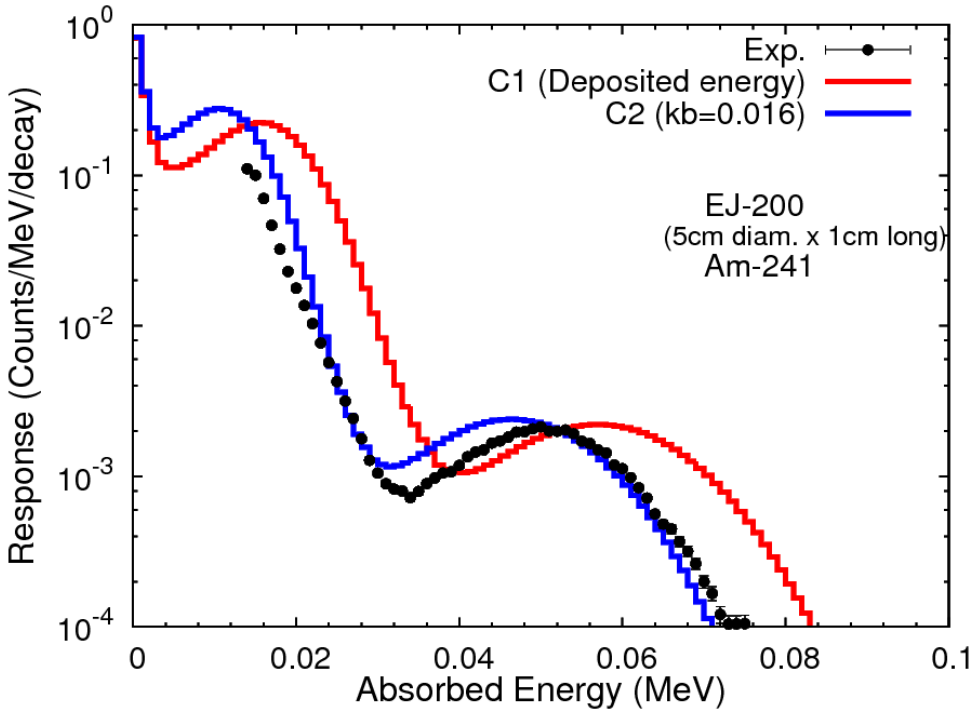

(a)

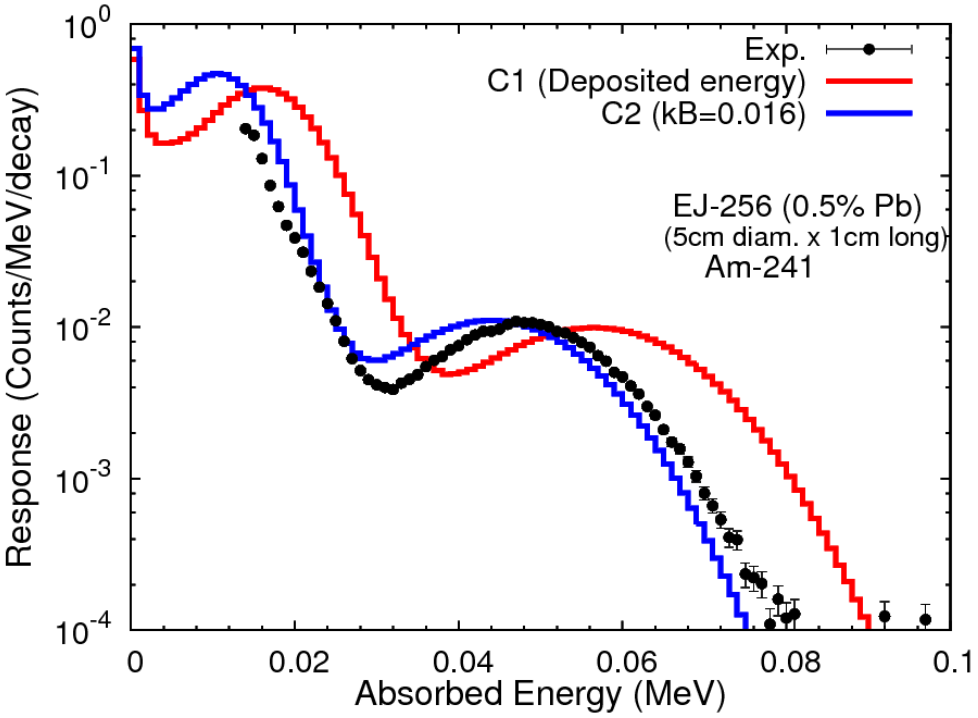

(b)

Figure 36 Measured and calculated light output distribution of Am-241 for a 5 cm diameter x 1 cm long cylinder of EJ-200 (a) and EJ-256 (b) at 10 cm distance. Black points are experimental data, red curve is the calculated energy deposition and blue curve is the calculated spectrum considering quenching effects.

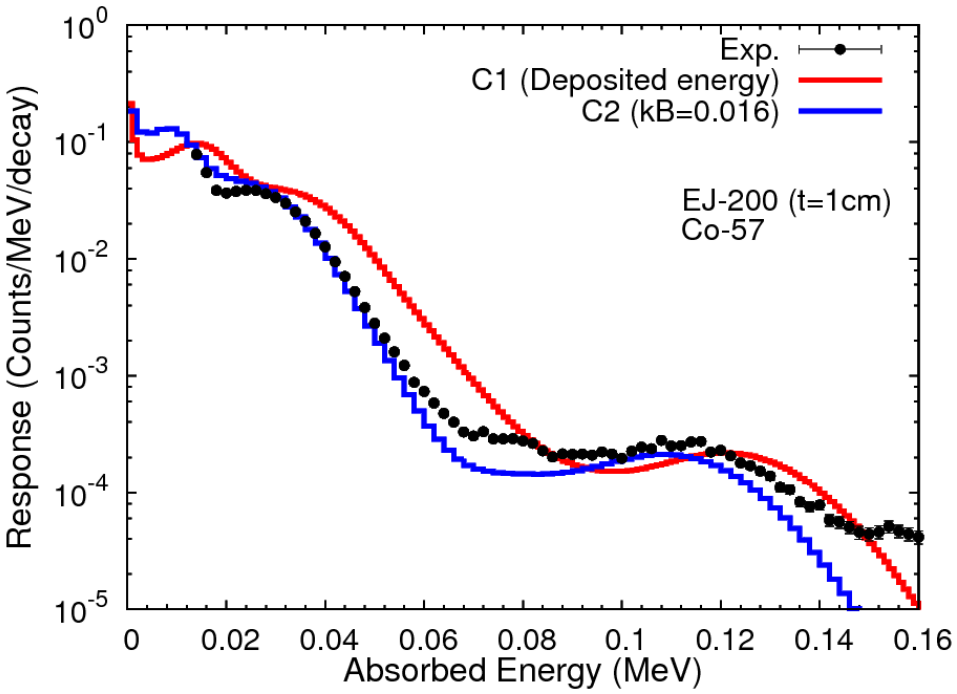

(a)

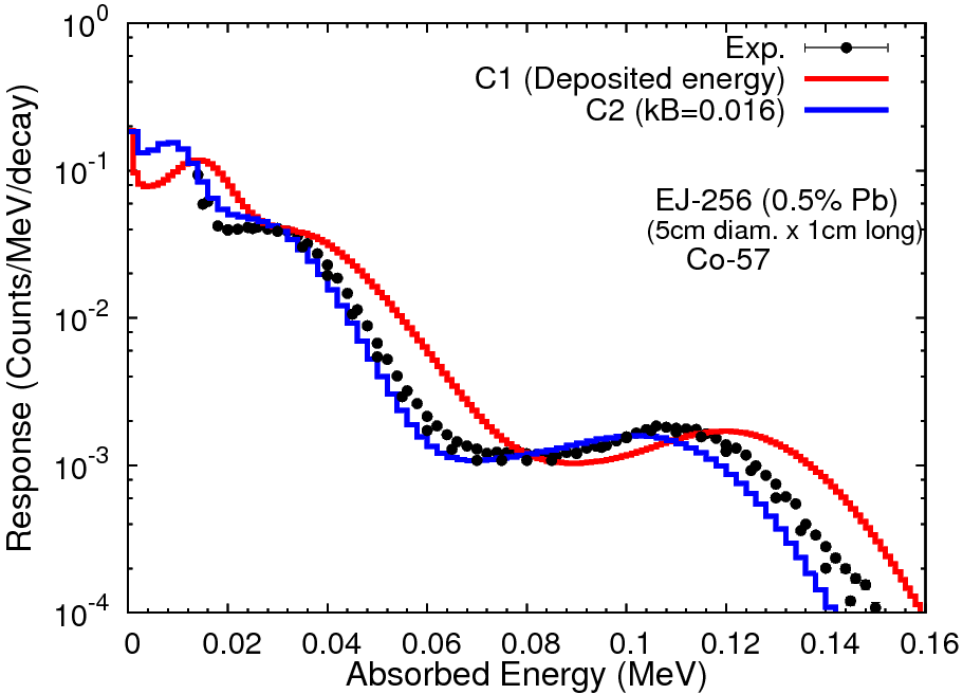

(b)

Figure 37 Measured and calculated light output distribution of Co-57 for a 5 cm diameter x 1 cm long cylinder of EJ-200 (a) and EJ-256 (b) at 10 cm distance. Black points are experimental data, red curve is the calculated energy deposition and blue curve is the calculated spectrum considering quenching effects.

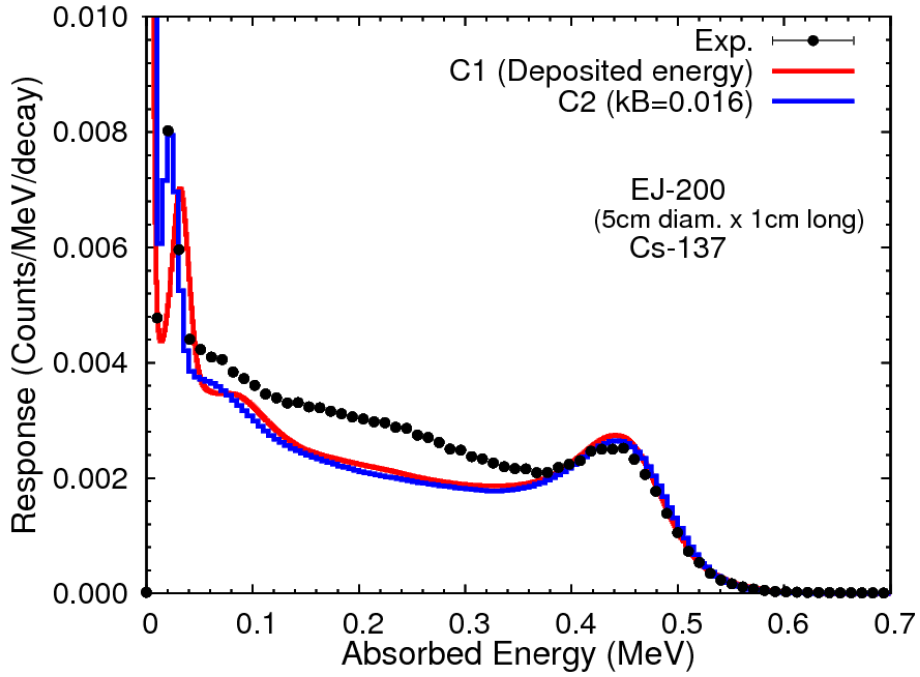

(a)

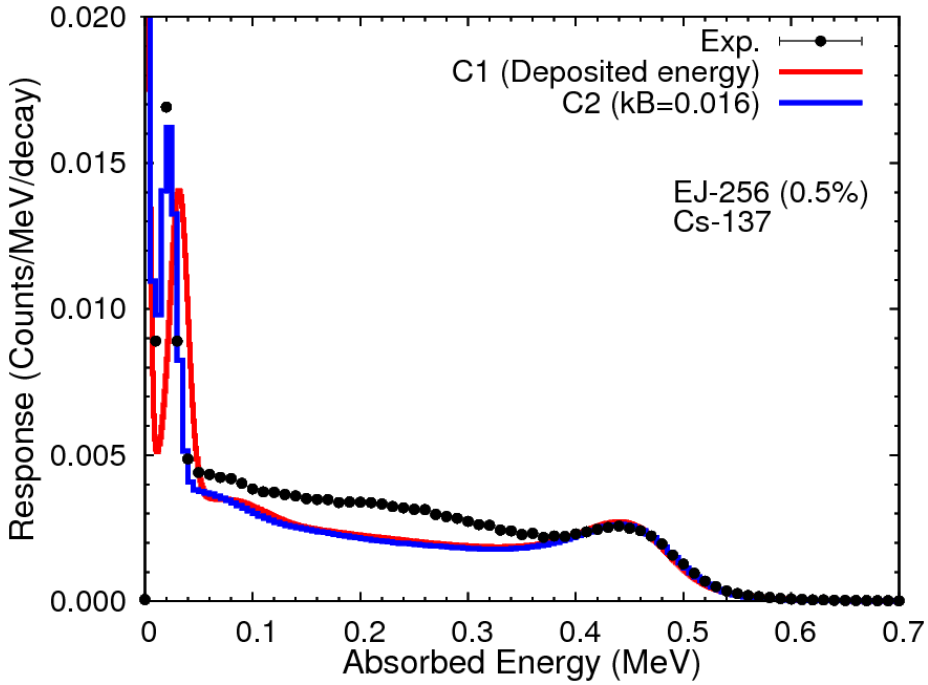

(b)

Figure 38 Measured and calculated light output distribution of Cs-137 for a 5 cm diameter x 1 cm long cylinder of EJ-200 (a) and EJ-256 (b) at 10 cm distance. Black points are experimental data, red curve is the calculated energy deposition and blue curve is the calculated spectrum considering quenching effects.

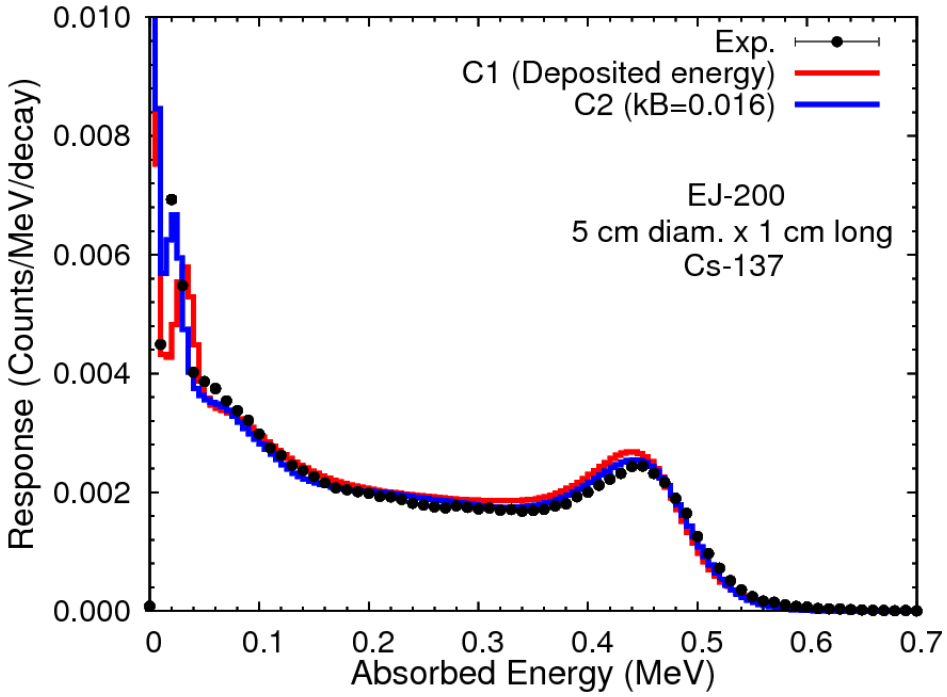

(a)

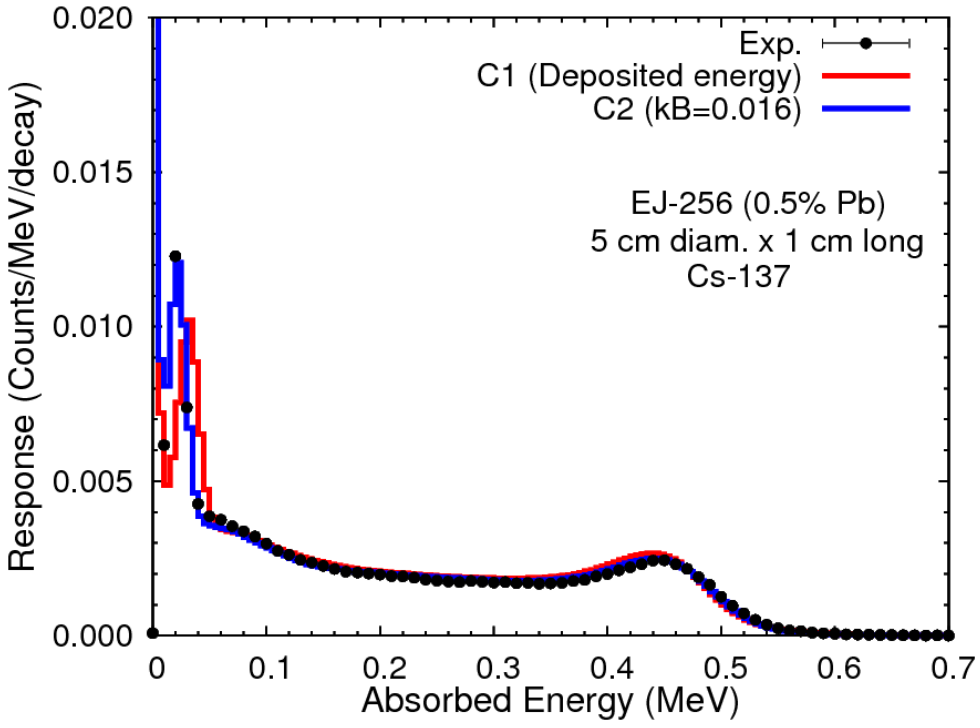

(b)

Figure 39 Measured and calculated light output distribution of Cs-137 for a 5 cm diameter x 1 cm long cylinder of EJ-200 (a) and EJ-256 (b) at 10 cm distance. Black points are experimental data, red curve is the calculated energy deposition and blue curve is the calculated spectrum considering quenching effects. The agreement was improved for the enire spectra once the beta ray emission from the source was blocked by a thin Al (2 mm).

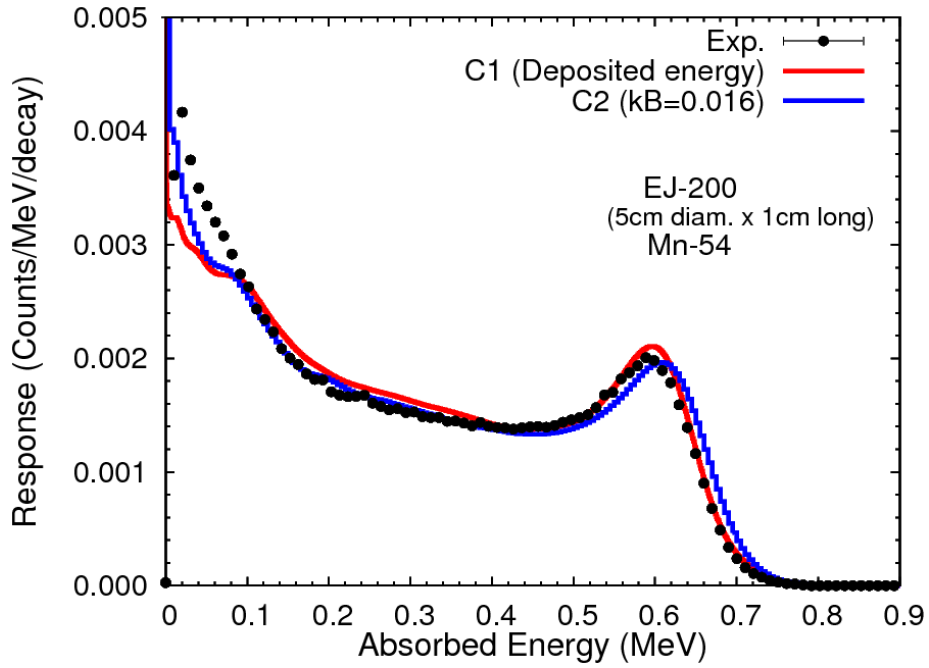

(a)

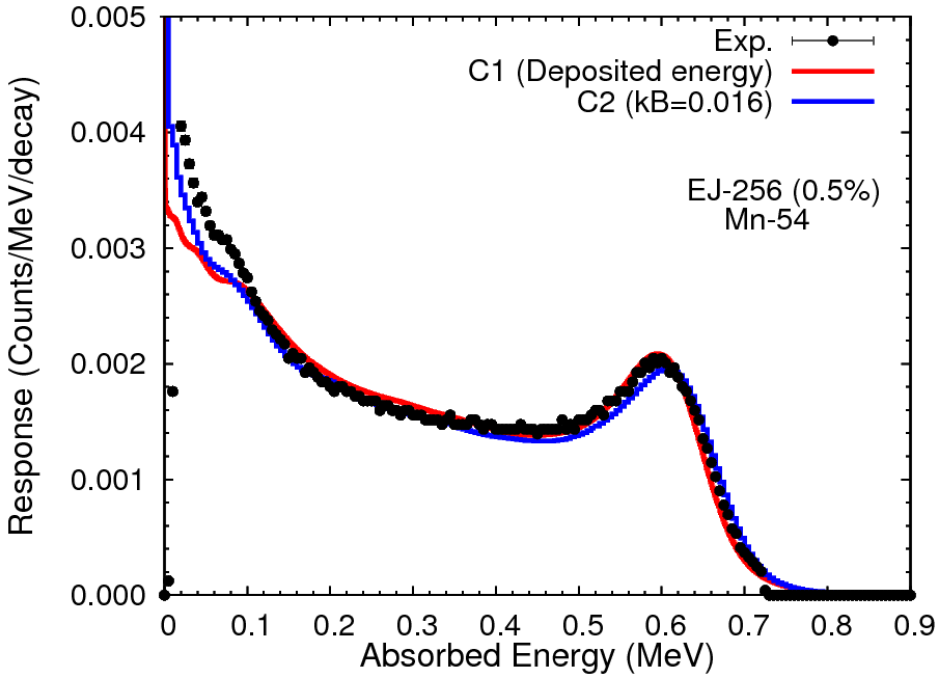

(b)

Figure 40 Measured and calculated light output distribution of Mn-54 for a 5 cm diameter x 1 cm long cylinder of EJ-200 (a) and EJ-256 (b) at 10 cm distance. Black points are experimental data, red curve is the calculated energy deposition and blue curve is the calculated spectrum considering quenching effects.

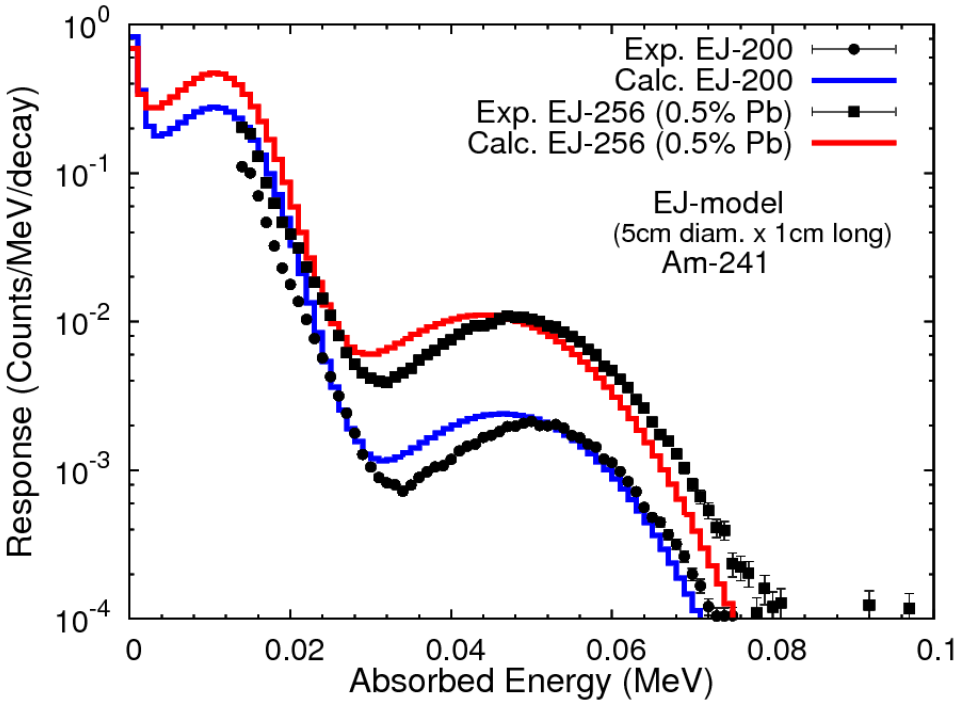

(a)

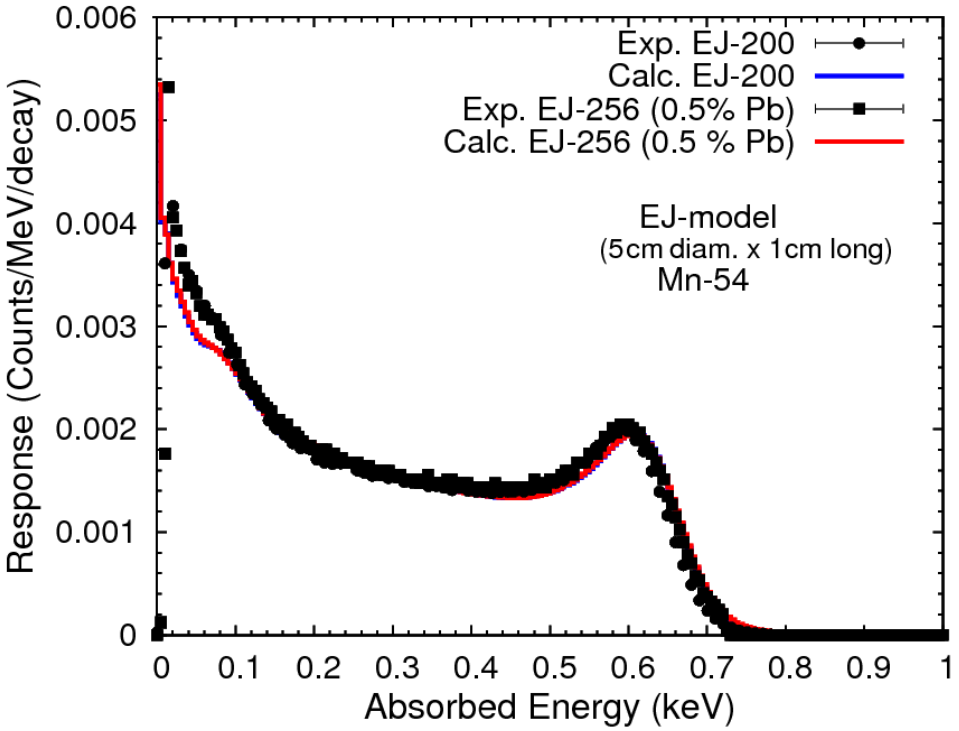

(b)

Figure 41 Overlap plot of measured and calculated light output distribution of EJ-200 and EJ-256 for Am-241 (a) and Mn-54 (b), respectively. Filled circle and square are experiment for EJ-200 and EJ-256 (0.5 % Pb), respectively. Blue and red histograms are calculation for EJ-200 and EJ-256 (0.5 % Pb), respectively.

Table 8 Measured and calculated absorbed dose rate of EJ-200 (5 cm diameter x 1 cm long) derived from the pulse height spectra as in Figure 36 to Figure 40.

Sources	kBq (as on 01.01.2015)	Absorbed dose rate (µGy/h) EJ-200				
		M			C1	C2
Am-241	405.2	0.045	±	0.002	0.066	0.040
Co-57	263.2	0.193	±	0.007	0.256	0.182
Cs-137	348.9	2.922	±	0.086	2.840	2.770
Mn-54	323.6	2.453	±	0.029	2.620	2.618

Table 9 Measured and calculated absorbed dose rate of EJ-256 (5 cm diameter x 1 cm long) derived from the pulse height spectra as in Figure 36 to Figure 40.

Sources	kBq (as on 01.01.2015)	Absorbed dose rate (µGy/h) EJ-256 (0.5 % Pb)				
		M			C1	C2
Am-241	405.2	0.164	±	0.005	0.223	0.143
Co-57	263.2	0.241	±	0.006	0.363	0.269
Cs-137	348.9	2.983	±	0.039	2.900	2.760
Mn-54	323.6	2.498	±	0.037	2.635	2.492

Table 10 Ratio of calculated (C1 and C2) to measured (M) absorbed dose in scintillator for the data shown in Table 8 and Table 9.

Source	EJ-200		EJ-256	
	C1/M	C2/M	C1/M	C2/M
Am-241	1.47	0.88	1.36	0.87
Co-57	1.33	0.94	1.51	1.06
Cs-137*	0.97	0.95	0.97	0.93
Mn-54	1.07	1.06	1.05	0.97

*Cs-137 measurement with Al of 2 mm.

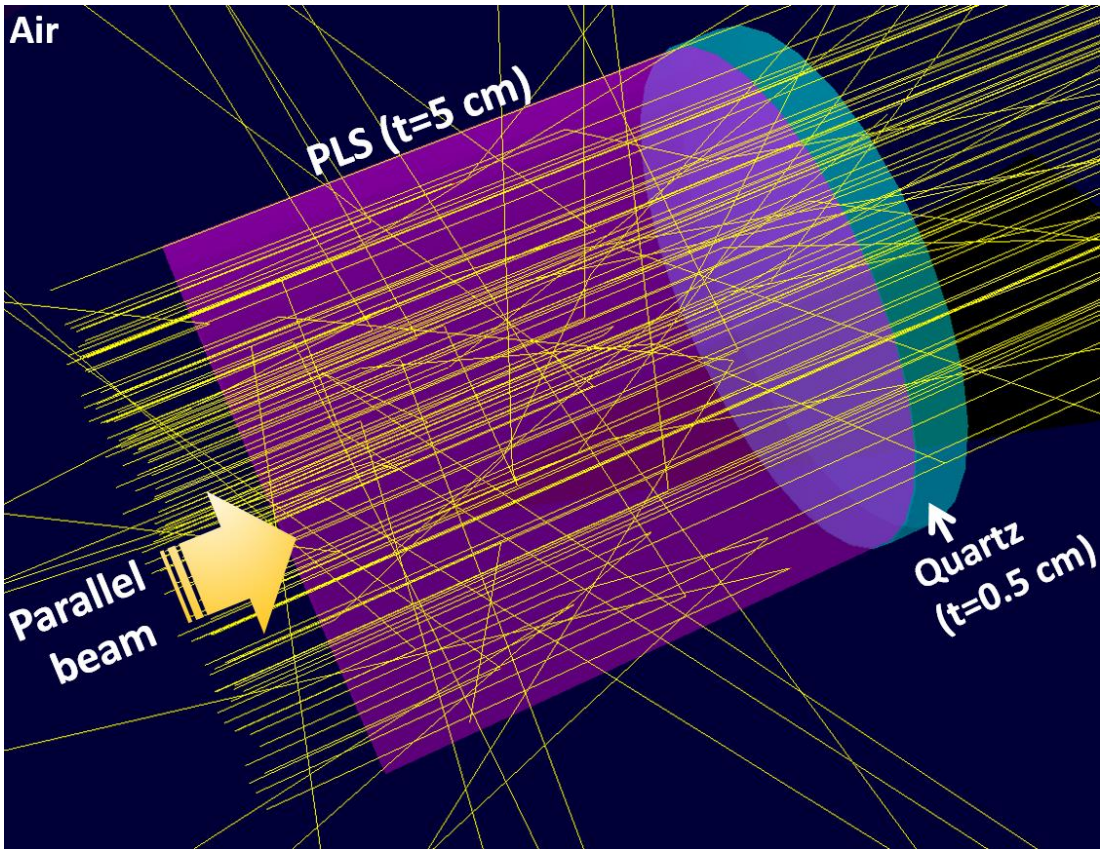

Figure 42 Simulation geometry modelled in EGS-CGview for calculation of the scintillator and soft-tissue absorbed dose. While maintaining the diameter of both scintillator and PMT, the parallel photon beams were incident to the plastic scintillator (PLS=5 cm long) which coupled to PMT window (Quartz=5 mm long). In the case of soft-tissue, the calculation was done without the window.

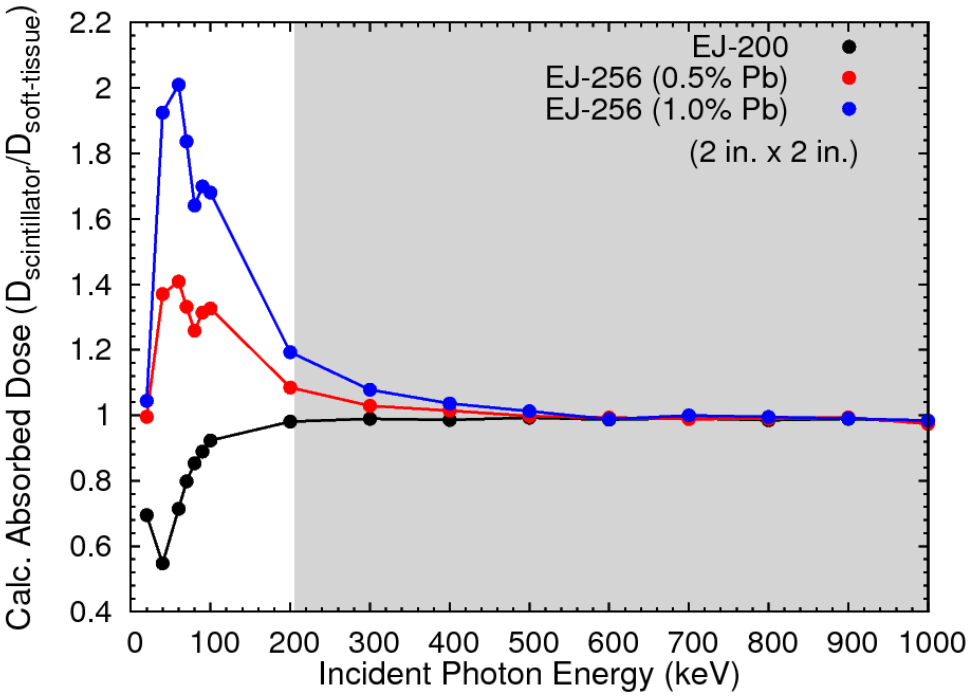

(a)

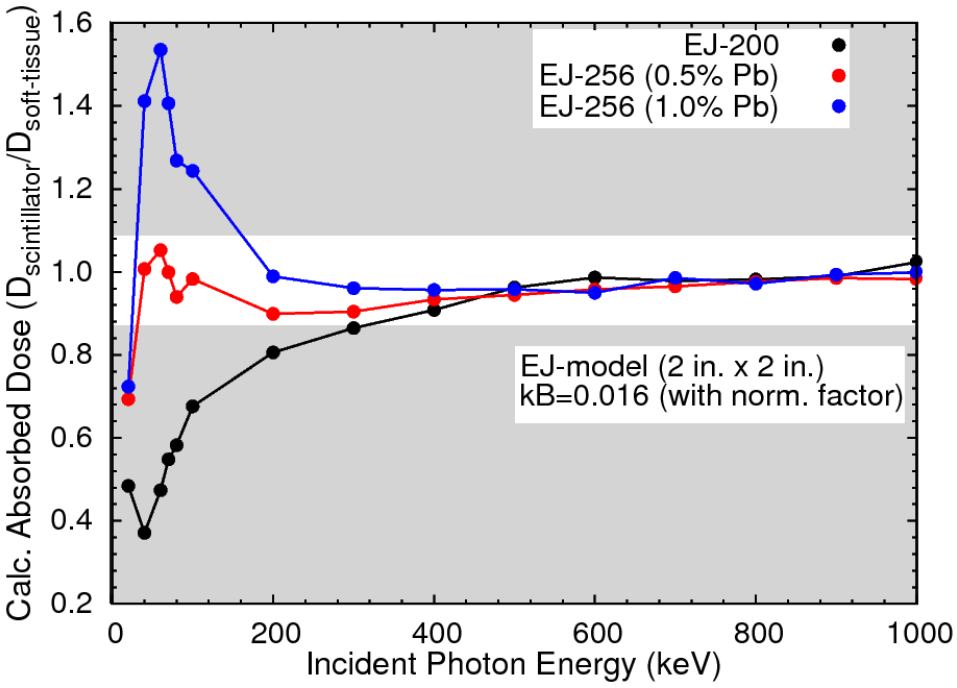

(b)

Figure 43 The ratios of calculated absorbed dose for EJ-200, EJ-256 (0.5% Pb) and EJ-256 (1.0% Pb) to soft-tissue are represented by black, red and blue dotted lines, respectively. Initially, the ratio was calculated based on absorbed energy (a). By considering the light output (b), the absorbed dose value by EJ-256 (0.5% Pb) was closer to soft tissue in wide energy range. EJ-256 (0.5% Pb) would be ideal for low energy photon dosimetry.

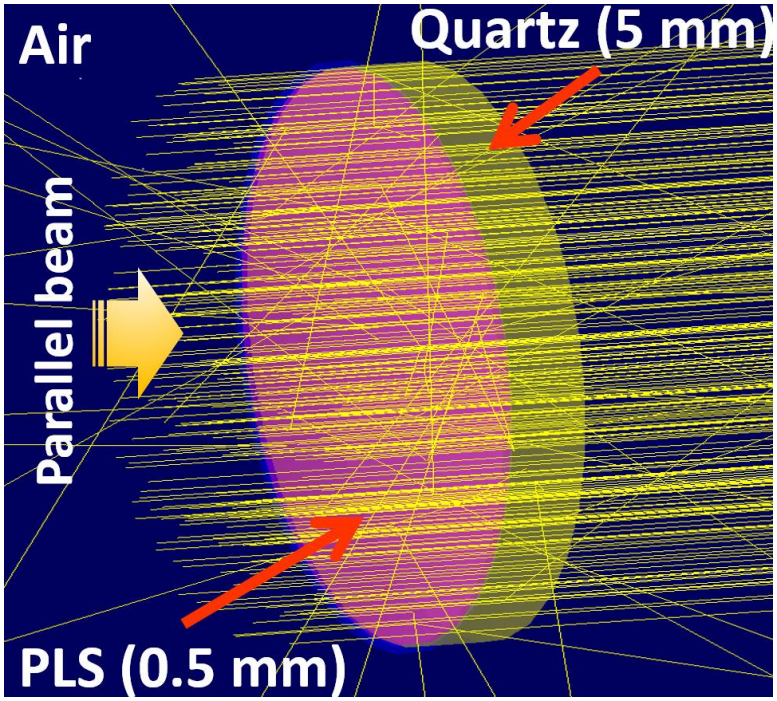

Figure 44 Simulation geometry modelled in EGS-CGview for estimation the effect of PMT window on the scintillator absorbed dose. While maintaining the diameter of both scintillator and PMT, the parallel photon beams were incident on the thin plastic scintillator (PLS=0.5 mm long) which was coupled to the PMT window (Quartz=5 mm long).

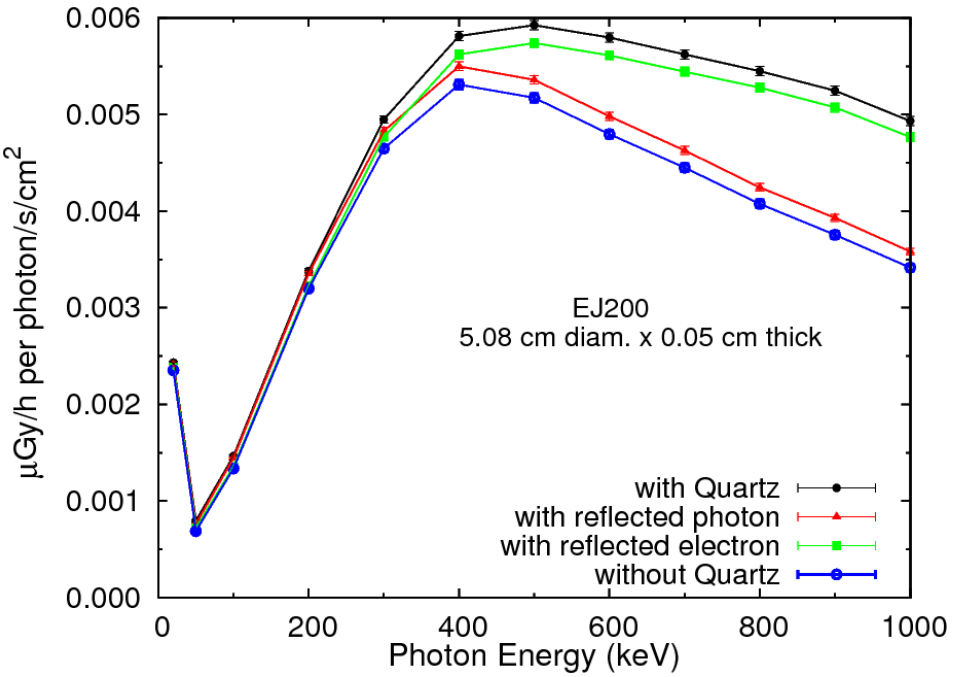

Figure 45 The absorbed dose rate for thin scintillator with (black line) and without considering the PMT quartz window (blue line). From 400 keV to 1 MeV, the additional dose due to quartz increases from 20 to 43 %. The red line and green line show backscattered photon and backscattered electron contribution to dose, respectively.

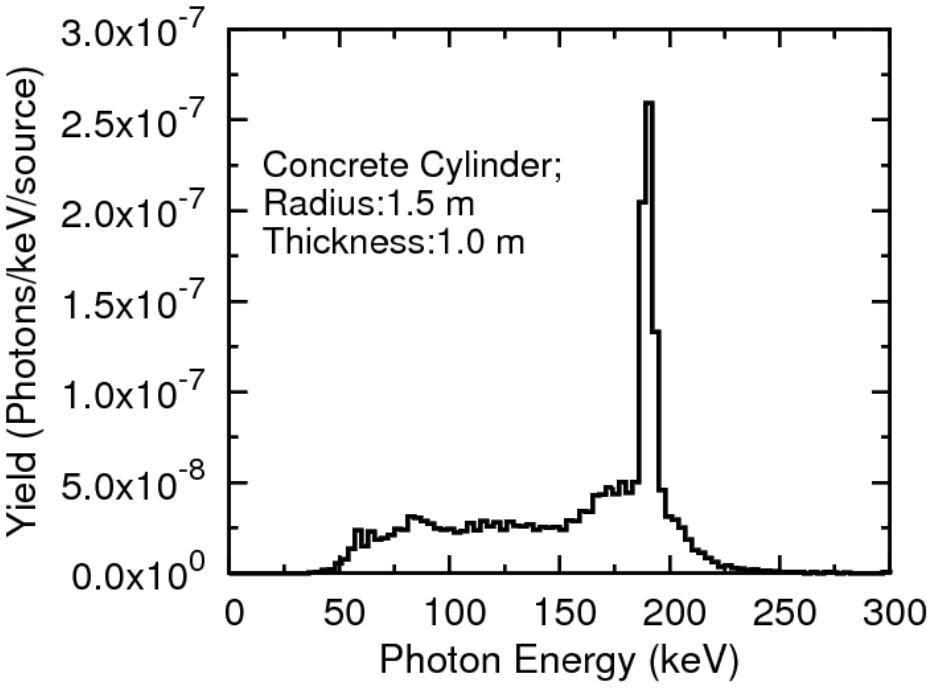

Figure 46 The typical calculated photon spectra for Cs-137 (662 keV) under the proposed backscatter layout as Figure 14. The parameters shown in Table 9. The detector response was ignored. The peak energy of the backscatter field obtained is at 190 keV.

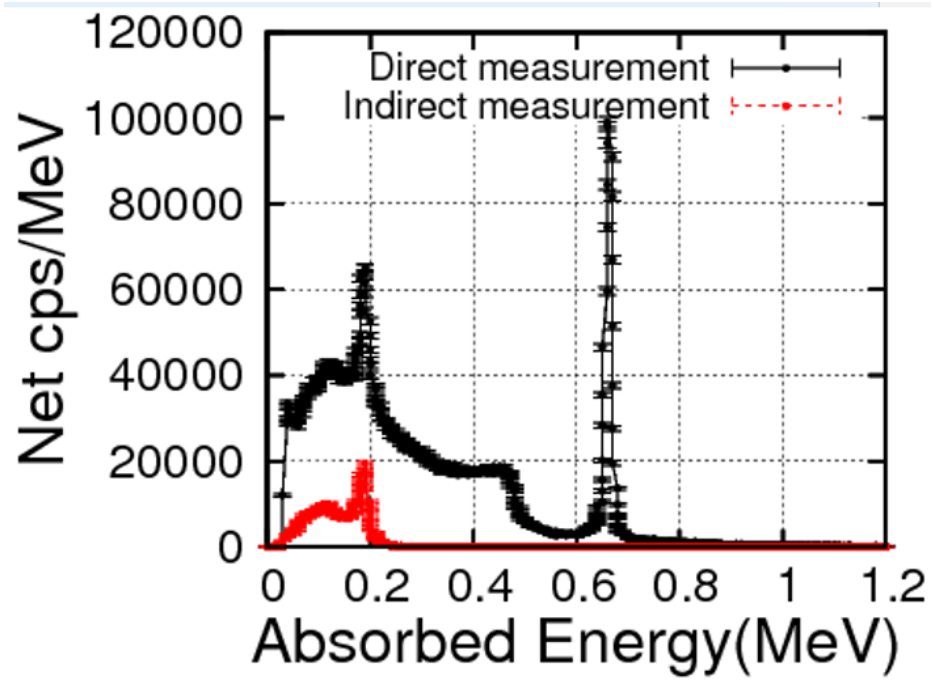

Figure 47 Measured pulse height distributions by a 1 cm³ CZT detector (KROMEK, GR1) under the proposed layout as shown in Figure 14 from a Cs-137 source. Black dotted represent the measured without the lead block showing the photopeak of 662 keV and backscattered field with peak at around 200 keV. Red dotted denoted the backscattered field when inserting a 10 cm x 10 cm x 10 cm lead block. The total net count rate of this backscattered field is smaller by a factor 11.

Table 11 Peak-to-total ratio and dose of the calculated photon spectra as a function of source to floor distance (SFD).

SFD (cm)	Peak-to-Total Ratio	Calc. Ambient Dose (Sv/photon)		
0.5	No peak appears	6.60E-18	±	1.7E-19
5	0.511	9.01E-18	±	2.0E-19
15	0.641	8.18E-18	±	1.9E-19
20	0.682	7.77E-18	±	1.8E-19

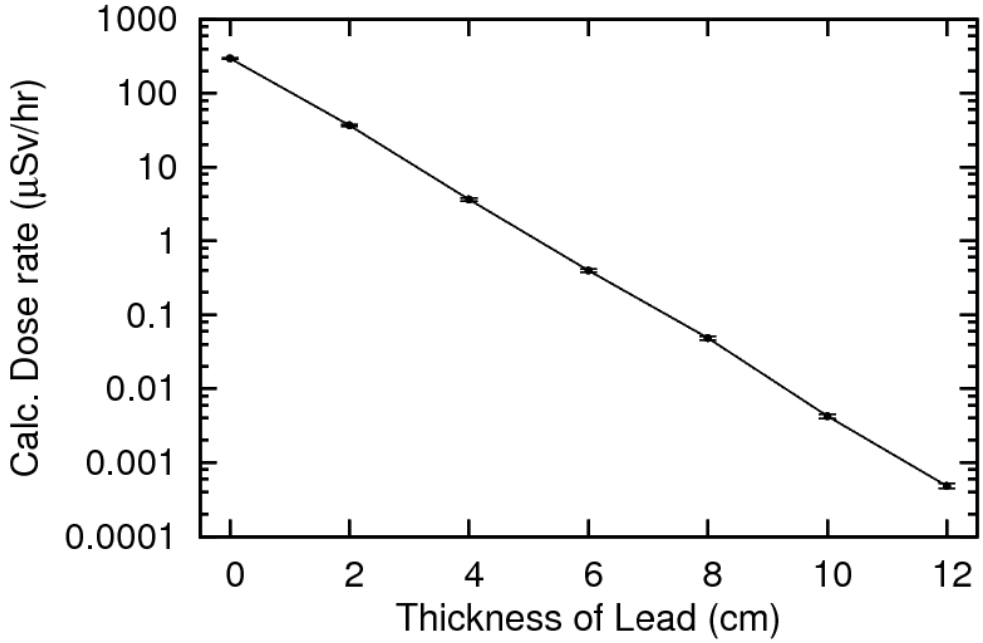

Figure 48 Dose rate as a function of lead thickness for 208 MBq Cs-137. The line was shown together as eye-guided.

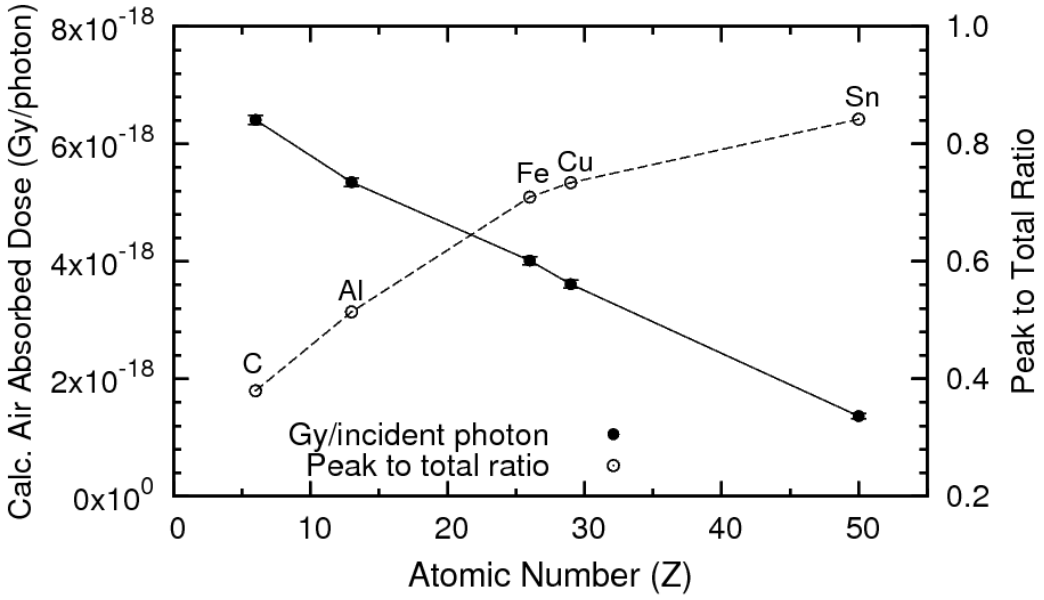

Figure 49 Calculation results for five different scattering materials (Carbon, Aluminum, Iron, Copper and Tin) of 1-m thickness. All simulations were performed for 5 m ×5 m areas. The effects of the scattering material in terms of peak ratio and air absorbed dose of the whole spectra (Gy/incident photon) are shown together. Both factors were considered in the selection of the optimum material. The lines were shown together as eye-guided.

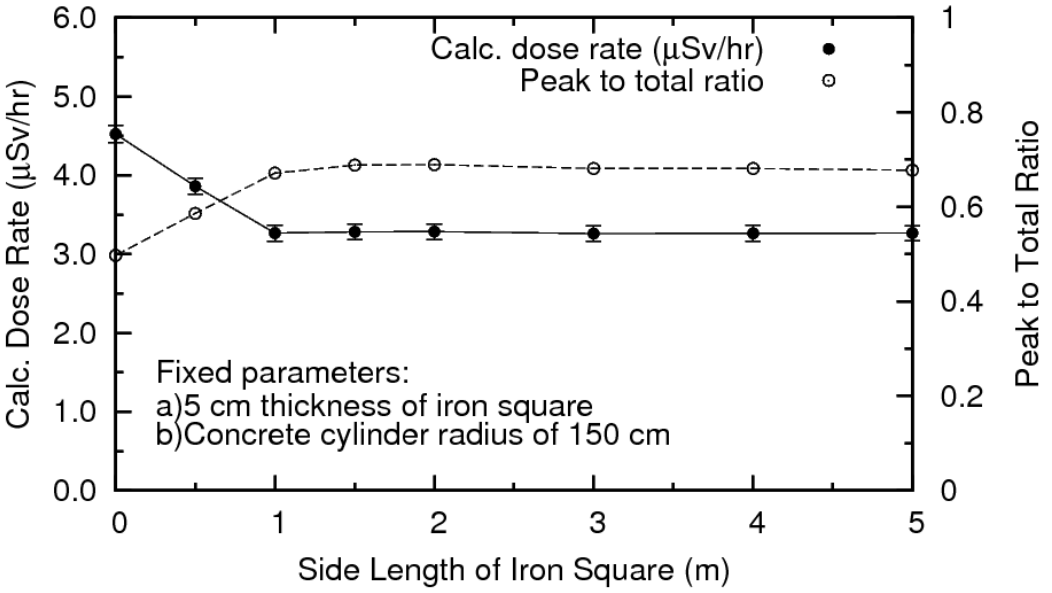

(a)

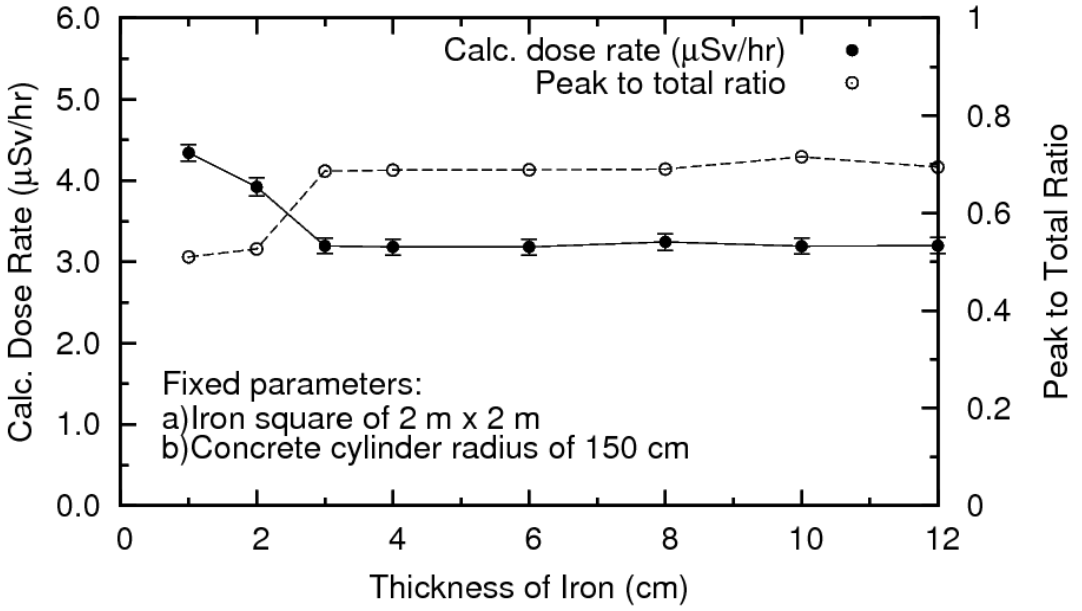

(b)

Figure 50 Calculated dose and peak-to-total ratio of the backscattered photons from the concrete floor with an added square iron block of (a) various sizes and (b) various thicknesses. The lines were shown together as eye-guided.

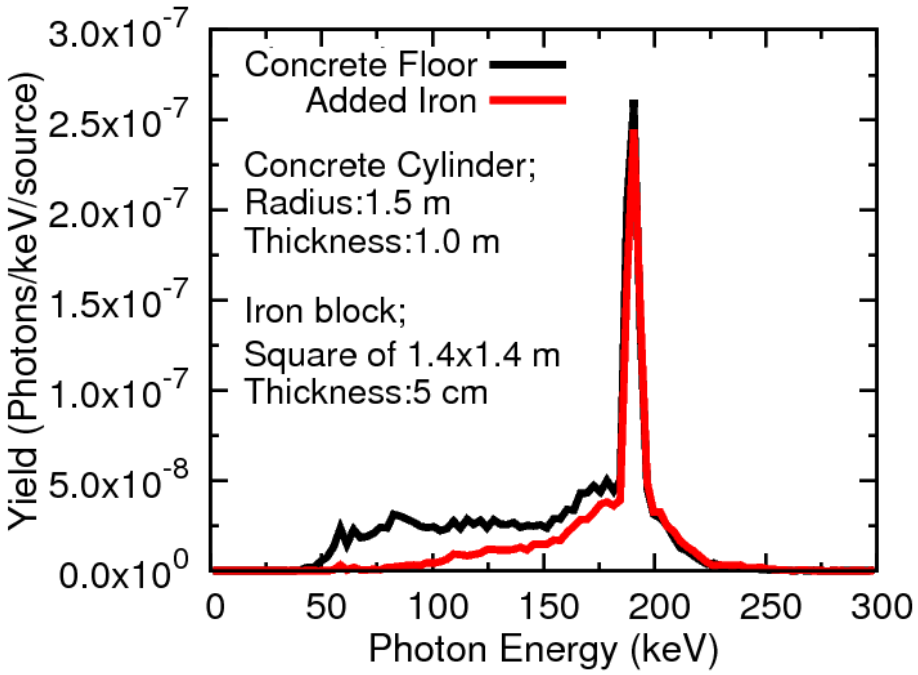

Figure 51 Calculated photon spectra at ~200 keV using a backscatter layout with a bare concrete floor and with the addition of a 1.4 m x 1.4 m x 0.05 m iron square on the floor. Adding iron on the concrete floor decreases the low energy components of the spectra (≤ 155 keV) by a factor of 3.

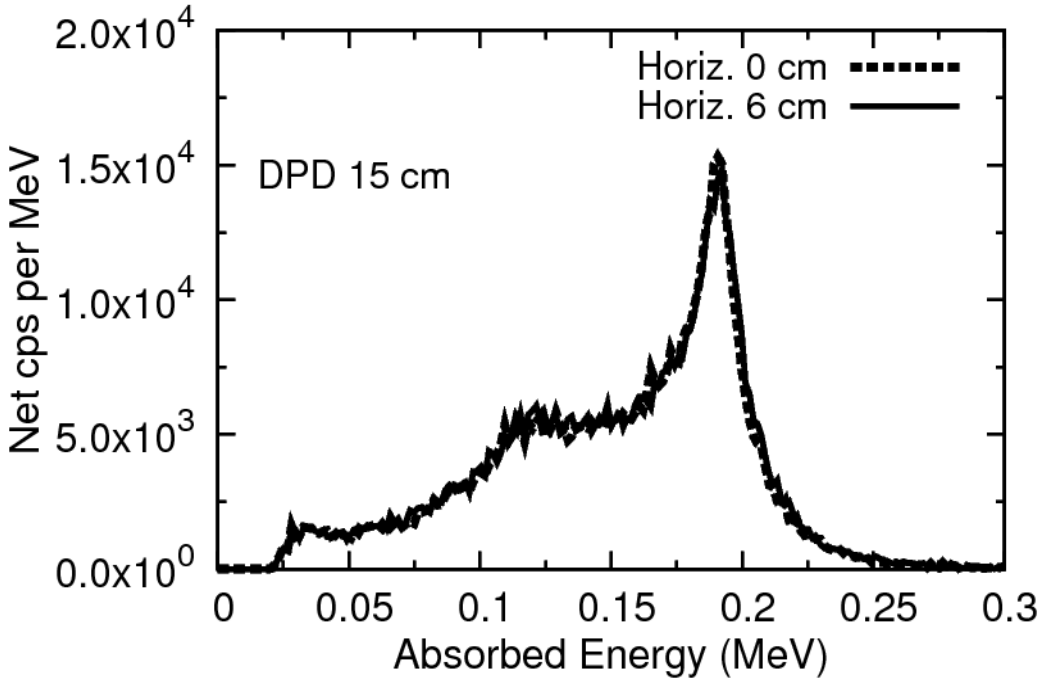

Figure 52 The measured pulse height distributions by a 1 cm³ CZT detector (KROMEK, GR1) at horizontal positions of 0 cm and 6 cm for DPD of 15 cm. The measured spectra display no significant shape variation in the horizontal direction (< 2 % per 6 cm).

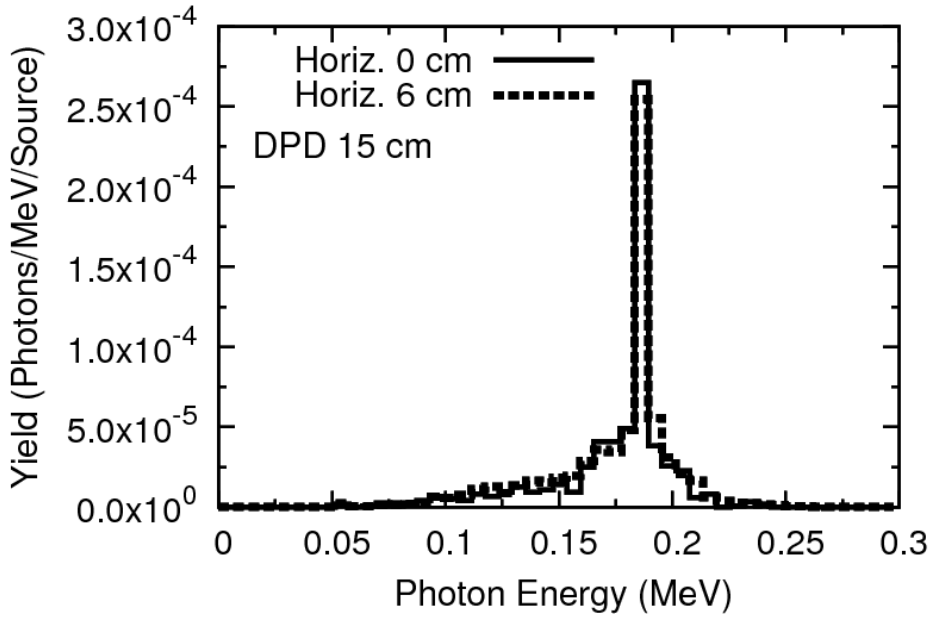

Figure 53 The calculated photon spectra at horizontal positions of 0 cm and 6 cm for a DPD value of 15 cm. The photon spectra show no significant shape changes in the horizontal direction, consistent with the measured spectra.

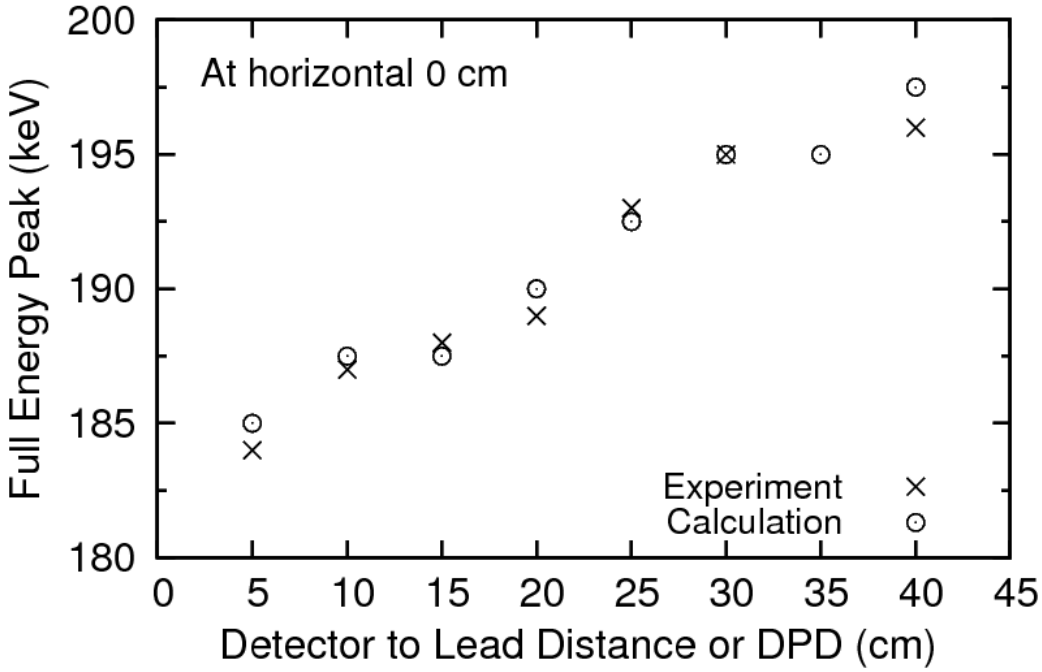

Figure 54 The full energy peak at the horizontal 0-cm position as a function of DPD.

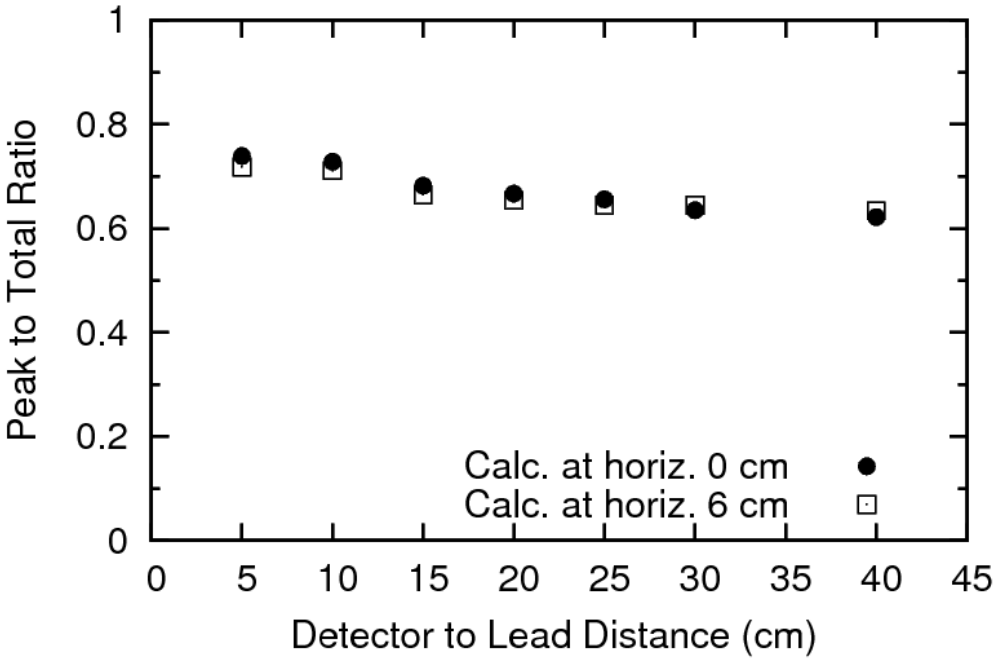

Figure 55 Summary of peak-to-total ratios of the calculated photon spectra at the horizontal 0- and 6-cm positions with respect to the source for each DPD.

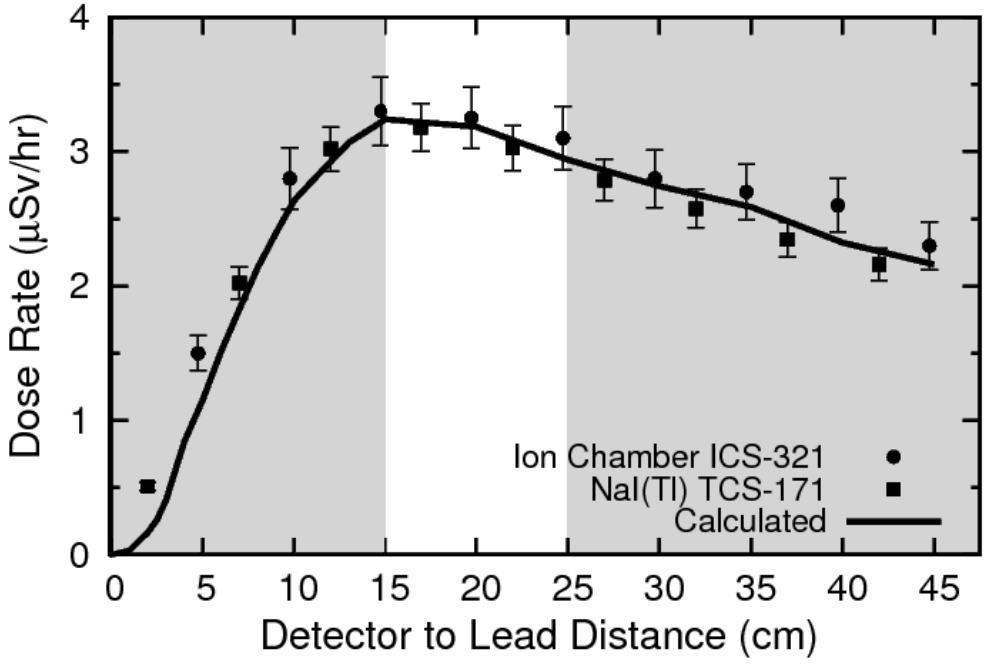

Figure 56 The dose rate at the 0-cm horizontal position for several DPD values from 10 to 45 cm. The line represents the calculated dose rate and the circles denote the measured dose rate for the 208-MBq Cs-137 source. A strong dose rate dependence (~21 % difference) is evident for DPDs of 10 to 15 cm, thus these detector positions are not recommended.

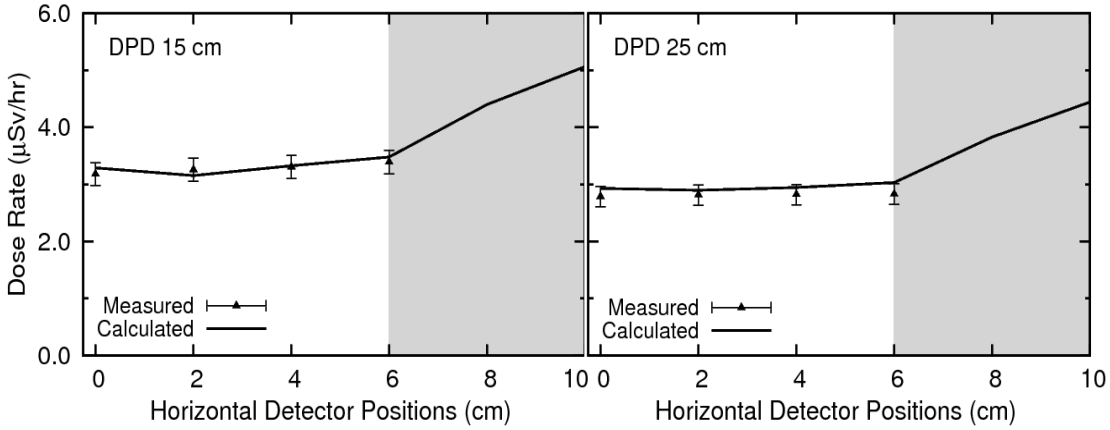

(a) (b)

Figure 57 The dose rate distribution in the horizontal direction for DPD of: (a) 15 cm and (d) 25 cm. The line represents the calculated dose rate and the circles the measured dose rate. There is no significant difference of dose rate in the horizontal direction below 6 cm for both DPDs.

Table 12 The properties of measured spectra as shown in Figure 60.The dose rate were measured by an air ionization chamber (ICS-321).

X-ray	250 kVp , 0.1mA		
Filters	5 mm W	JAERI	NIST
Peak centroid (keV)	219	204	200
Mean Energy (keV)	168.1	171.5	170.4
Peak Width (σ=keV)	17	33	34
Mean Direct Dose rate (μSv/hr)	6.9 ± 0.58	41.1 ± 2.5	42.4 ± 3.6
Mean Scattered dose (μSv/hr)	0.93	5.33	5.75

Table 13 Optimized layout parameters of Figure 15. Four parameters were optimized based on calculations and experiments by comparing their tendency; lead block sizes, source to floor distance (SFD), scattering material, and detector to lead distance (DPD).

Layout parameters	Value of parameters
Lead block	10 cm (length) x 10 cm (width) x 10 cm (height)
Source to floor distance (SFD)	20 cm
Detector to Pb block distance (DPD)	In the range of 15 to 25 cm
Scattering material	Added iron slab of 1.4 m x 1.4 m x 0.05 m on concrete floor

Table 14 The volume of the uniform backscattered radiation field in the horizontal and vertical directions.

Summary of radiation uniformity range		Estimated uniform dose volume at tested area as Figure 15
Horiz.	12 cm (From -6 to 6 cm)	1440 cm^3
Vert.	10 cm (From DPD 15 to 25 cm)	

Table 15 The contribution (%) of low energy component (LEC) towards dose value

Scattering Materials	Dimension	% of low energy components (≤ 155 keV) contributed to total calc. dose rate
Iron	3 m x 3 m x 1 m	15
Concrete	3 m x 3 m x 1 m	42
Iron on Concrete (real situation)	1.4 m x 1.4 m x 0.05 m of iron on 3 m x 3 m x 1 m concrete	19
Iron on Concrete (same size)	1.4 m x 1.4 m x 0.05 m of iron on the same area of concrete with 1 m thickness	18

Under the present backscatter layout, the percentage contribution of photon dose from low energy components (≤ 155 keV) was investigated. Generally, adding iron material will get high peak to total ratio of photon field, thus the contribution from LEC is small, from 42% to be 19%.

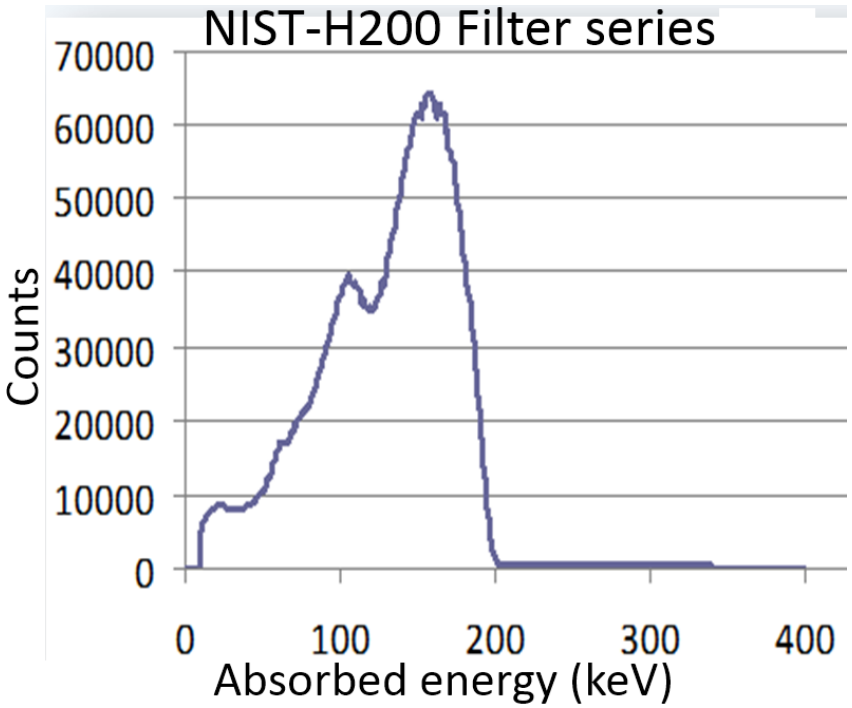

Figure 58 Example of the filtered X-ray spectra measured by using a CdTe detector (ICS-4000) to qualitatively see the spectra for the purpose of X-ray calibration [47]. The X-ray of 200 kVp was filtered with the NIST filter series.

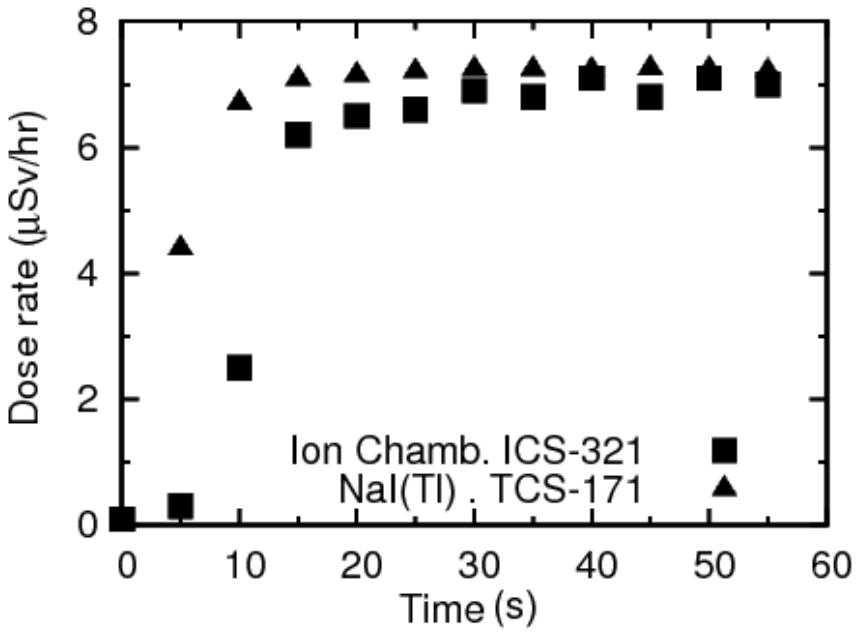

Figure 59 The measured dose rate of filtered X-ray as function of time irradiation. The figure suggested about 40 s is necessary as for the stability of X-ray output.

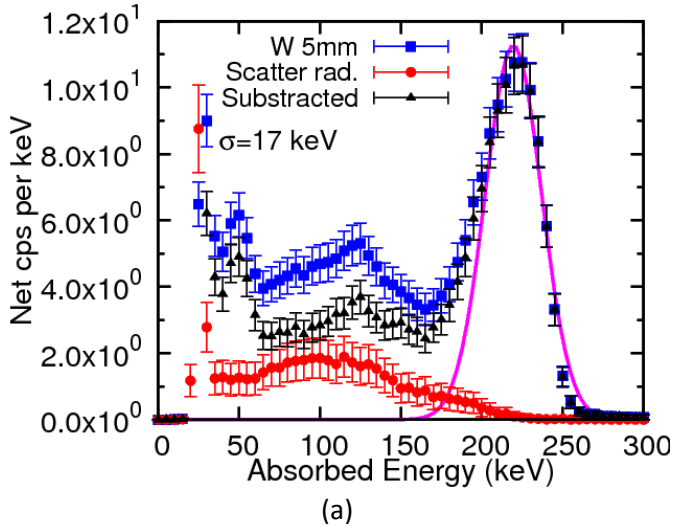

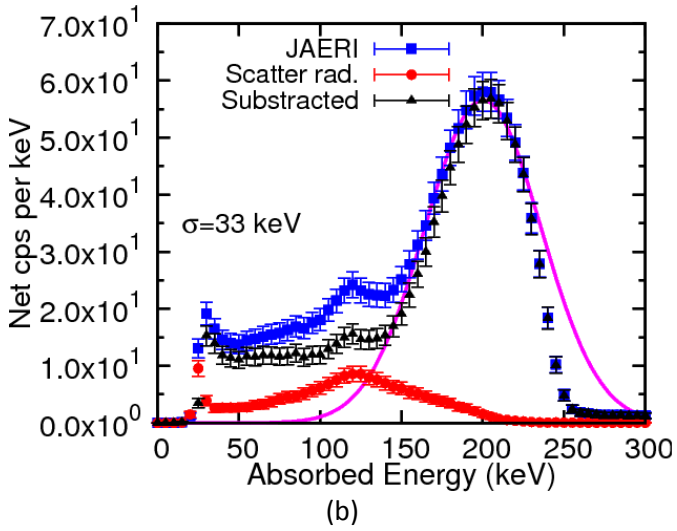

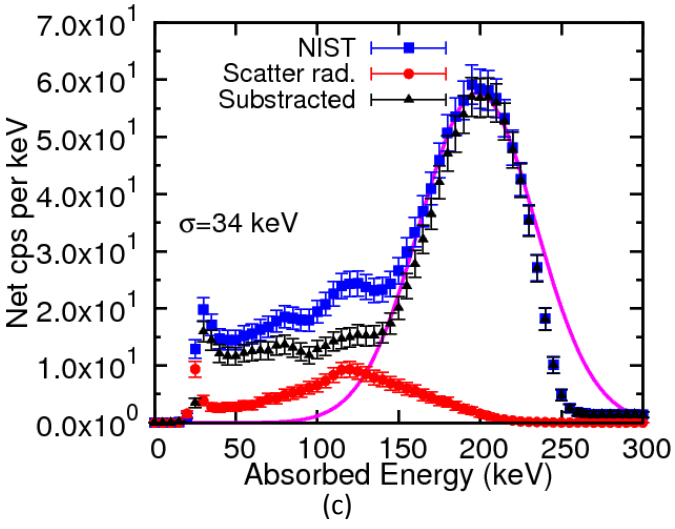

Figure 60 Measured pulse height spectra of filtered X-ray (X-ray of 250 kVp, 0.1 mA) for the same filters as calculated in Figure 17 (a)-(c). Black dots are the net count rate (cps) by subtractions of scattered radiation (red dots) from the signal (blue dots). Detailed properties of each spectra are given in Table 12.

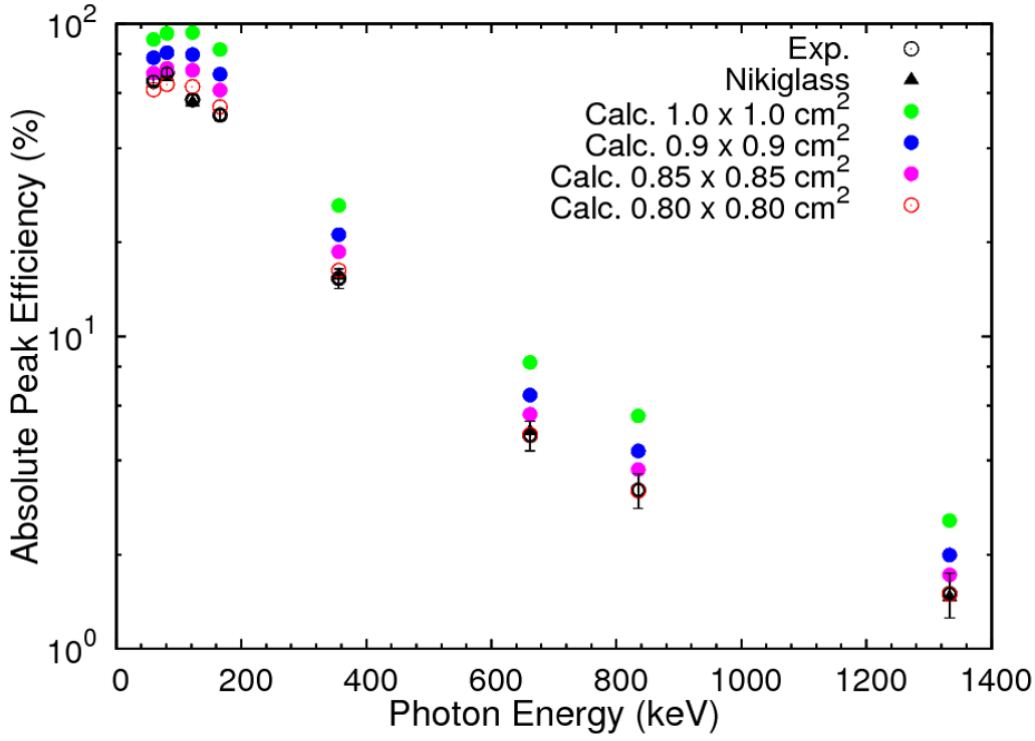

(a)

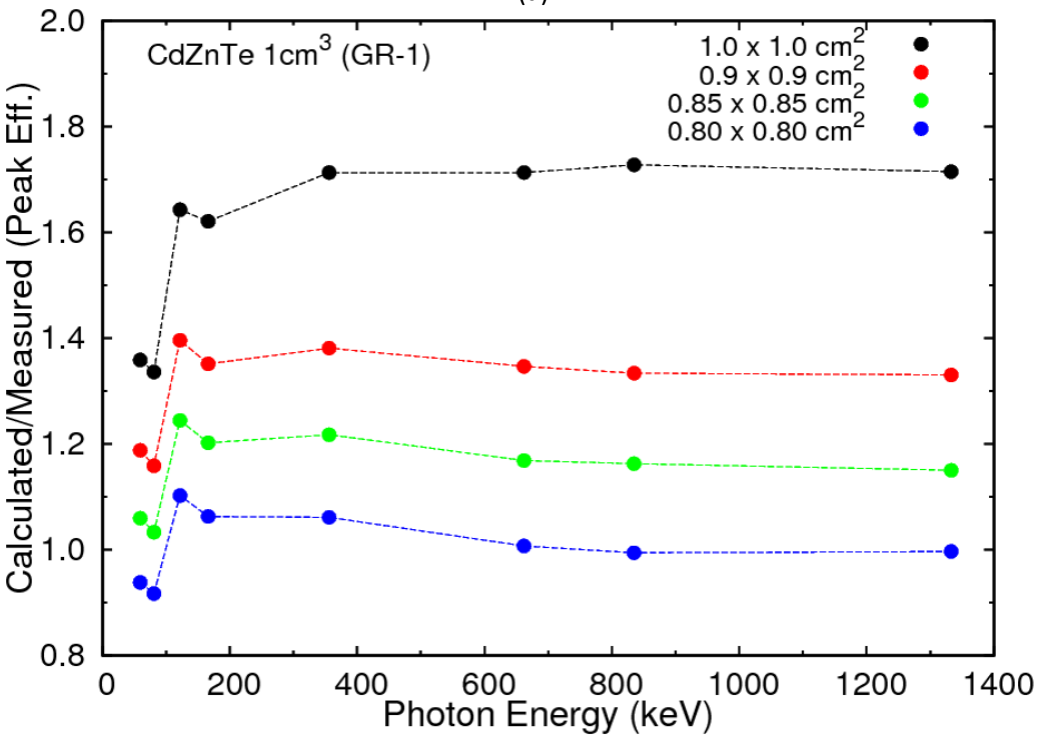

(b)

Figure 61 Comparison of measured and calculated absolute peak efficiency. In (a), the measured data (circles) are in agreement with literature (triangles). The calculated values are shown by closed circles for several areas of the CZT. Figure (b) shows the ratio of calculated to measured peak efficiency as the area of CZT was reduced.

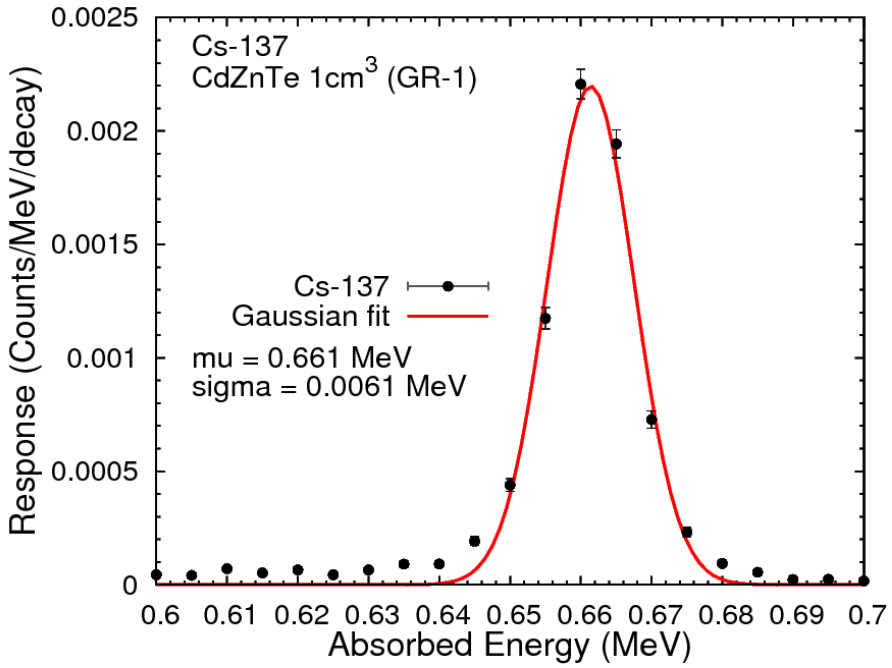

Figure 62 Measured photopeak of Cs-137 source by CZT was fitted by Gaussian function to deduce the FWHM=2.16 %. The calculated spectra were smeared with the same FWHM.

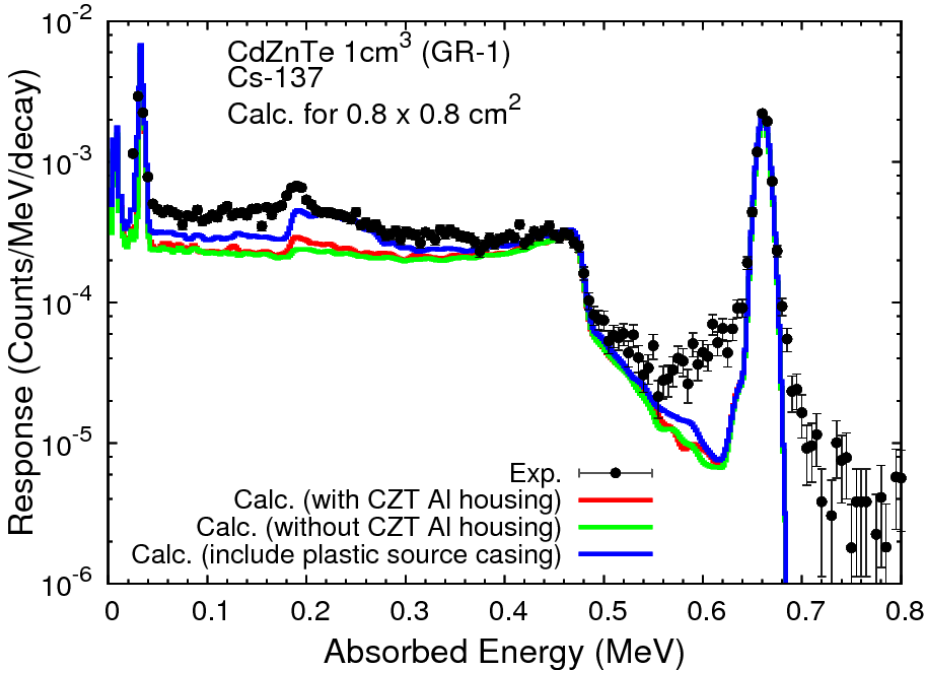

Figure 63 Measured and calculated absorbed energy spectra of Cs-137 source by CZT. The calculated photopeak of 662 keV agreed with the experimental data (black dotted) by reducing the “effective” crystal area. By comparing the red and green line, a small peak around 200 keV was known due to the backscattered photons of Al housing.

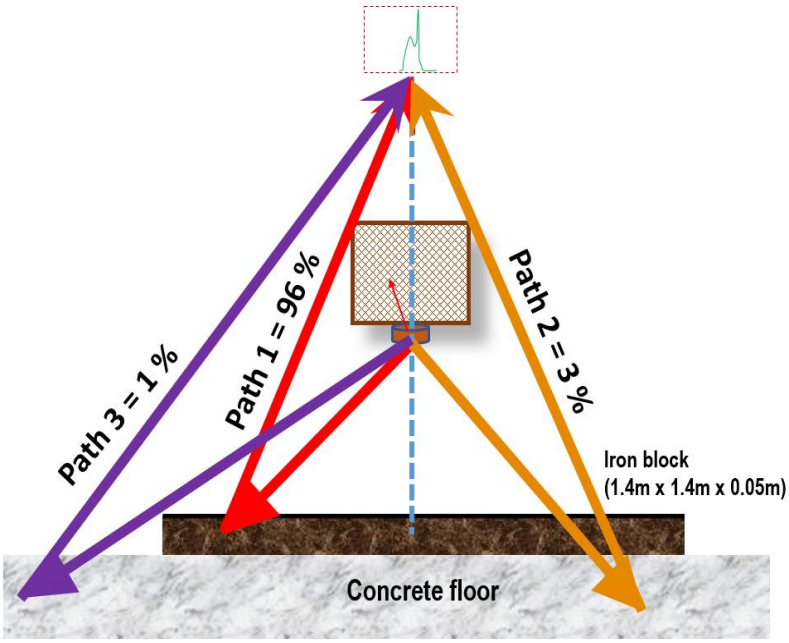

Figure 64 The paths of reflected photons under the optimized backscatter layout. Three path were investigated to know the source of reflected scattered photons. Most of the detected scattered photons are from Iron (96%). The contribution from the concrete floor, penetrated the iron blocks before scored was only 3%. 1% of the events occur outside the area of iron blocks and detected. Thus, collimator is not necessary to restrict the source direction.

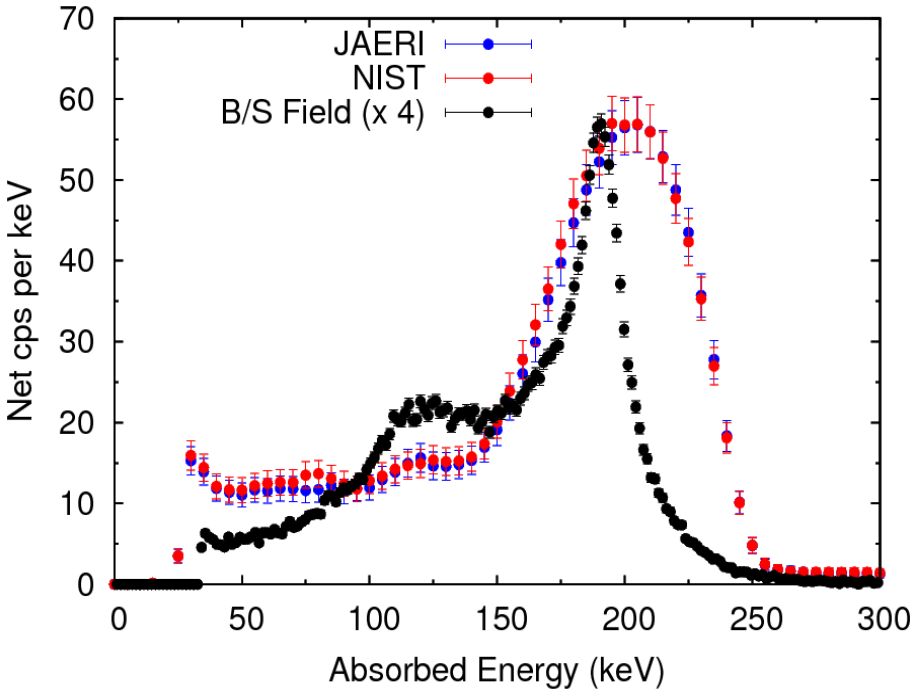

Figure 65 Comparison width of ~200 keV mono-energetic field of backscattered photon field (σ=10 keV) with filtered X-ray (σ=34 keV) using an X-ray tube. The backscatter field can provide narrower energy photons.

5 CONCLUSION

In the present research, an approach of low energy photon dosimetry was performed to improve dosimetric reliability of the existing employed dosimeters through development of detector and calibration field for few tens of keV to MeV energy region. In both studies, the experimental data had been discussed and compared with the output of calculations.

For detector development, the light output of plastic scintillator was found depend by the energy of incident radiation. It was found that it is not linear towards lower electron energy an effect known as ionization quenching. This is the problem of plastic scintillator for absorbed dose measurement in keV region. In this study, the absorbed dose was obtained from absorbed energy. Therefore energy response very important. The work can be summarized as follows:

(a) Electron response of plastic scintillator is obtained by Compton coincidence technique. Quenching parameter for electron, *kB=0.016* g cm^{-2} MeV^{-1} , is determined based on experimental data.
(b) Photopeak of 59.5 keV gamma ray from Am-241 was utilized to determine energy resolution of plastic scintillator. The resolution of other energies are obtained as $\mathrm{FWHM_o}/\sqrt{\mathrm{E}\ /E_o}$ to get reasonably good agreement with experiment. This method is superior to previous measurements using Compton edge.
(c) The pulse height distribution was well reproduced by EGS5 calculation by considering electron response for all gamma sources, in a wide energy range. Both low and high energy could be reproduced by the same value of *kB*.
(d) In the case of Cs-137 source, the agreement was further improved over the entire spectra compared to previous available data. The experimental results well agreed at the portion of energy lower than the Compton edge peak under conditions where beta radiation of the source avoided.
(e) Measured and calculated absorbed dose agreed from 3 to 13 % for photons of energies from 835 keV down to 59.5 keV.
(f) Experimentally confirmed that 0.5 % lead-doped plastic scintillator compensated for the lower response of plastic scintillator due to smaller effective Z and ionization quenching effect.
(g) Effect on absorbed dose from PMT quartz windows is estimated by EGS5 calculation. The windows gives up to 40 % enhancement for photon energies up to 1000 keV. The effect should be considered when measuring absorbed dose with relatively thin plastic scintillators.

From point b, c, d, and e, I concluded that the property of the plastic scintillator becomes clear when used as a dosimeter for low energy photon. Thus, applicability of plastic scintillator for low energy photon dosimetry is substantially improved by this study. More reliable photon dosimetry was provided by combining both quantities of the deposit energy (depe) and light output (L_{out}).

The cross comparison of EJ-256 (0.5 % Pb) for various sources obtained similar agreement as EJ-200. Thus calculation with EGS5 can be used for dosimetry study ofplastic scintillator by considering both deposit energy and light output.

For development of calibration field, 200 keV mono-energetic photon field was newly developed under well-examined backscatter layout. The optimal backscatter layout was found to comprise a 1 x 1 m^2 steel floor, a radioactive source placed 20 cm above the floor, and a 10 cm cubic lead block placed above the source. Under the proposed layout and using a 208-MBq Cs-137 source, a mono-energetic photon field with 190 ± 9.6 keV (FWHM) and a dose rate of 3.18 ± 0.18 μSv/h was obtained within an area of 10 × 10 × 10 cm at distance of 15 to 25 cm above the lead block. The field provides appropriate intensity photon field within 3 % fluctuation and narrower energy width than existing X-ray field using affordable intensity radioisotope. Several recommended X-rays filters were tested to obtain mono-energetic field around 200 keV. The peak width is larger than developed backscatter field.

CdZnTe detector was employed when studied the energy width of photon calibration field. By default, there is a strong disagreement of the absolute peak efficiency and pulse height distribution spectra with measurements of various sources. Through the comparison of the results between measured and calculated, insensitive region of CdZnTe was estimated to have a reasonable agreement. Therefore, additional consideration of incomplete charge collection or insensitive region are required to accurately simulate the radiation response of the CdZnTe detector and thus fully understand the properties of the detector.

REFERENCES

[1] International Atomic Energy Agency (IAEA) (1987). Absorbed Dose Determination in Photon and Electron Beams: *An International Code of Practice, Technical Report Series no. 277* (2nd ed in 1997), IAEA, Vienna.

[2] Almond P. R. et al. (1999). AAPM's TG-51 protocol for clinical reference dosimetry of high-energy photon and electron beams. *Med Phys.* **26(9)**:1847-70.

[3] Mainardi R. T. and Bonzi E. V. (1995). Monte Carlo Calculation of Radiation Energy Absorbed in Plastic Scintillators. *Radiat. Phys. Chem* .**45(5)**, 691-693.

[4] Beddar, A. S., Mackie T. R., & Attix F. H. (1992). Water-equivalent plastic scintillation detectors for high energy beam dosimetry: I. Physical characteristics and theoretical considerations. *Phys. Med. Biol.* **37**, 1883.

[5] Beddar, A.S. (2007). Plastic scintillation dosimetry and its application to radiotherapy. *Radiation Measurements*, **41**, 124–133.

[6] Beddar, A. S. et al. (1992). Water-equivalent plastic scintillation detectors for high-energy beam dosimetry: II. Properties and Measurements, *Physics in Medicine and Biology*, **37**, 1901.

[7] Knoll, G. F. (2010). Radiation detection and measurement. 4th Edition*. John Wiley & Sons*, pp 229-232.

[8] Berger, M.J., Hubbell, J.H., Seltzer, S.M., Chang, J., Coursey, J.S., Sukumar, R., Zucker, D.S., and Olsen, K. (2010). XCOM: Photon Cross Section Database (version 1.5). [Online] Available: http://physics.nist.gov/xcom. National Institute of Standards and Technology.

[9] Murai T. et. al. (1963). A new method of integral dose measurement with a plastic scintillator phantom*. Journal of Radiation Research* **5-1** 23-35.

[10] Hirayama, H., Sanami, T., & Namito, Y. (2013). Study of gamma-ray spectrum at height of 1 m from radionuclide widely distributed on soil surface using EGS5 Monte Carlo Code. *Transaction of the Atomic Energy Society of Japan* **12 (3**), 222-230.

[11] http://physics.nist.gov/cgi-bin/Star/compos.pl?matno=262

[12] Craun, R. L. & Smith, D. L. (1970). Analysis of response data for several organic scintillators. *Nuclear Instruments and Methods*, **80**, 239-244.

[13] Birks, J. B. (1951). Proceedings of the Physical Society. *Section A*, **64**, 874-877.

[14] Kohan, M. R., et al. (2012). Modelling plastic scintillator response to gamma rays using light transport incorporated FLUKA code. *Applied Radiation and Isotopes*, **70**, 864–7.

[15] Ghadiri, R. and Khorsandi, J. (2015). Studying the response of a plastic scintillator to gamma rays using the Geant4 Monte Carlo code. *Applied Radiation and Isotopes*, **99**, 63–68.

[16] Nardi, E. (1971). Gamma Ray Measurements with Plastic Scintillators. *Nuclear Instruments and Methods,* **95**, 229–232.

[17] Lobdell, J. L. and Hertel, N. E. (1997). Photon spectra and dose measurements using a tissue-equivalent plastic scintillator. *Rad. Prot. Dos.,* **72**, 95-103.

[18] G. T. Wright. (1953). Scintillation response of organic phosphors. *Phys. Rev*., **91(5**), 1282-1283.

[19] R. Voltz, J. L. da Silva, G. Laustriat, and A. Coche. (1966). Influence of the nature of ionizing particles on the specific luminescence of organic scintillators. *J. Chem. Phys*., **45(9**), 3306-3311.

[20] Martin J. Berger, J S. Coursey, M A. Zucker. (1999) ESTAR, PSTAR, and ASTAR: Computer Programs for Calculating Stopping-Power and Range Tables for Electrons, Protons, and Helium Ions (version 1.21). [Online] Available: http://physics.nist.gov/Star, National Institute of Standards and Technology.

[21] Brannen, E. & Garth L. O. (1962). The response of organic scintillators to electron energy deposited in them. *Radiation Research* **16(1**), 1-6.

[22] Peron, M. N., & Cassette, P. (1996). A Compton coincidence study of liquid scintillator response to low-energy electrons. *Nucl. Instrum Methods A*, **369**, 344–7.

[23] Chou, C. N. (1952). The nature of the saturation effect of fluorescent scintillators. *Physical Review **87*** **(5)**, 904-905.

[24] Rooney, B. D. & Valentine, J. D. (1996). Benchmarking the Compton coincidence technique for measuring electron response non-proportionality in inorganic scintillators. Nuclear Science, I*EEE Transactions*, **43(3)**, 1271-1276.

[25] Mainardi, R., & Bonzi, E. V. (1995). Monte Carlo calculation of radiation energy absorbed in plastic scintillators. *Appl. Radiat. lsot.* **46(6**), 499-500.

[26] Mainardi, R. et. al. (1996). Design of tissue equivalent scintillators for precise dosimetry purposes. *Radiat. Phys. Chem.* **50(2**), 159-163.

[27] Williamson, J. F., et al. (1999). Plastic scintillator response to low-energy photons. *Phys. Med. Biol*, **44**, 857–871.

[28] Lessard et. al. (2012). Validating plastic scintillation detectors for photon dosimetry in the radiologic energy range. *Med. Phys.* **39 (9**), 5308-5316.

[29] http://www.eljentechnology.com/index.php/products/plastic-scintillators

[30] http://www.hamamatsu.com/jp/en/R375.html

[31] Hohara, S., et al. (2001). A simple method of energy calibration for thin plastic scintillator. IEEE Transactions on Nuclear Science, **48(4)**. 1172-1176.

[32] Hirayama, H et al. (2010). EGS5 Code System, SLAC Report SLAC-R-730 and KEK Report 2005-8.

[33] Radioisotope pocket data book, 11th edition, Japan Radioisotope Association (JRIA).

[34] http://rcwww.kek.jp/research/egs/kek/cgview/

[35] American National Standard Performance Specifications for Health Physics Instrumentation-Portable Instrumentation for Use in Normal Environmental Conditions, ANSI N42.17A (1989).

[36] International Organization for Standardization: X and gamma reference radiations for calibrating dosimeters and dose rate meters and for determining their response as a function of photon energy, ISO 4037 (1979).

[37] JAERI-Tech-2003-095 Establishment of X-Ray Reference Fields Based on International Standard (ISO4037-1) (2003).

[38] Lamperti, P. J., Loftus, T. P., & Loevinger, R. (1987). Calibration of X-ray and gamma-ray measuring instruments at the National Bureau of Standards. *NBS Special Publication*, 250-16.

[39] G Poludniowski et al (2009). SpekCalc: A program to calculate photon spectra from tungsten anode x-ray tubes. *Phys. Med. Biol.* **54** N433.

[40] http://www.nikiglass.jp/KromeK_REF/KromeK_REF.html

[41] Miyajima, M., et al. (1993). Number of Scintillation Photons Emitted in NaI(Tl) and Plastic Scintillaotrs by Gamma-Rays. *Nuclear Instruments and Methods in Physics Research.* **40(4)**, 417-423.

[42] Naqvi, A.A. et. al. (1991). Energy resolution tests of 125 mm diameter cylinder NE213 detector using monoenergetic gamma rays. *Nuclear Instruments and Methods in Physics Research A,* **306**, 267-271.

[43] Swiderski, L. et. al. (2010). Measurement of Compton edge position in low-Z scintillators. *Radiation Measurements* **45(3-6)**, 605–607.

[44] Alan, Proctor & Wellman, J. (2012). Exposure rate by the spectrum dose index method using plastic scintillator detectors. *Radiation Protection Dosimetry*, **149(3)**, 309–14.

[45] http://www.ortec-online.com/download/Compton-Scattering.pdf, Experiment 10: Compton scattering.

[46] Swiderski, L. et. al. (2012). Electron response of some low-Z scintillators in wide energy range. *Journal of Instrumentation,* **7***.*

[47] Ludlum Measurements, Inc. (2012), X-ray Capability for Energy Response. [Online] Available:http://www.hpicorg.com/downloads/HPIC%202012%20LMI%20Energy%20Response%20Capability.pptx.

[48] http://www.horiba.com/jp/process-environmental/products-jp/environmental-radiation-monitor/details/pa-1000-environmental-radiation-monitor-radi-3124/

[49] http://www.clearpulse.co.jp/mr_gamma/

[50] Pérez, J. M., et. al. (2002). Estimate of large CZT detector absolute efficiency. *IEEE Transactions on Nuclear Science*, **49(4)**.

[51] Kim et al. (2009). Analysis of Charge Collection Efficiency for a Planar CdZnTe Detector. *Nuclear Engineering and Technology*, **41(5)**, 723-728.

[52] A.E. Bolotnikov et al. (2012). Rejecting incomplete charge-collection events in CdZnTe and other semiconductor detectors. *Nuclear Instruments and Methods in Physics Research A* **664,** 317–323.

[53] T. Sato et al. (2013). Particle and Heavy Ion Transport code System (PHITS). *Journal of Nuclear Science and Technology* **50(9)**.

PUBLICATION LIST

Original paper

1. Quasi-monoenergetic 200 keV photon field using a radioactive source with backscatter layout, Tajudin, S.M.; Namito, Y.; Sanami, T.; Hirayama, H.:, Jpn. J. Appl. Phys. 53 116401 (2014).

Conference proceedings

1. Experimental study of quasi-monoenergetic 200 keV photon field using a radioactive source with backscatter layout, Tajudin, S.M.; Namito, Y.; Sanami, T.; Hirayama, H., Nuclear Science Symposium and Medical Imaging Conference (NSS/MIC), 2013 IEEE , doi: 10.1109/NSSMIC.2013.6829658.
2. Quasi-Monoenergetic Photon Field of 200 keV using a Radioactive Source, Tajudin, S.M.; Namito, Y.; Sanami, T.; Hirayama, H., Proceedings of the Twentieth EGS Users' Meeting in Japan (2013).
3. Low Energy Quasi-Monoenergetic Photon Fields Using Different Radioactive Sources with Backscatter Layout, Tajudin, S.M.; Namito, Y.; Sanami, T.; Hirayama, H., Proceedings of the 28th Workshop on Radiation Detectors and Their Uses in KEK (2014).

Presentation at conference

International Conference (Oral presentation)

1. Study of Plastic Scintillator Properties for Radioactive Sources Dosimetry, Tajudin, S.M.; Namito, Y.; Sanami, T.; Hirayama, H.: ANS RPSD 2014 - 18th Topical Meeting of the Radiation Protection & Shielding Division of ANS (2014).

International Conferences (Poster presentation)

1. Experimental study of quasi-monoenergetic 200 keV photon field using a radioactive source with backscatter layout, Tajudin, S.M.; Namito, Y.; Sanami, T.; Hirayama, H., Nuclear Science Symposium and Medical Imaging Conference (NSS/MIC), IEEE (2013).
2. A few hundred of keV mono-energetic photon field using filtered X-ray, Tajudin, S.M.; Namito, Y.; Sanami, T.; Hirayama, H., 4th Asian and Oceanic Congress on Radiation Protection (AOCRP-4), (2014).

Meetings of academic society

1. Development of a uniform B/scatter field from ordinary concrete floor by Cs-137 through exp. and calc., Tajudin, S.M.; Namito, Y.; Sanami, T.; Hirayama, H., JSAP 74th Autumn Meeting, (2013.09.16) for poster presentation.

2. Calculation of scattering properties from radioactive sources with B/scatter layout, Tajudin, S.M.; Namito, Y.; Sanami, T.; Hirayama, H., JSAP 61st Spring Meeting, (2014.03.20) for poster presentation.

Workshops and symposium

1. Quasi-monoenergetic photon field of 200 keV: Using radioactive source with B/scatter layout, Tajudin, S.M.; Namito, Y.; Sanami, T.; Hirayama, H., 20th EGS User's Meeting, (2013.08.09) for oral presentation.
2. Low energy Quasi-monoenergetic photon field of 200 keV using a radioactive source with B/scatter layout, Tajudin, S.M.; Namito, Y.; Sanami, T.; Hirayama, H., 28th Radiation Detectors & Their Uses Workshop, (2014.01.28) for oral presentation.
3. Low Energy Photon Response of Plastic Scintillator for Absorbed Dose Measurement, Tajudin, S.M.; Namito, Y.; Sanami, T.; Hirayama, H., 29th Radiation Detectors & Their Uses Workshop, (2015.02.03) for oral presentation.

Acknowledgements

I am blessed to have the opportunity to work with wonderful peoples who have guided me throughout the years of my journey at KEK, Radiation Science Center.

My heartfelt appreciation I extend to my dear supervisor, Prof. Yoshihito Namito. The encouragement, advice, constructive criticism and continued support throughout these years I will cherish always. I wish to express my thanks to him for allowing me the experience to be his student. I would like to extend my special thanks to Prof. Toshiya Sanami and Prof. Hideo Hirayama for their critical contribution, guidance and patience.

And my most sincere appreciation to Prof. Shinichi Sasaki as my Chief examiner. Your useful advices and comments during my mid-term examination, preliminary of viva and final viva had significantly made my research and dissertation better. Also I would like to thanks for allowing me to use his equipment freely. My special appreciation and thanks to Prof. Yuichi Yamasaki and Hiroshi Iwase as my examiners for useful suggestion and comments to improve my study. Never forget, Prof. Eido Shibamura for your kindness and willingness to attend my final viva and examine the whole of my dissertation. All your comments had significantly contributed in my thesis writing.

Never the least, I would like to thank to the all staff of KEK, Radiation Science Center for their kind and encouragement to me who have made my time studying at center enjoyable. A special note of thanks is to my roommate, Ascc. Prof. Yuji Kishimoto and Masayuki Hagiwara for giving a lot of valuable ideas and willingness to listen to the problems that I have faced throughout my study.

My fabulous wife and family, I could not have done it without all of you. Thanks for the support, love and encouragement. I could not ask for more. I feel deeply humbled and blessed to have such amazing people around me.

I am sure I am forgetting someone other than above mentioned. Thank you again to all the above named and those who have not been mentioned for helping me in completing this thesis.